Universität Potsdam
Mathematisch-Naturwissenschaftliche Fakultät
Institut für Physik und Astronomie
Angewandte Physik kondensierter Materie

Thermophony in real gases

Theory and applications

Dissertation
zur Erlangung des akademischen Grades
"doctor rerum naturalium" (Dr. rer. nat.)
in der Wissenschaftsdisziplin: "Angewandte Physik"

Eingereicht an der
Mathematisch-Naturwissenschaftlichen Fakultät
der Universität Potsdam
von
Dipl.-Phys. Maxim Daschewski

Potsdam, den 5.11.2016

Abstract

A thermophone is an electrical device for sound generation. The advantages of thermophones over conventional sound transducers such as electromagnetic, electrostatic or piezoelectric transducers are their operational principle which does not require any moving parts, their resonance-free behavior, their simple construction and their low production costs.

In this PhD thesis, a novel theoretical model of thermophonic sound generation in real gases has been developed. The model is experimentally validated in a frequency range from 2 kHz to 1 MHz by testing more then fifty thermophones of different materials, including Carbon nanowires, Titanium, Indium-Tin-Oxide, different sizes and shapes for sound generation in gases such as air, argon, helium, oxygen, nitrogen and sulfur hexafluoride.

Unlike previous approaches, the presented model can be applied to different kinds of thermophones and various gases, taking into account the thermodynamic properties of thermophone materials and of adjacent gases, degrees of freedom and the volume occupied by the gas atoms and molecules, as well as sound attenuation effects, the shape and size of the thermophone surface and the reduction of the generated acoustic power due to photonic emission. As a result, the model features better prediction accuracy than the existing models by a factor up to 100. Moreover, the new model explains previous experimental findings on thermophones which can not be explained with the existing models.

The acoustic properties of the thermophones have been tested in several gases using unique, highly precise experimental setups comprising a Laser-Doppler-Vibrometer combined with a thin polyethylene film which acts as a broadband and resonance-free sound-pressure detector. Several outstanding properties of the thermophones have been demonstrated for the first time, including the ability to generate arbitrarily shaped acoustic signals, a greater acoustic efficiency compared to conventional piezoelectric and electrostatic airborne ultrasound transducers, and applicability as powerful and tunable sound sources with a bandwidth up to the megahertz range and beyond.

Additionally, new applications of thermophones such as the study of physical properties of gases, the thermo-acoustic gas spectroscopy, broad-band characterization of transfer functions of sound and ultrasound detection systems, and applications in non-destructive materials testing are discussed and experimentally demonstrated.

Zusammenfassung

Ein Thermophon ist ein elektrisches Gerät zur Schallerzeugung. Aufgrund der fehlenden beweglichen Teile verfügen Thermophone über mehrere Vorteile gegenüber den herkömmlichen elektromagnetischen, elektrostatischen oder piezoelektrischen Schallwandlern. Besonders bemerkenswert sind das resonanz- und nachschwingungsfreie Verhalten, die einfache Konstruktion und die niedrigen Herstellungskosten.

Im Rahmen dieser Doktorarbeit wurde ein neuartiges theoretisches Modell der thermophonischen Schallerzeugung in Gasen entwickelt und experimentell verifiziert. Zur Validierung des Modells wurden mehr als fünfzig Thermophone unterschiedlicher Größen, Formen und Materialien, darunter Kohlenstoff-Nanodrähte, Titan und Indium-Zinnoxid zur Erzeugung von Schall in Gasen wie Luft, Argon, Helium, Sauerstoff, Stickstoff und Schwefelhexafluorid in einem Frequenzbereich von 2 kHz bis 1 MHz eingesetzt.

Das präsentierte Modell unterscheidet sich von den bisherigen Ansätzen durch seine hohe Flexibilität, wobei die thermodynamischen Eigenschaften des Thermophons und des umgebenden Gases, die Freiheitsgrade und das Eigenvolumen der Gasatome und Moleküle, die Schallschwächungseffekte, die Form und Größe des Thermophons, sowie die Verringerung der erzeugten akustischen Leistung aufgrund der Photonenemission berücksichtigt werden. Infolgedessen zeigt das entwickelte Modell eine um bis zu einem Faktor 100 höhere Vorhersagegenauigkeit als die bisher veröffentlichten Modelle. Das präsentierte Modell liefert darüber hinaus eine Erklärung zu den Ergebnissen aus den Vorarbeiten, die von den bisherigen Modellen nicht abschließend geklärt werden konnten.

Die akustische Eigenschaften der Thermophone wurden unter Verwendung von einzigartigen hochpräzisen Versuchsaufbauten getestet. Dafür wurde ein Laser-Doppler-Vibrometer in Kombination mit einer dünnen Polyethylenfolie verwendet, welche als breitbrandiger und resonanzfreier Schalldruckdetektor fungiert. Somit konnten mehrere herausragende akustische Eigenschaften der Thermophone zum ersten Mal demonstriert werden, einschließlich der Möglichkeit, beliebig geformte akustische Signale zu erzeugen, eine größere akustische Wirksamkeit im Vergleich zu herkömmlichen Luftultraschallwandlern und die Anwendbarkeit als leistungsfähige beliebig abstimmbare Schallquellen mit einer Bandbreite bis in den Megahertz-Bereich.

Zusätzlich werden neue Anwendungen von Thermophonen wie die Untersuchung der physikalischen Eigenschaften von Gasen, die thermoakustische Gasspektroskopie, eine breitbandige Charakterisierung der Übertragungsfunktionen von Schall- und Ultraschallmesssystemen und Anwendungen in der zerstörungsfreien Materialprüfung demonstriert.

Contents

1. Introduction

2. The Energy-Density-Function model

4. Applications of thermophones

1. Introduction

1.1 What is a thermophone

A thermophone is an electrical device for sound generation. It consists either of a free-standing electrically conductive film or wire, or, for reasons of better mechanical stability, of an electrically conductive film on a solid substrate. Figure 1.1 schematically shows these two types of thermophones.

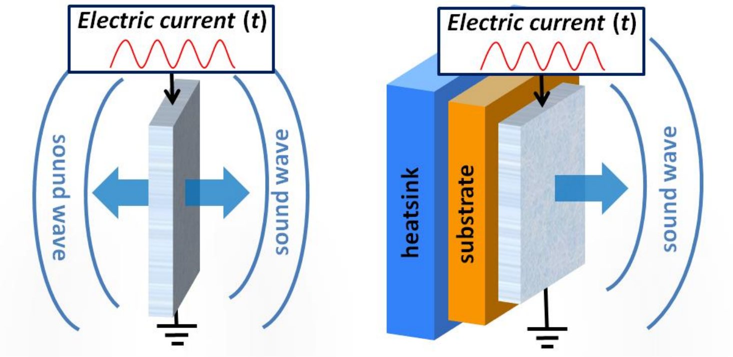

FIG. 1.1 Schematic setups of two different implementations of thermophones.

Due to their simple construction, thermophones of nearly arbitrary shape and size can be fabricated. Figure 1.2 exemplarily shows photographs of thermophones consisting of Titanium and Indium-Tin-Oxide (ITO) coatings on planar and spherically shaped substrates.

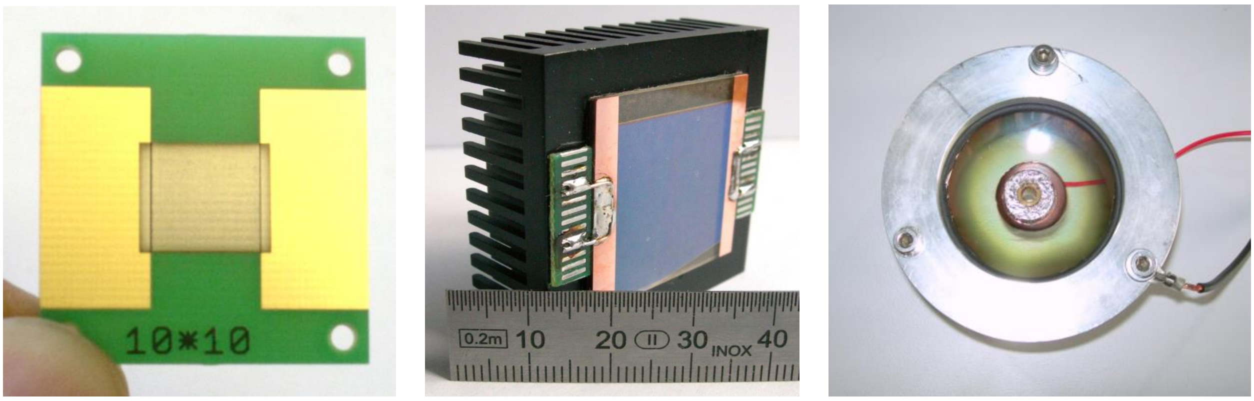

FIG. 1.2 Photographs of a few thermophones which have been fabricated as part of this PhD thesis. **(a)** A thermophone consisting of a 10 × 10 mm^2 and 50-nm-thin Titanium coating on a circuit board. Photographs **(b)** and **(c)** show thermophones consisting of 100-nm-thin Indium-Tin-Oxide coatings on planar and spherically shaped SiO_2 glass substrates.

First published experimental attempts to use thermophones for sound generation date back to the beginning of the 20th century. In 1915, De Lange tested 7-µm-thin Platinum wires as an earphone [1], and Arnold and Crandall [2] in 1917 used a 700-nm-thin platinum film as "*a precision sound source*" for calibrating microphones. In 1922, Wente [3] proposed the use of a thermophone for measuring the thermal conductivity of gases. In 1933, Gefken and Keibs [4] used thermophones to study the acoustic threshold of human hearing. In 1999, Shinoda *et al.* [5] first proposed the use of a 30-nm-thin aluminum film on porous silicon as an airborne ultrasonic source, and Boullosa and Santillan [6] showed in 2004 that such an electrically conductive film on a wood, kapton or mica substrate is also suitable for ultrasound generation. In 2005, Hwang and Kim [7] published an experimental study on free-standing nickel foils of 12, 10 and 0.75 µm thickness that were excited with electric pulses and reported on measured sound pressures of about 1 Pa (94 dB) at a distance of 50 mm from the foils. In 2008, Xiao *et al.* used a carbon nanotube (CNT) tissue as a stretchable loudspeaker [8] and tested it two years later as a low-frequency (< 100 kHz) ultrasound source in argon and helium gases [9]. In 2009, Niskanen *et al.* [10] used a suspended aluminum wire array and reached a sound-pressure level of 110 dB at 40 kHz in air at a distance of 8 cm in front of the thermophone. In 2011, Tian *et al.* tested different graphene sheets on paper substrates [11] and in 2012 experimentally investigated the performances of a 100-nm-thin Indium-Tin-Oxide (ITO) coating on polyethylene-terephthalate and glass substrates for frequencies up to 50 kHz [12]. And, in 2013, Wei *et al.* [13] demonstrated a miniaturized thermoacoustic earphone consisting of a CNT-yarn array on a silicon wafer.

1.2 Existing theoretical and experimental findings on thermophones

Up to now, published theoretical models describing thermophonic sound generation in gases [2,5,6,8-11,15-17] are based on the assumption of an expansion and contraction of the gas layer adjacent to the periodically heated surface. Supposedly, this gas layer acts as a moving piston and its movement causes the emission of sound waves. This physical concept as well as the first theoretical approach for sound pressure generated by a thermophone was introduced by Arnold and Crandall in 1917 [2].

As a thermophone, Arnold and Crandall used a free-standing 700-nm-thin platinum strip mounted between two contact clamps. Figure 1.3 schematically shows the thermophone of Arnold and Crandall. They tested it for sound generation in air at frequencies up to 3 kHz. Using the ideal gas law, Arnold and Crandall assumed a linear change of the gas volume close to the periodically heated film and proposed the following approach for the sound pressure generated in air by a free- standing metallic foil

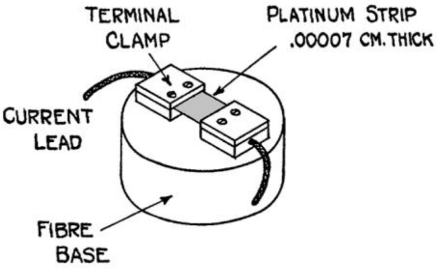

FIG. 1.3 [2] The thermophone of Arnold and Crandall.

$$p(r,f)=\frac{\sqrt{12\cdot 10^{-11}}\cdot P_{el}\cdot \rho_{0\,air}\cdot \sqrt{f}}{r\cdot d_{film}\cdot S_{film}\cdot \rho_{film}\cdot c_{p\,film}}=\frac{\sqrt{12\cdot 10^{-11}}\cdot P_{el}\cdot \rho_{0\,air}\cdot \sqrt{f}}{r\cdot C_{film}}, \tag{1.1}$$

where P_{el} is the supplied electric power, $\rho_{0\,air}$ is the air density, f the excitation frequency, r the distance from the thermophone and C_{film} – the product of the film surface area S_{film}, the film thickness d_{film}, its density ρ_{film} and its heat capacity $c_{p\,film}$ – is the heat capacity per unit area of the electrically conductive film.

Based on the experimental and theoretical results, Arnold and Crandall [2] concluded that:

- *“The conductor has to be thin.”*
- *“Its heat capacity must be small.”*
- *“To produce a pure tone free from harmonics, the excitation current has to be a pure sine wave.”*

Over the years, a couple of discrepancies in this first approach were discovered in comparison with experimental results. For example, in 1922, Wente [3] tested a 1.4-µm-thin gold foil and a 300-nm-thin Wollastone wire as thermophones and reported on "*certain discrepancies* (compared to the prediction of Arnold & Crandall) *which cannot be attributed to experimental errors*". In 1933, Gefken and Keibs [4], tested several thermophones consisting of 2-µm-thin metallic foils and of 6- and 10-µm-thin wires for sound generation in the audio-frequency rage. They also reported deviations from the theoretical prediction of Arnold and Crandall.

Since then, the thermophones have fallen into oblivion, until 1999, when Shinoda *et al.* [5] first demonstrated thermophonic sound generation in air in a frequency range up to 100 kHz using a 30-nm-thin aluminum film on porous silicon as an airborne ultrasound source. To predict the sound pressure generated by a thermophone on a substrate, Shinoda *et al.* utilized the model of McDonald and Wetzel [14] for the photo-acoustic effect (originally developed for photo-acoustic cells of a small volume and low-frequency (< 1 kHz) excitations) and proposed, without derivation, a frequency- and distance-independent approach for thermally generated sound-pressure in air

$$p = \frac{\sqrt{\gamma_{air}} \cdot P_{0\,air}}{c_{sound} \cdot T_{0\,air}} \cdot \frac{a_{air}}{e_{sub}} \cdot q_{in}\,, \tag{1.2}$$

where $\gamma_{air} = c_p / c_v$ is the isentropic expansion coefficient of air, $P_{0\ air}$ and $T_{0\ air}$ are the air pressure and temperature, $a_{air} = \lambda_{gas} / \rho_{air} \cdot c_{p\,air}$ is the thermal diffusivity of air, e_{sub} is the thermal effusivity of the substrate, c_{sound} is the speed of sound in air and $q_{in} = P_{in} / S_{film}$ is the thermal power density supplied to the thermophone. Based on the experimental and theoretical results, Shinoda *et al.* [5] concluded that the efficiency of a thermophone on a substrate can be increased by using substrates with a small thermal effusivity.

In 2004, Boullosa *et al.* [6] tested thermophones consisting of 285-nm-thin gold films on glass, wood, mica, kapton, pyrex and acrylic-plastic-sheet substrates for sound generation in air in a frequency range up to 100 kHz. They also revised the model of Shinoda *et al.* proposing some corrections, namely a linear dependence on the isentropic expansion factor γ_{air} and the incorporation of the Fraunhofer approach (an approach for the sound pressure generated in the acoustic far-field on the axis of a circular piston of radius r_{film} which is mounted in an infinite baffle) to describe the dependence of the generated sound pressure on the excitation frequency f and the distance r from the thermophone,

$$p(r,f) = \frac{\gamma_{air} \cdot P_{0\,air}}{c_{sound} \cdot T_{0\,air}} \cdot \frac{a_{air}}{e_{sub}} \cdot q_{in} \cdot \left(1 - \exp\left(\mathrm{i} \cdot \frac{2 \cdot \pi \cdot f}{c_{sound}} \cdot \left(\sqrt{r^2 + r_{film}^2} - r\right)\right)\right). \tag{1.3}$$

As reported by Boullosa *et al.* [6], the comparison of the experimental results with the prediction of Equation (1.3) shows deviations in a range of 6 – 10 dB compared to the experimental results but reproduces "well" the trend of sound pressures generated over the excitation frequency.

In 2008, Lin Xiao *et al.* [8] reported on the sound generation in the frequency range from 300 Hz to 23 kHz using free-standing CNT tissues of different thickness and surface area. For a theoretical prediction of the generated sound pressures, Xiao *et al.* applied the same assumptions as Arnold and Crandall [2], but found a solution (see Equation (1.4)) which is a little bit different from that of Arnold and Crandall (see Equation (1.1)):

$$p(r,f)=\frac{\sqrt{a_{gas}}\cdot\rho_{0\,gas}\cdot P_{el}\cdot\sqrt{f}}{2\cdot\sqrt{\pi}\cdot T_{0\,gas}\cdot r\cdot C_{film}} \tag{1.4}$$

where $a_{gas}=\lambda_{gas}/\rho_{gas}\cdot c_{p\ gas}$ is the thermal diffusivity of gas, $C_{film}=d_{film}\cdot\rho_{film}\cdot c_{p\ film}$ is the heat capacity per unit area of the film and P_{el} is the supplied electric power. λ_{gas}, ρ_{gas} and $c_{p\ gas}$ are the heat conductivity, the density and the isobaric heat capacity of the gas, respectively.

As reported by Xiao *et al.* [8], the prediction of Equation (1.4) shows deviations of about 30 dB compared to the experimental results, the slope of the generated sound pressure is larger ($p(f)\sim f^{0.7-0.8}$) than theoretically predicted ($p(f)\sim f^{0.5}$), and the difference of generated sound pressures for a one-layer thin film and a four-layer film samples is much smaller than the factor of 4 (12 dB) which is predicted by Equation (1.4). Therefore, Xiao *et al.* modified Equation (1.4) with additional terms and fitting parameters:

$$p(r,f)=\frac{\sqrt{a_{gas}}\cdot\rho_{0\,gas}\cdot P_{el}\cdot\sqrt{f}}{2\cdot\sqrt{\pi}\cdot(T_{0\,gas}+T_{film})\cdot r\cdot C_{film}}\cdot\frac{f}{f_2\cdot\sqrt{\left(1+\sqrt{\frac{f}{f_1}}\right)^2+\left(\frac{f}{f_2}+\sqrt{\frac{f}{f_1}}\right)^2}}\ , \tag{1.5}$$

where $T_{film}=P_{el}/2\cdot\beta_0\cdot S_{film}$ is the mean temperature of the film above the surroundings, β_0 is the effective convection heat transfer coefficient of the adjacent gas, S_{film} is the area of the film and f_1 and f_2 are given as: $f_1=\alpha_{gas}\cdot\beta_0/\pi\cdot\lambda_{gas}$ and $f_2=\beta_0/\pi\cdot C_{film}$.

As reported by Xiao *et al.* [8], the convection heat-transfer coefficient β_0 was used as a fitting parameter to reduce the deviations between experimental results and the model prediction. The comparison of experimental results and the prediction of Equation (1.5) showed deviations of about 6 – 8 dB. This corresponds to a deviation of sound pressure in a range of 100 – 130 %.

Three years later, in 2011, Xiao *et al.* [9] tested a thermophone consisting of a free-standing CNT tissue for sound generation up to 100 kHz in argon and helium at normal pressure and room temperature. The sound pressure was measured in all gases by means a B&K 4939 condenser microphone.

Based on the experimental results, Xiao *et al.* [9] concluded that:

- *"Fit of experimental detected sound pressure shows a proportionality of* $p(f)\sim f^{0.7-0.8}$*, deviating from the theoretically predicted square root dependence."*
- *"The sound pressure is linear to the input power."*

In 2010, Vesterinen *et al.* [15] tested a suspended Aluminum wire array for sound generation in air in a frequency range up to 100 kHz und proposed, neglecting the heat capacity of the wire array, an approach given in Equation (1.6) as an “ultimate maximum” for sound pressure generated by a free-standing film or wire

$$p(r,f) = \frac{P_{in} \cdot f}{2 \cdot c_{p\,gas} \cdot T_{0\,gas} \cdot r}. \tag{1.6}$$

As reported by Vesterinen *et al.* [15], the prediction of Equation (1.6) shows deviations of about 12 - 15 dB compared to the experimental results. This corresponds to a sound pressure deviation of 400 – 450 %.

Based on the experimental results, Vesterinen *et al.* [15] concluded that:

- *“The magnitude of the generated sound waves is frequency dependent in the sense that the thermo-acoustic effect is more suitable for producing higher frequency sounds.”*
- *“Sound pressure scales linearly with frequency, deviating from the* $f^{0.5}$ *predicted behavior of Arnold and Crandall’s model.”*
- *“Especially at high frequencies, a small* C_S *(heat capacity per unit area of the wires) would indeed be a great advantage.”*
- *“At frequencies higher than 10 kHz the heat capacity of wires started to have a notable effect.”*
- *“The acoustic efficiency improves linearly with input power … and is proportional to the square of the excitation frequency.”*

In the same year, Hu *et al.* [16] revised the models of Shinoda *et al.* [5] and Boullosa *et al.* [6] starting at the same set of time-dependent coupled partial differential equations for temperature and pressure as already used by Shinoda and Boullosa, but arriving at the solution

$$p = \frac{(\gamma_{gas} - 1)}{c_{sound}} \cdot \frac{e_{gas}}{e_{gas} + e_{sub}} \cdot q_{in}, \tag{1.7}$$

which is different from the solutions of Shinoda *et al.* (see Equation (1.2)) and of Boullosa *et al.* (see Equation (1.3)) in terms of the gas effusivity and the isentropic-expansion-coefficient dependence. The approach of Hu *et al.* as given in Equation (1.7) is similar to that of Shinoda *et al.*, independent of frequency and distance, and predicts a constant sound pressure over all frequencies and all distances. However, this prediction contradicts all existing experimental results. Additionally, Hu *et al.* theoretically investigated the expected thermal expansion of the electrically conductive film and concluded that it is very small (< 1 nm), does not contribute to the excitation of acoustic wave and hence can be neglected.

In 2011, Tian *et al.* [11] tested thermophones consisting of graphene sheets of different thicknesses (20, 60 and 100 nm) on paper substrates. The experimental result of Tian *et al.* demonstrates that the sound pressure generated by a thermophone increases linearly with the input power and that the generated sound pressure decreases with the increase of the graphene-sheet thickness. Based on the experimental results, Tian *et al.* proposed (compared to the model of Hu *et al.* (see Equation (1.7))) a modified approach for the sound pressure generated by a substrate-based thermophone incorporating the Rayleigh distance $R_0 = \pi \cdot f \cdot l^2 / c_{sound}$ (which gives an approximate distance of the transition from near- to far-field of the sound field generated by a circular source with diameter l) and the thermal effusivity e_{film} of the heat-producing film:

$$p(r,f) = \frac{(\gamma_{gas}-1)}{c_{sound}} \cdot \frac{e_{gas}}{e_{gas}+e_{film}+e_{sub}} \cdot q_{in} \cdot \frac{R_0}{r} . \tag{1.8}$$

As one can see from Equation (1.8), the sound pressure generated by a thermophone on a substrate is assumed to be linearly dependent on the input-power density q_{in} and on the thermal-excitation frequency f. Additionally, the sound-pressure amplitude decreases (~1/r) with the distance r from thermophone. However, the approach proposed by Tian *et al.* cannot explain: i) the experimentally measured decrease of the generated sound pressure with the increase of the graphene-sheet thickness, and ii) the deviation of the generated sound pressure from the predicted linear dependence on the excitation frequency.

Two years later, in 2013, Aliev *et al.* [17] tested a 5 x 5 cm^2 tissue of carbon multi-walled nanotubes in He, Ar, Xe, N_2, air, SF_6 and Freon gases for sound generation at a constant frequency of 1.54 kHz and 1 Watt AC excitation power. They also compared the measured sound pressures with the prediction of the model of Vesterinen *et al.* (see Equation (1.6)). To measure the sound pressure generated by the tested thermophone in all gases, Aliev *et al.* used a 1/4 inch ACO-Pacific condenser microphone.

The findings of Aliev *et al.* [17] are:

- *“The sound pressure measured for polyatomic molecules somewhat deviates from the theoretical line, probably due to non-ideal gas behavior.”*
- *“The sound pressure increases linearly with the applied power for all gases.”*

In 2014, Dutta *et al.* [18] tested a thermophone consisting of a gold nano-wire array for sound generation up to 100 kHz and compared the experimental results with the predictions made from the models of Xiao *et al.* (see Equation (1.6)), Vesterinen *et al.* (see Equation (1.7)) and Tian *et al.* (see Equation (1.8)). As reported by Dutta *et al.*, *“the proofed models fit poorly the experimental data”*. The comparison of experimentally detected sound pressure levels (SPLs) with predictions made from the models of Xiao *et al.* (Equation (1.5)), Vesterinen *et al.* (Equation (1.6)) and Tian *et al.* (Equation (1.8)) show frequency-dependent deviations in a range of 6 – 25 dB. Additionally, the slope of generated sound pressure with increasing excitation frequency $p(f)$ deviates from both, the linear and the square-root dependence, that are predicted from the tested models.

1.3 Summary and discussion

Concluding this chapter, let us summarize and discuss the theoretical and experimental findings on the thermophones of the last hundred years:

i) To the best of the author's knowledge, all the theoretical models for thermophonic sound generation in gases that have been published up to now [2,5,6,8-11,15-17] (see chapter 1.2, Equations (1.1) – (1.8)) are based on the assumption of an expansion and contraction of the gas layer adjacent to the periodically heated surface. Supposedly, this gas layer acts like a moving piston and its movement causes the emergence of the sound waves.

ii) All existing models have different constants and parameters for modeling either free-standing or substrate-based thermophones and can be classified into two categories according to their origin:

   a) The models of Arnold and Crandall [2] and of Xiao *et al.* [8,9] are based on a time-dependent system of coupled partial differential equations (PDE) for temperature and pressure:

$$\begin{cases} \dfrac{\partial T_{film}}{\partial t} = (P_{power}(t) - 2 \cdot S_{film} \cdot \beta_{gas} \cdot T_{film}) / (d_{film} \cdot S_{film} \cdot \rho_{film} \cdot c_{p\,film}) \\ \dfrac{\partial p_{gas}}{\partial t} = \dfrac{\partial T_{film}}{\partial t} \cdot \dfrac{P_{0\,gas}}{T_{0\,gas}} \end{cases} \tag{1.9}$$

   The PDE-system (Equation (1.9)) focuses on the temperature variation of the electrically conductive film, assumes a diffusive heat flux into the adjacent gas and considers the heat capacity of the heat-producing film as a frequency-independent parameter. As can be seen when considering the solutions of Arnold and Crandall and Xiao et al. (see Equations (1.1),(1.4)), the PDE-system yields a linear dependence on the supplied electric power and a square-root dependence on the excitation frequency for the thermally generated sound pressure.

   Arnold and Crandall [2] as well as Xiao et al. [8,9] concluded that the electrically conductive film has to be very thin and should have a small heat capacity per unit area.

   b) The models of Shinoda *et al.* [5], Boullosa *et al.* [6], Tian *et al.* [11], Vesterinen *et al.* [15] and of Hu *et al.* [16] are based on a time-dependent system of coupled PDEs for temperature and pressure originally developed by McDonald and Wetzel [14] for closed photo-acoustic cells of a constant volume V_{gas} excited with a light beam of power $P_{in}(t)$:

$$\begin{cases} \nabla^2 p_{gas} - \dfrac{\gamma_{gas}}{c_{sound}^2} \dfrac{\partial^2 p_{gas}}{\partial t^2} = -\dfrac{(\gamma_{gas} - 1) \cdot \rho_{gas} \cdot c_{p\,gas}}{c_{sound}^2} \dfrac{\partial^2 T_{gas}}{\partial t^2} \\ \lambda_{gas} \nabla^2 T_{gas} - \rho_{gas} \cdot c_{p\,gas} \dfrac{\partial T_{gas}}{\partial t} + \dfrac{P_{in}(t)}{V_{gas}} = -\dfrac{\partial p_{gas}}{\partial t} \end{cases} \tag{1.10}$$

   This PDE-system (Equation (1.10)) includes no electrically conductive films at all and considers only an adiabatic increase of pressure at a constant volume of a gas-filled cell.

Hence, all resulting approaches are, contrary to the models of category (a), independent of the thickness and the heat capacity of the electrically conductive film.

iii) The theoretically predicted dependence of the generated sound pressure on the excitation frequency varies from model to model between a square-root dependence $f^{0.5}$ (Arnold and Crandall, Xiao *et al.*), a linear dependence on f (Vesterinen *et al.*, Aliev *et al.*, Tian *et al.*) or a frequency independence in the models of Shinoda *et al.* and Hu *et al.*.

iv) All models predict a linear dependence of the generated sound pressure on the excitation power.

v) Only the models of Boullosa *et al.* [6] and Tian *et al.* [11] take into account the size of the thermophone and thus yield approaches for the acoustical far-field.

vi) All existing theoretical models neglect the distance and the frequency-dependent decrease of the generated sound pressure due to sound attenuation in the gas.

vii) Published experimental examinations of thermophones have only reported frequencies not exceeding 100 kHz.

viii) Fits of experimental results for free-hanging as well as substrate-based thermophones show that:

- the generated sound pressure increases linearly with the supplied electric power;
- experimentally detected sound pressures show either a linear or a $f^{0.7-0.8}$ dependence of the generated sound pressure on the excitation frequency, deviating from the predicted square-root dependence for free-standing thermophones.

ix) All comparisons of experimentally measured sound pressures with predictions made by existing models reported deviations between 100 and 1000 %.

x) Most experimental evaluations of thermophones and of proposed theoretical approaches were carried out in air. To the best of the author's knowledge, up to now only two experimental examinations of thermophones in gases such as He, Ar, Xe, SF_6, N_2 and Freon have been published [9,17]. In both studies, ¼ - inch condenser microphones (a B&K 4939 and an ACO-Pacific 7016) were used to measure thermally generated sound pressure. Unfortunately, these microphones are originally calibrated in air at room temperature and normal atmospheric pressure. The use of these microphones in other gases, with different values for density ρ and speed of sound c, changes the stiffness $S = \rho \cdot c^2 \cdot A/d$ of the gas-filled microphone capsule (where A is the surface of the capsule and d is the capsule height) [19]. As also discussed in [19], the change of the capsule stiffness results in a change of sensitivity and of the resonance frequencies of the microphone. Thus, all condenser microphones have to be recalibrated before being employed in other gases. However, the authors [9,17] give no indication that their microphones were recalibrated for He, Ar, Xe, SF_6, N_2 or Freon. Consequently, experimentally detected sound pressures generated by the tested thermophones in various gases [9,17] may be flawed due to the use of uncalibrated microphones.

Summing up, there is currently no model available which is able to accurately predict the sound pressure generated by thermophones in gases. Hence, a detailed theoretical analysis of the thermophonic sound generation in gases is required.

2. The Energy-Density-Function model

2.1 How does a thermophone work

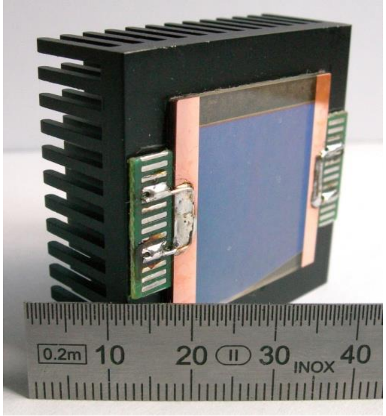

Let us consider a homogeneous, few nanometers thin, electrically conductive film of area S_{film} with a purely ohmic resistance on a smooth and homogeneous solid substrate in a semi-infinite, isotropic gaseous space.

For this three-layer setup, a formula will be derived for the amplitude of the thermally generated sound pressure depending on the time-function of the supplied electric power. Consequently, a formula will be derived for free-standing conductive wires or foils, which should also be applicable to plasma speakers.

Furthermore, the model allows for a quantitative prediction of the generated sound-field distribution around a thermo-acoustic sound source of arbitrary size, shape and material. Consequently, the model could be used in the design of thermo-acoustic sound sources for specific applications. In general, the proposed model is generalized and can also be used for the determination of the sound pressure generated in a gas by any thermal-power sources such as thermophones, plasma discharges, laser beams, chemical- or nuclear reactions.

But first the commonly used model of an imaginary gas piston is refuted and a realistic description of thermophonic sound generation in gases is given.

To understand the genesis of a thermally generated acoustic wave let us initially consider a thermophone in an ideal monatomic gas. Figure 2.1 schematically demonstrates the formation of a thermally generated pressure wave in a monatomic gas after a single pulse excitation of an electrically conductive film. The arrows schematically represent the momentum vectors of the gas particles.

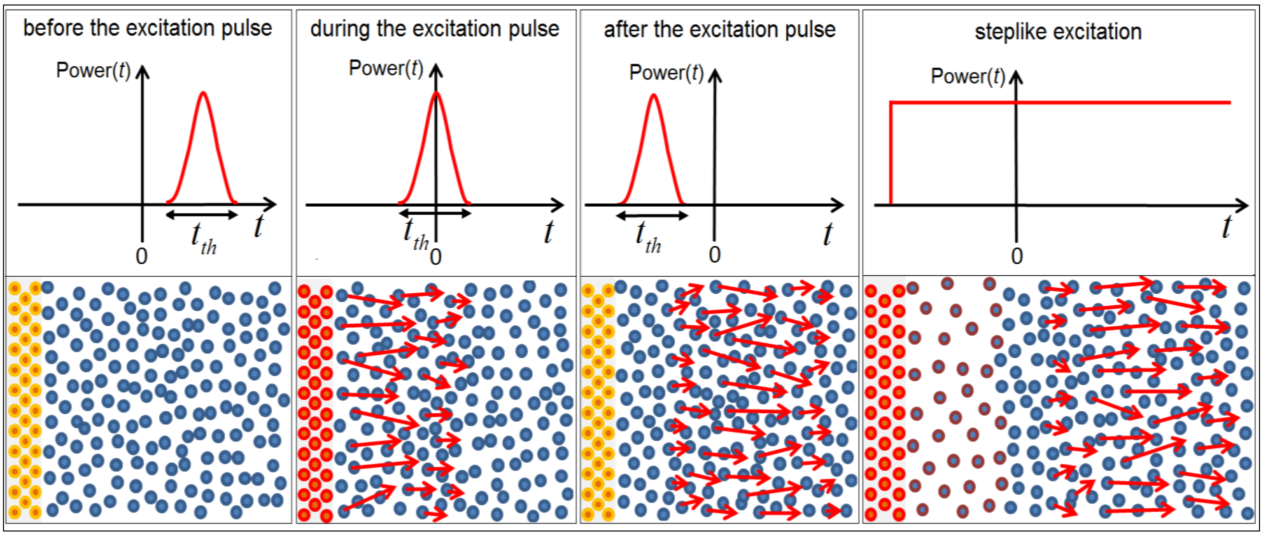

FIG. 2.1 Schematic representation of the formation of a thermally excited sound pulse and the propagation of momentum in a monatomic gas after a single power pulse (three left images) and after a steplike excitation (right image).

Before an electrical excitation impulse is applied the gas particles are in a constant random motion colliding with each other and with the surface of the electrically conductive film. Everything is in thermodynamic equilibrium.

During the electrical excitation pulse, the electrically conductive film heats up and the velocity of the film atoms increases. The adjacent gas particles bounce off the heated film atoms and take some of the heat as a momentum directed away from the heated film. The momentum propagates by collision of gas particles away from the heated thermophone surface with the speed of sound, similar to a Newton's cradle. The pressure around the thermophone increases.

After the electrical excitation pulse, the film cools down, the velocity of the atoms decreases, and everything returns to the initial thermodynamic state.

As depicted in Figure 2.1, the thermal generation of an acoustic wave, at least at high frequencies, takes place at a constant gas volume. This means that the gas volume close to the heated surface does not expand and subsequently does not store the supplied thermal energy. The quick heating of the film results in a particle-velocity wave in the adjacent gas, which propagates at the speed of sound as a sound pulse.

Only, if the film is constantly heated for a longer time, e.g. on the order of a few seconds (Figure 2.1, right image), the gas layer close to the heated surface stores the kinetic energy and expands. In this case, the thermal energy supplied to the gas is carried away with the convective gas flow, thermal diffusion and photonic emission.

Now let us consider an acoustic wave from the viewpoint of thermodynamics and derive a mathematical description of the thermal sound generation in gases.

From a thermodynamic point of view, an acoustic wave can be considered to have the following properties:

1. It is a closed thermodynamic system of finite volume V_{wave} that transports kinetic energy at the speed of sound c_{sound}.
2. The mean value of the sound pressure p_{sound} inside an acoustic wave of volume V_{wave} corresponds to the mean value of its internal energy density,

$$p_{sound} \equiv \Delta\check{U} / V_{wave}. \tag{2.1}$$

3. Given the first law of thermodynamics, the change of internal energy $\Delta\check{U}$ of a closed thermodynamic system is equal to the sum of the heat ΔQ supplied to the system and the volume-work ΔW performed on it,

$$\Delta\check{U} \equiv \Delta Q + \Delta W = \Delta Q - p_0 \cdot \Delta V_{wave} \tag{2.2}$$

where p_0 is the initial pressure in the given gas.

Conventional sound transducers, such as electro-magnetic loudspeakers, electrostatic and piezoelectric transducers, usually move in both directions and alternately compress and expand the adjacent gas adiabatically. They do not generate heat ($\Delta Q = 0$), and only perform the adiabatic volume work $\Delta W = -p_0 \cdot \Delta V$. In this way, they generate a periodic variation of internal energy $\Delta\check{U} = \Delta W$, and thus a variation of sound pressure Δp_{sound}.

Thermophones work without any macroscopic moving parts, and hence, they do not perform any mechanical volume-work $\Delta W = 0$. They only generate heat $\Delta Q = P_{el} \cdot t$ which results in the change of the internal energy $\Delta \check{U}$ of the adjacent gas particles. The local variation of the internal energy leads to a local variation of sound pressure $\Delta p_{sound} = \Delta \check{U}/V_{wave}$ and thus to an acoustic wave. The time function of the thermally generated sound pressure $p_{sound}(t)$ corresponds to the time function of the outward heat flux $\dot{Q}(t)$ and thus to the time function of the supplied electric power $P_{el}(t)$,

$$p_{sound}(t) \sim \dot{Q}(t) = P_{el}(t)\,. \tag{2.3}$$

Assuming the electrically conductive film is excited by a sinusoidal voltage without offset $U_{el}(t) = U \cdot \sin(\omega \cdot t)$, with $\omega = 2 \cdot \pi \cdot f$ and frequency f, the electric current is, therefore, also a sine function $I_{el}(t) = I \cdot \sin(\omega \cdot t)$. The converted electric power $P_{el}(t)$, which is equal to the thermal power, is the product of these two functions and has double the frequency of the originally supplied voltage and current,

$$P_{el}(t) = U \cdot \sin(\omega \cdot t) \cdot I \cdot \sin(\omega \cdot t) = U \cdot I \cdot \sin^2(\omega \cdot t) = U \cdot I \cdot \big(1 - \cos(2 \cdot \omega \cdot t)\big)/2\,. \tag{2.4}$$

In this case, the effective value of the electric power corresponds to half of the product of the voltage and current amplitudes

$$P_{el\,eff} = U \cdot I / 2\,, \tag{2.5}$$

and the thermal excitation frequency is $f_{th} = 2 \cdot f$. The doubling of frequency, when a sinusoidal voltage without offset is applied, is a characteristic property of a thermophone.

When the film is excited by a sinusoidal voltage with offset $U_{el}(t) = U \cdot (1 + \sin(\omega \cdot t))$, the electric current is $I_{el}(t) = I \cdot (1 + \sin(\omega \cdot t))$, and the corresponding electric power

$$\begin{aligned} P_{el}(t) &= U \cdot \big(1 + \sin(\omega \cdot t)\big) \cdot I \cdot \big(1 + \sin(\omega \cdot t)\big) = U \cdot I \cdot \big(1 + \sin(\omega \cdot t)\big)^2 \\ &= U \cdot I \cdot \big(1 + 2 \cdot \sin(\omega \cdot t) - \big(1 - \cos(2 \cdot \omega \cdot t)\big)/2\big) \\ &= U \cdot I \cdot \big(1 + 4 \cdot \sin(\omega \cdot t) + \cos(2 \cdot \omega \cdot t)\big)/2 \end{aligned} \tag{2.6}$$

contains the excitation frequency $\sin(\omega \cdot t)$ and its first harmonic $\cos(2 \cdot \omega \cdot t)$. Hence, for the generation of a single-frequency tone free from any harmonic distortion, a thermophone should be driven by a sinusoidal voltage without offset and at half of the desired frequency.

Figure 2.2 shows examples of the electric power and the sound pressures for both kinds of excitation.

If an alternating electric power converted inside the film has a constant offset larger than the alternating amplitude, e.g. $P_{el}(t) = P_{ac} \cdot (1 + \sin(\omega \cdot t)) + P_{dc}$, only the alternating part P_{ac} is converted into acoustic waves. The DC-part P_{dc} of the electric power constantly heats the film, the substrate and the surrounding gas, and the resulting thermal energy is removed by photon emission, heat conduction and convection.

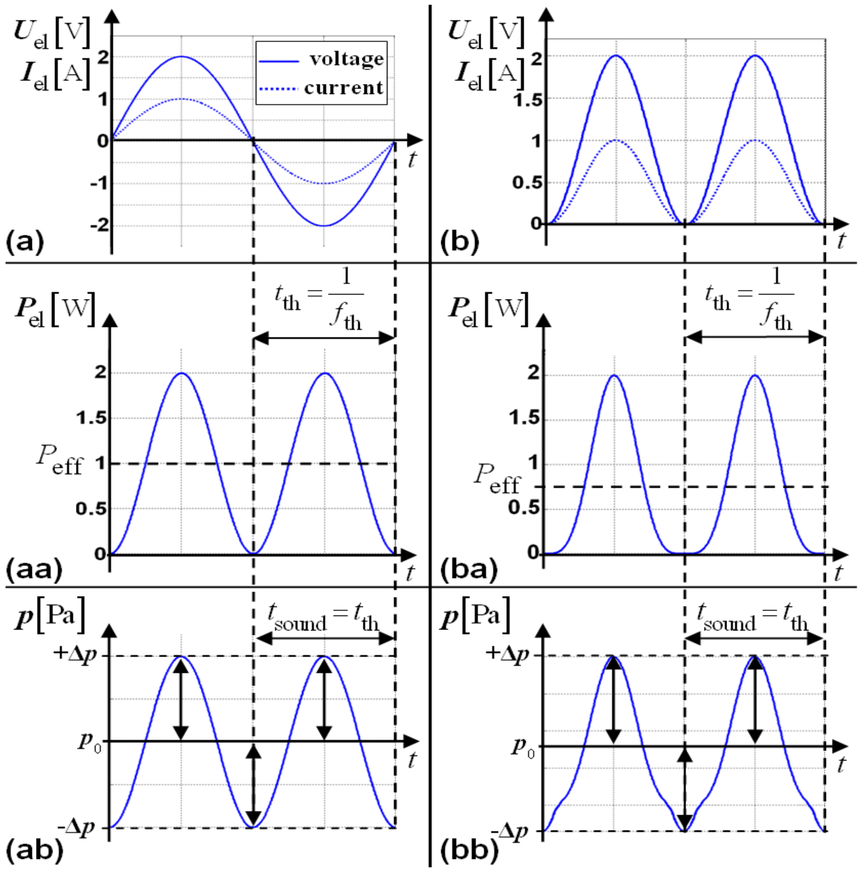

FIG. 2.2 Time profiles of electric power (aa, ba) and of the corresponding sound pressures (ab, bb) for **(a)** sinusoidal excitation without offset $U_{el}(t) = U \cdot \sin(\omega \cdot t)$ and **(b)** sinusoidal excitation with offset $U_{el}(t) = U \cdot (1+\sin(\omega \cdot t))$.

Another important point is that the pressure amplitude of the acoustic wave depends on the instantaneous thermodynamic state of the electrically conductive film and the adjacent matter. That is, when the film, the surrounding gas, and the substrate are at a certain constant temperature $T_0 \sim \check{U}_0$, an excitation with a single power pulse generates a single "positive" pressure pulse (see Figure 2.1). When the thermophone is excited with a continuous sinusoidal electric power with a constant effective value P_{eff}, the film, the substrate and thus also the surrounding gas close to the thermophone will all be heated. After reaching the thermodynamic equilibrium temperature T_{eq} (for determination of T_{eq} see Appendix A), the thermophone generates positive and negative pressure changes like a conventional sound transducer (see Figure 2.2(ab)). The reason for this behavior is that the internal energy of the heat producing film, the adjacent substrate and the gas now oscillates around the equilibrium value of internal energy $\check{U}_{eq} \sim Q_{eff} \sim P_{eff}$, and hence $\Delta\check{U}(t) = Q_{eff} \cdot \sin(\omega \cdot t)$ has "negative" and "positive" parts.

Summing up and following Equation (2.1) $\Delta p_{sound}(t_{th}) = \Delta Q_{gas}(t_{th})/V_{wave}(t_{th})$, for a quantitative determination of the thermally generated sound pressure in a gas during a heating period t_{th}, we need to determine:

i) the amount of heat $\Delta Q_{gas}(t_{th})$ supplied to the gas during one heating period t_{th}, and

ii) the volume of the acoustic wave $V_{wave}(t_{th})$ in the respective radiation direction.

2.2 Calculation of the amount of thermal energy flowing into the gas

To calculate the amount of thermal energy flowing into the gas, we first have to calculate the total thermal energy $Q_{th\,in}$ produced during the heating period t_{th}.

In general

$$Q_{th\,in} = \int_0^{t_{th}} P_{el}(t) \cdot dt \,, \tag{2.7}$$

but, assuming a sinusoidal power function $P_{el}(t)$, a simplified equation for the amount of heat generated during one heating period t_{th} can be obtained using the effective value of the supplied electric power $P_{el\,eff}$

$$Q_{th\,in} = P_{el\,eff} \cdot t_{th} = \frac{P_{el\,eff}}{f_{th}} \tag{2.8}$$

The heating of the conductive film leads to photon emission and to a heat flux into adjacent gas and substrate layers, leading to the energy balance

$$Q_{th\,in} = Q_{film\,th} + Q_{sub\,th} + Q_{gas\,th} + Q_{photons\,th}. \tag{2.9}$$

For a film surface area S_{film} that is smaller than a few square centimeters and high-frequency (e.g. > 10 kHz) temperature oscillations of the conductive film up to 100 °C, less than 0.1 % of the input energy $Q_{th\,in}$ is converted into photon emission $Q_{photons\,th}$ during one heating period t_{th} (for determination of $Q_{photons\,th}$ see Appendix B). Thus, the energy transported by photons $Q_{photons\,th}$ can initially be disregarded and the energy balance can be simplified as

$$Q_{th\,in} = Q_{film\,th} + Q_{sub\,th} + Q_{gas\,th}. \tag{2.10}$$

The amounts of thermal energy distributed between the electrically conductive film ($Q_{film\,th}$), the substrate ($Q_{sub\,th}$) and the gas ($Q_{gas\,th}$) are proportional to the respective thermal capacities (see Figure 2.3). This analogy to the capacity for storing electric charges is well established and is an often-used tool for solving heat-transfer problems.

The thermal capacity of the electrically conductive film C_{film} is equal to the product of its thickness d_{film}, surface area S_{film}, specific heat capacity $c_{p\,film}$ and density ρ_{film}:

$$C_{film} = d_{film} \cdot S_{film} \cdot \rho_{film} \cdot c_{p\,film} \,. \tag{2.11}$$

Note that for electrical excitation of the conductive film at frequencies up to 2 MHz the electrical skin effect can be neglected, which gives a penetration depth for the electrical current e.g. in titanium, aluminum and gold, on the order of about 60 – 80 µm. Thus, a homogeneous electric current distribution along across the electrically conductive film, and hence a homogeneous heating of the film, can be assumed.

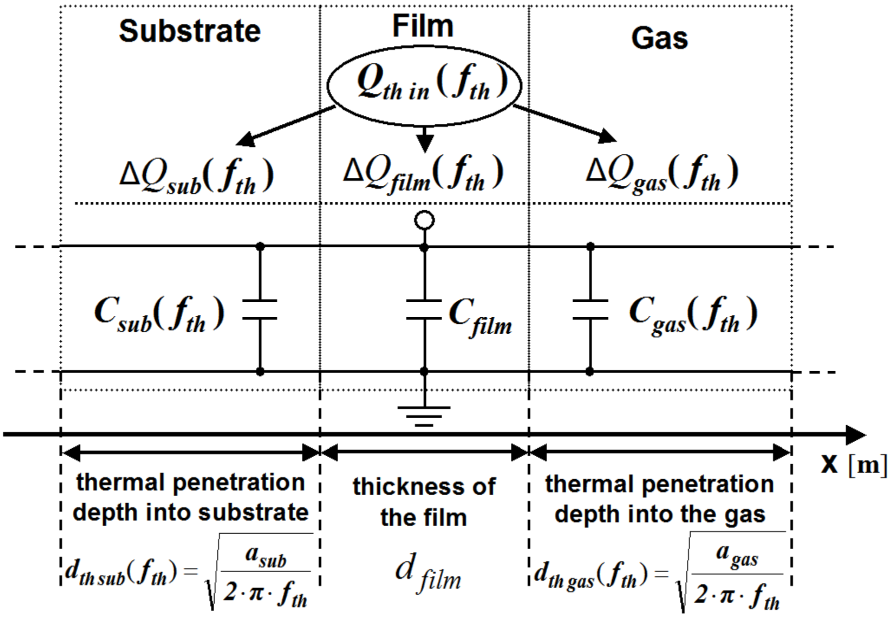

FIG. 2.3 Distribution of the thermal energy $Q_{th\,in}(f_{th})$ generated inside an electrically conductive film.

The heat capacities of the adjacent gas (C_{gas}) and substrate (C_{sub}) layers depend on the respective densities, specific heat capacities and frequency-dependent thermal penetration depths $d_{th}(f_{th})$ given by

$$d_{th}(f_{th})=\sqrt{\frac{a_{diffusion}}{2\cdot\pi\cdot f_{th}}} \tag{2.12}$$

where $a_{diffusion}=\lambda/\rho\cdot c_v$ is the thermal diffusivity of the given material at a constant volume, and f_{th} is the heating frequency.

Thus, we obtain for the frequency-dependent heat capacity of the adjacent gas

$$\begin{aligned}C_{gas}(f_{th})&=d_{th\;gas}(f_{th})\cdot S_{film}\cdot\rho_{gas}\cdot c_{v\,gas}=\sqrt{\frac{a_{gas}}{2\cdot\pi\cdot f_{th}}}\cdot S_{film}\cdot\rho_{gas}\cdot c_{v\,gas}\\&=\sqrt{\frac{\lambda_{gas}}{\rho_{gas}\cdot c_{v\,gas}\cdot 2\cdot\pi\cdot f_{th}}}\cdot S_{film}\cdot\rho_{gas}\cdot c_{v\,gas}=\sqrt{\frac{\lambda_{gas}\cdot\rho_{gas}\cdot c_{v\,gas}}{2\cdot\pi\cdot f_{th}}}\cdot S_{film}=\frac{e_{gas}\cdot S_{film}}{\sqrt{2\cdot\pi\cdot f_{th}}},\end{aligned} \tag{2.13}$$

with thermal diffusivity $a_{gas}=\lambda_{gas}/\rho_{gas}\cdot c_{v\,gas}$ and thermal effusivity $e_{gas}=\sqrt{\lambda_{gas}\cdot\rho_{gas}\cdot c_{v\,gas}}$ of the adjacent gas, where λ_{gas} is the heat conductivity, ρ_{gas} the density and $c_{v\;gas}$ the isochoric heat capacity of the gas.

As the heat transfer from the periodically heated film into the adjacent gas takes place at a constant gas volume, one has to use the isochoric heat capacity $c_{v\,gas}$ for calculating the thermal effusivity e_{gas} of the gas.

For most solid materials, the isochoric heat capacity is equal to the isobaric heat capacity. Hence, the isobaric heat capacity $c_{p\;sub}$ can be used to calculate the heat capacity of the substrate,

$$C_{sub}(f_{th}) = d_{th\,sub}(f_{th}) \cdot S_{film} \cdot \rho_{sub} \cdot c_{p\,sub} = \sqrt{\frac{a_{sub}}{2 \cdot \pi \cdot f_{th}}} \cdot S_{film} \cdot \rho_{sub} \cdot c_{p\,sub}$$

$$= \sqrt{\frac{\lambda_{sub}}{\rho_{sub} \cdot c_{p\,sub} \cdot 2 \cdot \pi \cdot f_{th}}} \cdot S_{film} \cdot \rho_{sub} \cdot c_{p\,sub} = \sqrt{\frac{\lambda_{sub} \cdot \rho_{sub} \cdot c_{p\,sub}}{2 \cdot \pi \cdot f_{th}}} \cdot S_{film} = \frac{e_{sub} \cdot S_{film}}{\sqrt{2 \cdot \pi \cdot f_{th}}}, \tag{2.14}$$

with thermal diffusivity $a_{sub} = \lambda_{sub} / \rho_{sub} \cdot c_{p\,sub}$ and thermal effusivity $e_{sub} = \sqrt{\lambda_{sub} \cdot \rho_{sub} \cdot c_{p\,sub}}$, where λ_{sub} is the heat conductivity, ρ_{sub} the density and $c_{p\,sub}$ the specific heat capacity of the substrate material.

As already mentioned, the distribution of the thermal energy is proportional to the frequency-dependent thermal capacities of the film, the gas and the substrate. Thus, the amount of thermal energy flowing out from the heat-producing film into the substrate and the gas $Q_{out\,th} = Q_{gas\,th} + Q_{sub\,th}$ is related to the total generated energy $Q_{th\,in} = Q_{film\,th} + Q_{sub\,th} + Q_{gas\,th}$ by

$$\frac{Q_{out\,th}(f_{th})}{Q_{th\,in}(f_{th})} = \frac{Q_{gas\,th}(f_{th}) + Q_{sub\,th}(f_{th})}{Q_{th\,in}(f_{th})} = \frac{C_{gas}(f_{th}) + C_{sub}(f_{th})}{C_{gas}(f_{th}) + C_{sub}(f_{th}) + C_{film}}, \tag{2.15}$$

and

$$Q_{out\,th}(f_{th}) = Q_{gas\,th}(f_{th}) + Q_{sub\,th}(f_{th}) = Q_{th\,in}(f_{th}) \cdot \frac{C_{gas}(f_{th}) + C_{sub}(f_{th})}{C_{gas}(f_{th}) + C_{sub}(f_{th}) + C_{film}}. \tag{2.16}$$

The ratio between the thermal energy flowing into the gas ($Q_{gas\,th}$) and the amount of thermal energy flowing outwards the heat producing film ($Q_{out\,th}$) is given by

$$\frac{Q_{gas\,th}(f_{th})}{Q_{out\,th}(f_{th})} = \frac{Q_{gas\,th}(f_{th})}{Q_{gas\,th}(f_{th}) + Q_{sub\,th}(f_{th})} = \frac{C_{gas}(f_{th})}{C_{gas}(f_{th}) + C_{sub}(f_{th})}. \tag{2.17}$$

Substituting Equation (2.16) into Equation (2.17) yields the amount of thermal energy $Q_{gas\,th}$ flowing into the adjacent gas during one period $t_{th} = 1/f_{th}$ of the periodical heating:

$$\begin{aligned} Q_{gas\,th}(f_{th}) &= Q_{out\,th}(f_{th}) \cdot \frac{C_{gas}(f_{th})}{C_{gas}(f_{th}) + C_{sub}(f_{th})} \\ &= Q_{th\,in}(f_{th}) \cdot \frac{C_{gas}(f_{th}) + C_{sub}(f_{th})}{C_{gas}(f_{th}) + C_{sub}(f_{th}) + C_{film}} \cdot \frac{C_{gas}(f_{th})}{C_{gas}(f_{th}) + C_{sub}(f_{th})} \\ &= Q_{th\,in}(f_{th}) \cdot \frac{C_{gas}(f_{th})}{C_{gas}(f_{th}) + C_{sub}(f_{th}) + C_{film}}. \end{aligned} \tag{2.18}$$

Substituting Equations (2.11), (2.13) and (2.14) for C_{film}, $C_{gas}(f_{th})$ and $C_{sub}(f_{th})$ into Equation (2.18) results in

$$Q_{gas\ th}(f_{th}) = Q_{th\ in}(f_{th}) \cdot \frac{e_{gas}}{e_{gas} + e_{sub} + d_{film} \cdot \rho_{film} \cdot c_{p\ film} \cdot \sqrt{2 \cdot \pi \cdot f_{th}}}. \tag{2.19}$$

The frequency dependent term $d_{film} \cdot \rho_{film} \cdot c_{p\ film} \cdot (2 \cdot \pi \cdot f_{th})^{0.5}$ in Equation (2.19) can be considered as the “thermal inertia” of the heat producing film, where d_{film} is the thickness of the film and ρ_{film} and $c_{p\ film}$ are its density and specific heat capacity, respectively. Due to its frequency dependence, the heat capacity of the heat producing film acts as a thermal low-pass filter, reducing non-linearly the amount of thermal energy flowing into the gas and substrate during a heating period and hence reducing the generated sound pressure with increasing the heating frequency f_{th} of the periodical heating.

Additionally, one must not forget that all thermodynamic variables and parameters depend on temperature T and pressure P.

For further simplification, let us now define the energy distribution function $E_{gas}(T,P, f_{th})$ for the gas as

$$E_{gas}(T,P,f_{th}) = \frac{e_{gas}(T,P)}{e_{gas}(T,P) + e_{sub}(T,P) + I_{film\ th}(T,P,f_{th})} \tag{2.21}$$

where $e_{gas}(T,P)$ and $e_{sub}(T,P)$ are the thermal effusivities of gas and substrate at some given temperature T and pressure P, and $I_{film\ th}(T,P,f_{th})$ is the thermal inertia of the heated film given by

$$I_{film\ th}(T,P,f_{th}) = d_{film}(T,P) \cdot \rho_{film}(T,P) \cdot c_{p\ film}(T,P) \cdot \sqrt{2 \cdot \pi \cdot f_{th}}\ . \tag{2.22}$$

As one can see in equation (2.21), the distribution of thermal energy produced during one heating period $t_{th} = 1/\ f_{th}$ depends on thermal effusivities of the gas $e_{gas}(T,P)$ and substrate $e_{sub}(T,P)$ and on the heating-frequency dependent thermal inertia of the heat producing film $I_{film\ th}(T,P,f_{th})$.

It is obvious that the energy distribution function $E_{gas}(T,P,f_{th})$ (see Equation (2.21)) and thus the proposed model apply also for free-standing films and wires when inserting $e_{sub}(T,P) = e_{gas}(T,P)$.

Furthermore, the energy distribution function $E_{gas}(T,P,f_{th})$ can also be applied to plasma sound sources when considering the plasma discharge as an electrically heated conductor with thickness d, density ρ and heat capacity c_v.

Summing up, we obtain for the amount of thermal energy flowing into the gas during the heating period t_{th} if we ignore the photon emission:

$$Q_{gas\ th}(T,P,f_{th}) = Q_{th\ in}(f_{th}) \cdot E_{gas}(T,P,f_{th}) \tag{2.23}$$

and if we include the photon emission $Q_{photon}(f_{th})$, we obtain

$$Q_{gasth}(T,P,f_{th}) = \left(Q_{th\ in}(f_{th}) - Q_{photon}(f_{th})\right) \cdot E_{gas}(T,P,f_{th})\ . \tag{2.24}$$

Note that for smaller thermophone surfaces (e.g. 10 – 20 cm^2) and higher-frequency (> 10 kHz) temperature oscillations of the conductive film up to 500 °C, the loss of thermal energy is at most 0.1 % of the input energy and can thus be neglected (for calculation of the energy Q_{photon} transported by photons see Appendix B). For low-frequency excitations (< 1 kHz), the part of the thermal energy converted into photon radiation can reach up to a few percent of the thermal-energy input and hence has to be taken into account.

Additionally, as was already discussed in Section 2.1, one has to distinguish between single-pulse excitation and continuous sinusoidal excitation when the thermophone has reached its equilibrium temperature. Figure 2.4 schematically shows the differences between these two excitation types.

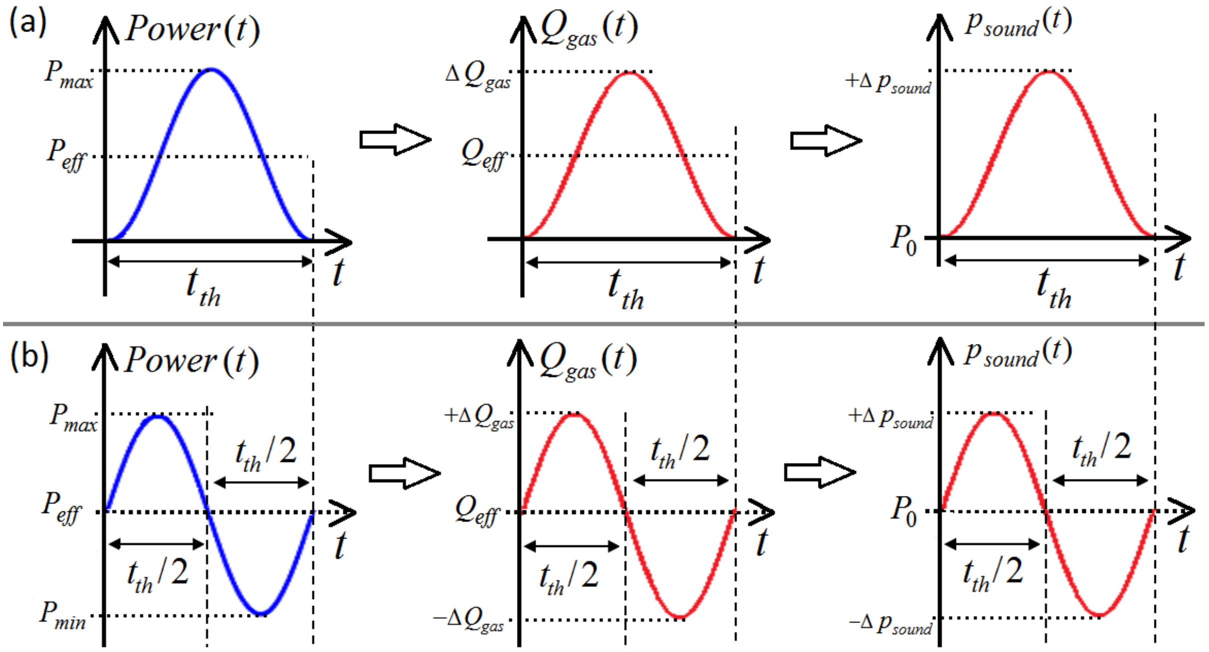

FIG. 2.4 Schematic representation of the time functions of the supplied electric power $Power(t)$, the thermal energy flowing into the gas $Q_{gas}(t)$ and the resulting sound pressure $p_{sound}(t)$ for **(a)** sinusoidal pulse excitation with a period t_{th} and **(b)** continuous sinusoidal excitation with the same period duration t_{th} and the same peak-to-peak electric power. P_0 represents the ambient atmospheric pressure.

As one can see from Figure 2.4, if single excitation pulse is applied there is only the “heating time” which is equal to t_{th}; if a continuous sinusoidal excitation without offset is applied there are the “heating time” and the “cooling time”, and both are equal to $t_{th}/2$.

Thus we get for the amount of thermal energy flowing into the adjacent gas:

i) for single-pulse excitation

$$\begin{aligned}\Delta Q_{gas\,pulse}(T,P,f_{th}) &= \left(Q_{th\ in}(f_{th}) - Q_{photon}(f_{th})\right)\cdot E_{gas}(T,P,f_{th}) \\ &= \left(\frac{P_{eff}}{f_{th}} - \frac{P_{photon}}{f_{th}}\right)\cdot E_{gas}(T,P,f_{th}) \quad ,\end{aligned} \tag{2.25}$$

ii) and for a continuous sinusoidal excitation at the frequency f_{th} with constant amplitude

$$\begin{aligned}\Delta Q_{gassinus}(T,P,f_{th}) &= \left(Q_{th\ in}(f_{th}) - Q_{photon}(f_{th})\right)\cdot E_{gas}(T,P,f_{th}) \\ &= \left(\frac{P_{eff}}{2\cdot f_{th}} - \frac{P_{photon}}{2\cdot f_{th}}\right)\cdot E_{gas}(T,P,f_{th})\end{aligned} \qquad (2.26)$$

Now, following Equation (2.1), $\Delta p_{sound}\ (t_{th}) = \Delta Q_{gas}\ (t_{th})\ /\ V_{wave}\ (t_{th})$, we have to calculate the volume of the generated acoustic wave for determining the thermally generated sound pressure.

2.3 Calculation of the volume of the resulting acoustic wave

In the following, let us assume an acoustical point source. That means the film size is at least five times smaller than the length of the generated acoustic wave. Furthermore, let us assume a large, planar and homogeneous substrate, and a homogeneous and isotropic surrounding gas.

Because pressure fluctuations propagate at the speed of sound (supersonic propagation, as caused for example by explosions, is not included and has to be treated separately), the volume of the resulting acoustic wave depends on the speed of sound in the given gas $c_{sound}(T,P)$ and the "heating time" t_{th}.

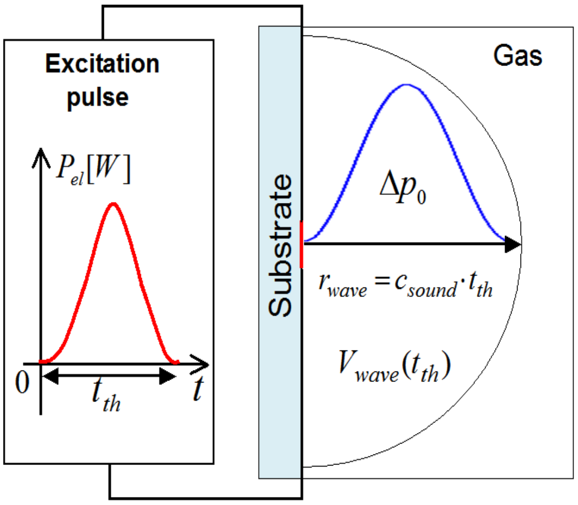

FIG. 2.5 Schematic representation of the formation of a longitudinal acoustic wave in a gas after pulse excitation with a sinusoidal semicycle of period t_{th}.

Figure 2.5 schematically shows the propagation of an acoustic wave away from the heated "point source" as a spherical longitudinal wave. During the "heating time" t_{th}, it fills a half sphere of volume $V_{wave\ th}$ with radius $r_{wave} = c_{sound} \cdot t_{th}$, and the volume of the generated acoustic wave is

$$V_{wave\ pulse}(T,P,f_{th}) = \frac{4}{3}\cdot\pi\cdot(c_{sound}(T,P)\cdot t_{th})^3/2 = \frac{2}{3}\cdot\pi\cdot(c_{sound}(T,P)/f_{th})^3\,. \qquad (2.27)$$

When calculating the volume of the resulting acoustic wave, one has to distinguish between single-pulse excitation and continuous sinusoidal excitation. Hence, if a thermophone is supplied with continuous sinusoidal power of frequency f_{th} the "heating time" is equal to $t_{th}/2$ and the volume of the generated acoustic wave is

$$V_{wave\ sinus}(T,P,f_{th}) = \frac{4}{3}\cdot\pi\cdot(c_{sound}(T,P)\cdot t_{th}/2)^3/2 = \frac{1}{12}\cdot\pi\cdot(c_{sound}(T,P)/f_{th})^3\,. \qquad (2.28)$$

2.4 Determination of the sound-pressure amplitude generated by a thermo-acoustic point source at an arbitrary observation point in an ideal gas

The amplitude of the sound pressure generated by a thermophone in an ideal gas at temperature T and pressure P follows from Equation (2.1),

$$\Delta p(T,P,f_{th}) = \frac{\Delta Q_{gas}(T,P,f_{th})}{V_{wave}(T,P,f_{th})} . \tag{2.29}$$

The amplitude of the sound pressure of a spherical wave generated by an acoustic “point source” decreases with the inverse distance law as

$$\Delta p(r) = \Delta p(r_0) \cdot \frac{r_0}{r} , \tag{2.30}$$

where r_0 is the initial position of the generated acoustic wave and r the distance to the observation point.

As depicted in Figure 2.6, the initial position of the generated acoustic wave corresponds to half of the radius of the acoustic wave and is given by

$$r_{0\,pulse}(T,P,f_{th}) = \frac{c_{sound}(T,P) \cdot t_{th}}{2} = \frac{c_{sound}(T,P)}{2 \cdot f_{th}} \tag{2.31}$$

for pulse excitation and

$$r_{0\,sinus}(T,P,f_{th}) = \frac{c_{sound}(T,P) \cdot t_{th}}{4} = \frac{c_{sound}(T,P)}{4 \cdot f_{th}} \tag{2.32}$$

for continuous sinusoidal excitation.

Summing up the previous sections, we have for the amplitude of thermally generated sound pressure at a distant observation point r in an ideal gas at temperature T and pressure P

$$\Delta p(T,P,f_{th},r) = \frac{\Delta Q_{gas}(T,P,f_{th})}{V_{wave}(T,P,f_{th})} \cdot \frac{r_0(T,P,f_{th})}{r} . \tag{2.33}$$

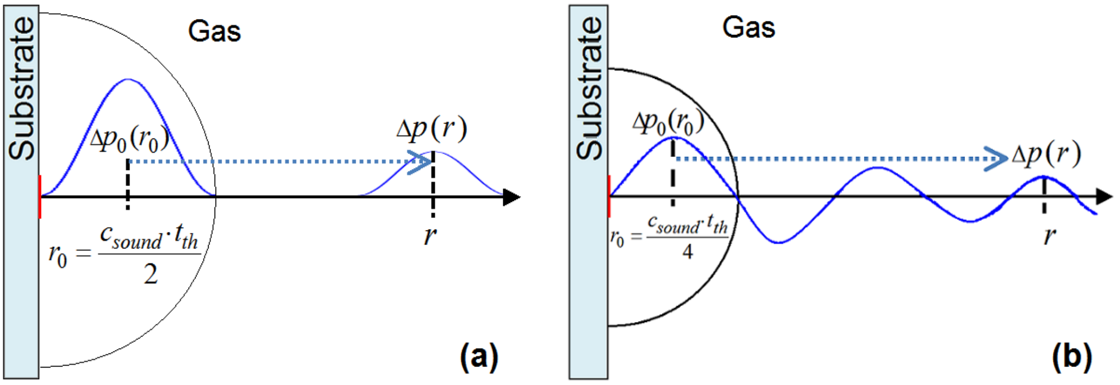

FIG. 2.6 Schematic representation of the initial position r_0 of a generated acoustic wave for: **(a)** pulse excitation and **(b)** continuous sinusoidal excitation at the same thermal excitation frequency f_{th}.

2.5 Thermophonic sound generation in a real gas

Now let us consider a real gas. Contrary to an ideal gas, for real gas atoms and molecules, the following is valid:

i) more than three degrees of freedom (DoFs);

ii) real gas particles have a nonzero volume and are compressible;

iii) there are small attractive and repulsive interaction forces between the real gas particles;

iv) collisions of real gas particles are inelastic;

v) the interaction forces between the real gas particles together with inelastic collisions result in the dissipation of the particle momentum and thus in the attenuation of a propagating acoustic wave.

Hence, in order to accurately predict thermally generated sound pressure in real gases, all these aspects have to be taken into account.

Let us start with the distribution of the thermal energy $\Delta Q_{gas\ th}$ supplied to a gas on the DoFs of the gas molecules.

The thermal energy $\Delta Q_{gas\ th}$ flowing into the gas will distribute over all available molecular DoFs (equipartition theorem of thermodynamics). In general, these can be translational, rotational, vibrational, electronic or nuclear DoFs

$$\Delta Q_{gas\ th}(T,P) = Q_{transl}(T,P) + Q_{rot}(T,P) + Q_{vibr}(T,P) + Q_{electron}(T,P) + Q_{nucleus}(T,P). \quad (2.34)$$

How many DoFs of a gas molecule have to be taken into account, depends on the number of atoms forming the molecule, the shape of the molecule and of course on the gas temperature and pressure. For example, the atoms of all monatomic gases at room temperature and normal pressure have only the three translational DoFs. Diatomic molecules, like for example, air molecules (N_2, O_2) have in total five (three translational and two rotational) DoFs, the remaining DOFs are mostly “frozen out” and hence are inactive at this temperature. With an increase of the gas temperature, activation of the vibronic, electronic and nuclear DoFs occurs, and the heat capacity of the gas molecules increases. However, only the translational movement of atoms and molecule and thus only the translational DoFs results in an acoustic wave. Therefore, the ratio of the three translational DoFs ($F_{transl} = 3$) to the total number of all available DoFs ($F_{DoFs}(T,P)$) of the gas molecule at a given gas temperature and pressure have to be taken into account.

Thus, following the Equation (2.33) for sound pressure generated in an ideal gas and taking into account the amount of available DoFs of the real gas molecule we obtain

$$\Delta p(T,P,f_{th},r) = \left[\frac{\Delta Q_{gas}(T,P,f_{th})}{V_{wave}(T,P,f_{th})} \cdot \frac{3}{F_{DoFs}(T,P)} \right] \cdot \frac{r_0(T,P,f_{th})}{r}. \quad (2.35)$$

For the calculation of the total number of available DoFs $F_{DoFs}(T,P)$ in a given gas its isobaric heat capacity $c_{v\ gas}(T,P)$, its molar mass M_{gas} and the universal gas constant R_{gas} = 8.3144598(48) J/K·mol can be used [20]

$$F_{DoFs}(T,P) = 2 \cdot \frac{c_{v\,gas}(T,P) \cdot M_{gas}}{R_{gas}} \,. \tag{2.36}$$

Now let us take into account the finite non-zero volume of the gas particles inside the acoustic wave. For this purpose, the gas-specific van-der-Waals constant b can be used. It describes the volume occupied by the gas particles in a mol of a given gas. Thus, we obtain for thermally generated sound pressure in a real gas

$$\Delta p(T,P,f_{th},r) = \left[\frac{\Delta Q_{gas}(T,P,f_{th})}{V_{wave}(T,P,f_{th}) \cdot \left(1 - b \cdot \frac{\rho_{gas}(T,P)}{M_{gas}} \right)} \cdot \frac{3}{F_{DoFs}(T,P)} \right] \cdot \frac{r_0(T,P,f_{th})}{r} , \tag{2.37}$$

where $\rho_{gas}(T,P)$ and M_{gas} are the density and the molar mass of the gas, respectively.

At this point, I would like to stress that, strictly speaking, the volume excluded by the gas particles depends on gas temperature and pressure. As the van-der-Waals constant b is pressure- and temperature-independent, it describes the reality inaccurately. For gases at small and moderate pressures up to a few bar, the impact of this parameter is very small (about 0.5 % or less), but it can increase with the increase of gas pressure und gas density.

Next, let us incorporate the reduction of the sound-pressure amplitude due to sound attenuation:

$$\Delta p(T,P,f_{th},r) = \left[\frac{\Delta Q_{gas}(T,P,f_{th})}{V_{wave}(T,P,f_{th}) \cdot \left(1 - b \cdot \frac{\rho_{gas}(T,P)}{M_{gas}} \right)} \cdot \frac{3}{F_{DoFs}(T,P)} \right] \cdot \frac{r_0(T,P,f_{th})}{r} \cdot A(T,P,r,f_{th}). \tag{2.38}$$

The function $A(T,P,r,f_{th})$ describes the distance- and frequency-dependent decrease of the sound-pressure amplitude due to sound attenuation and is given by

$$A(T,P,r,f_{th}) = exp\left[-\alpha(T,P,f_{th}) \cdot r \right], \tag{2.39}$$

where $\alpha(T, P, f_{th})$ is the material-specific sound-attenuation coefficient.

To calculate the sound-attenuation coefficient $\alpha(T,P,f_{th})$ in gases, the Stokes-Kirchhoff model for compressible gases and fluids can be applied

$$\alpha(T,P,f_{th}) = \frac{(2 \cdot \pi \cdot f_{th})^2}{2 \cdot \rho_{gas}(T,P) \cdot c^3_{sound}(T,P)} \cdot \left[\frac{4}{3} \mu_{dyn}(T,P) + \mu_{bulk}(T,P) + \left(\frac{\lambda_{gas}(T,P)}{c_{v\,gas}(T,P)} - \frac{\lambda_{gas}(T,P)}{c_{p\,gas}(T,P)} \right) \right] , \tag{2.40}$$

where μ_{dyn} is the dynamic viscosity (also called shear viscosity), μ_{bulk} is the bulk viscosity of the gas (also called volume viscosity), λ_{gas} is the heat conductivity and $c_{v\,gas}$ and $c_{p\,gas}$ are its isochoric and isobaric heat capacities, respectively. The viscosities μ_{dyn} and μ_{bulk} are important for the description of the attenuation of sound waves in real gases.

The dynamic viscosity μ_{dyn} describes the loss of kinetic energy due to the interaction between the real gas particles in terms of shear viscosity. The bulk viscosity μ_{bulk} describes the loss of kinetic energy due to inelastic collisions and due to the compression of gas atoms and molecules, as well as due to the excitation of rotational and vibronic states in the polyatomic molecules. The heat conductivity term describes the diffusive loss of kinetic energy between the propagating acoustic wave and the adjacent gas, or between the compressed and the expanded parts of an acoustic wave, tending to equalize the temperature differences inside the wave. A detailed mathematical description and derivation of the sound attenuation coefficient can be found e.g. in [21,22].

For the calculation of the gas density $\rho_{gas}(T,P)$ and the speed of sound $c_{sound}(T,P)$ for gases at moderate temperature and pressure, the following well-known analytical expressions for ideal gases can be used:

$$\rho_{gas}(T,P) = \frac{P \cdot M_{gas}}{R_{gas} \cdot T}, \tag{2.41}$$

$$c_{sound}(T,P) = \sqrt{\frac{c_{p\,gas}(T,P)}{c_{v\,gas}(T,P)} \cdot \frac{P}{\rho_{gas}(T,P)}}, \tag{2.42}$$

where P is the gas pressure, M_{gas} is the molar mass of the gas, R_{gas} = 8.3144598(48) J/K·mol is the universal gas constant, and T is the gas temperature in Kelvin.

In this form (Equations (2.36) – (2.42)), the model can be used with reasonable accuracy for most thermophonic applications in real gases. For more complex cases, such as thermal sound generation in gases near the condensation points or near the critical points, the model may require further modifications.

2.6 Determination of the sound-pressure amplitude generated by an any shaped thermophone

To describe accurately the sound pressure generated by a thermophone, the shape and the size of the thermophone surface have to be taken into account. If the wavelength of the generated acoustic waves is at the same order as the size of the thermophone or smaller, diffraction of elementary waves occurs and so-called acoustic near-field conditions must be considered (see Figure 2.7(c)).

Under these conditions, for a thermophone of arbitrary size and shape (e.g. a line, a rectangle, a circle, a sphere or a cylinder), the thermophone surface has to be discretized into a suitable number n of point sources. To obtain a prediction accuracy of at least 99.5%, each point source must be at least ten times smaller than the generated acoustic wavelength. The total input power $P_{el\ eff}$ has to be distributed over all these point sources corresponding to their surfaces.

Using a discretized version of the Kirchhoff-Helmholtz integral

$$\Delta p_{sound}(\bar{r}, f_{th}) = \left| \sum_{k=1}^{k=n} \Delta p_k(\bar{r}, f_{th}) \cdot \exp(\mathrm{i} \cdot 2 \cdot \pi \cdot f_{th} \cdot \frac{|\bar{r}_k|}{c_{sound}(T,P)}) \right|, \tag{2.43}$$

the complex amplitudes of all n point sources have to be superimposed at the observation point r (see Figure 2.7(b)). The absolute value of the superposition yields the sound pressure amplitude Δp_{sound} at the observation point. The discrete point-source approach allows to determine the sound-pressure amplitude for arbitrarily shaped thermophones in both the acoustic near and far fields.

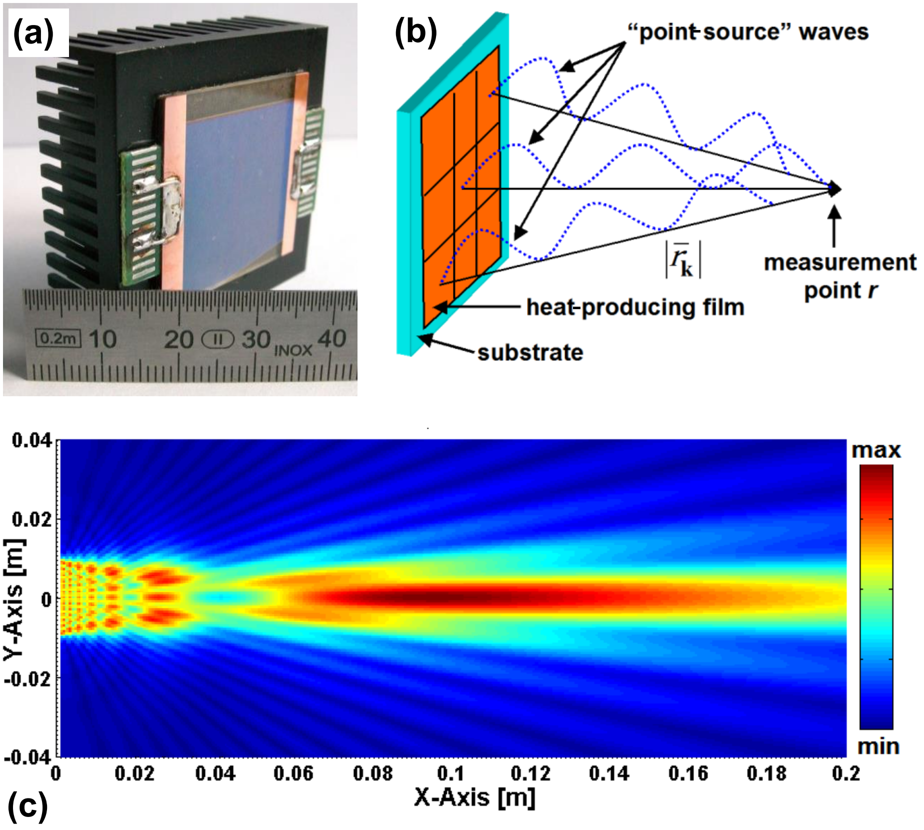

FIG. 2.7 (a) A 50-nm-thin, 20 × 20 mm^2 Indium-Tin-Oxide (ITO) coating on a quartz-glass substrate as a thermophone sample. **(b)** Schematic representation of the superposition of elementary waves.
(c) Distribution of the sound pressure generated in air (at normal temperature and pressure) in front of a 20 × 20 mm^2 thermophone during continuous sinusoidal excitation at 125 kHz, calculated from Equation (2.43). The frequency of the generated acoustic waves is 250 kHz. The thermophone is placed at X = 0 in the YZ-plane.

2.7 Summary and discussion

Based on the consideration of an acoustic wave as a thermally induced kinetic-Energy-Density-Function (EDF) and on its propagation in the adjacent gas, a mathematical description of thermophonic sound generation in real gases has been derived.

Using this energy-based concept the difficulties encountered with the analytical solution of a set of coupled partial differential equations for temperature and pressure are avoided, and a full analytical solution for the thermally generated sound pressure at each point of the surrounding real gas is obtained.

From the theoretical point of view, the proposed EDF model is generalized and can be applied to arbitrary thermal power sources including thermophones, plasma sources, laser beams, chemical and nuclear reactions. The non-linear effects such as shock waves and hypersonic waves, caused e.g. by explosions are not included and have to be treated separately.

Unlike the existing theoretical approaches [2,5,6,8-11,15-17] (see Section 1.2, Equations (1.1) - (1.8)) for modeling the thermophonic sound generation in gases, only the EDF model describes free-standing as well as substrate-based thermophones and takes into account

- the thermodynamic properties of thermophone materials, including the thermal inertia of the heat-producing film and the thermal effusivities of the substrate and the adjacent gas,
- the physical properties of the adjacent real-gas atoms and molecules,
- the distance- and frequency-dependent sound-attenuation effects,
- and the shape and size of the thermophone surface.

Thus, the EDF model is applicable to a wide range of thermophonic applications in real gases. For more complex cases, such as thermal sound generation in gases near their condensation points or near their critical points, the EDF model may require further modifications.

In order to better understand the EDF model, let us look more closely at Equation (2.38) which describes the sound pressure generated by a thermo-acoustic point source in a real gas.

The EDF model predicts the amplitude of sound pressure generated by a thermo-acoustic point source at an arbitrary observation distance r in a real gas at temperature T and pressure P:

$$\Delta p(T,P,f_{th},r) = \left[\frac{\Delta Q_{gas}(T,P,f_{th})}{V_{wave}(T,P,f_{th}) \cdot \left(1 - b \cdot \dfrac{\rho_{gas}(T,P)}{M_{gas}} \right)} \cdot \frac{3}{F_{DoFs}(T,P)} \right] \cdot \frac{r_0(T,P,f_{th})}{r} \cdot A(T,P,r,f_{th}),$$

where $\Delta Q_{gas}(T, P, f_{th})$ is the amount of thermal energy flowing into the gas, $V_{wave}(T, P, f_{th})$ is the volume of the generated acoustic wave, b is the gas-specific van-der-Waals constant which describes the volume occupied by the gas particles in a mol of a given gas, $\rho_{gas}(T,P)$ and M_{gas} are the density and the molar mass of the gas, $F_{DoFs}(T,P)$ is the total number of degrees of freedom for a given set of gas molecules at a given temperature and pressure, $r_0(T, P, f_{th})$ is the initial position of the acoustic wave, and the function $A(T,P,r,f_{th})$ describes the distance- and frequency-dependent decrease of the sound-pressure amplitude due to sound attenuation.

As can be seen from the above equation, the volume of the generated sound wave V_{wave}, the amount of thermal energy ΔQ_{gas} flowing into the gas, as well as the initial position r_0 of the generated acoustic wave depend, besides gas temperature T and pressure P, on the heating frequency $f_{th} = 1/t_{th}$. As discussed in Section 2.1, the heating frequency depends on the type of excitation. Hence, one has to distinguish between single-pulse excitation and continuous sinusoidal excitation when the thermophone reaches its thermodynamic equilibrium temperature. Figure 2.8 highlights the differences between these two excitation types.

As depicted in Figure 2.8, the volume of the generated acoustic wave V_{wave} depends on the speed c_{sound} of sound in the gas and on the thermal excitation frequency f_{th}. The amount of thermal energy ΔQ_{gas} flowing into the adjacent gas depends on the supplied electric power P_{eff} and on the heating frequency-dependent energy distribution function $E_{gas}(T,P,f_{th})$. This function describes the relative distribution of the released thermal energy between the heat-producing film, the adjacent gas and the substrate and is given by

$$E_{gas}(T,P,f_{th}) = \frac{e_{gas}(T,P)}{e_{gas}(T,P) + e_{sub}(T,P) + I_{film\ th}(T,P,f_{th})},$$

where

$$e_{gas}(P,T) = \sqrt{\lambda_{gas}(T,P)\cdot\rho_{gas}(T,P)\cdot c_{v\,gas}(T,P)} \text{ and } e_{sub}(T,P) = \sqrt{\lambda_{sub}(T,P)\cdot\rho_{sub}(T,P)\cdot c_{p\,sub}(T,P)}$$

are the temperature- and pressure-dependent thermal effusivities of gas and substrate,

and $I_{film\ th}(T,P,f_{th}) = d_{film}(T,P)\cdot\rho_{film}(T,P)\cdot c_{p\,film}(T,P)\cdot\sqrt{2\cdot\pi\cdot f_{th}}$ is the frequency-dependent thermal inertia of the electrically conductive film, where d_{film} is the thickness of the film and ρ_{film} und $c_{p\,film}$ are its density and specific heat capacity, respectively.

It is obvious that the energy distribution function $E_{gas}(T,P,f_{th})$ and thus the EDF model apply also for free-standing films and wires with $e_{sub} = e_{gas}$.

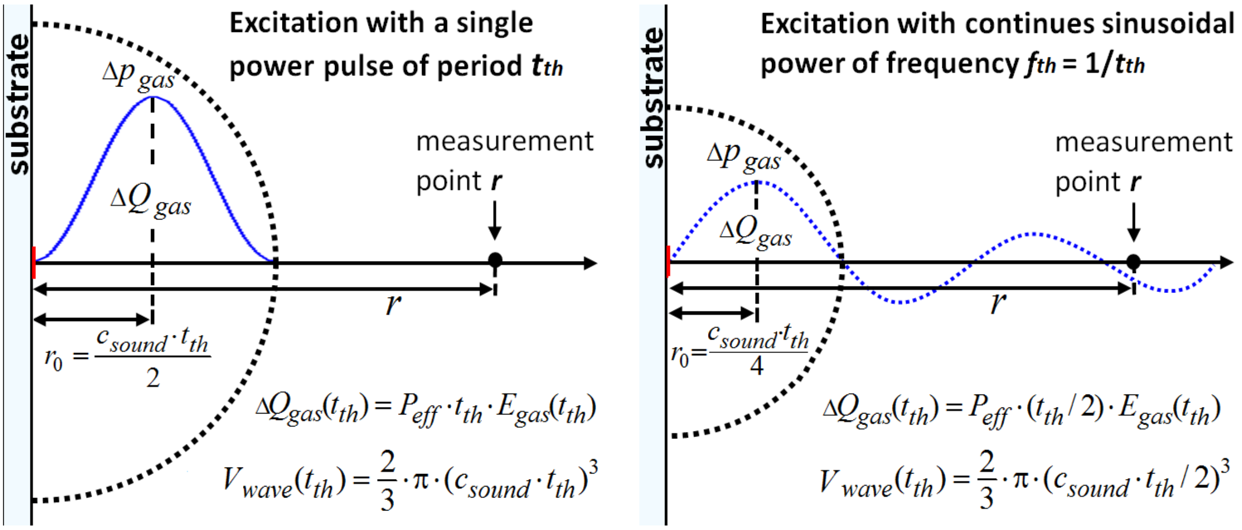

FIG. 2.8 Differences between single-pulse excitation and continuous sinusoidal excitation.

Furthermore, the EDF model could also be applied to plasma loudspeakers if the plasma discharge is considered as an electrically heated conductor with thickness d, density ρ and heat capacity c_v.

In addition, it can be assumed that the EDF model can also be applied to the photo-acoustic effect in gases by considering the light-absorbing layer as a heated film of thickness d, density ρ and heat capacity c_v and with a corresponding thermal inertia $I_{th\,film}(f_{th})$.

For a better understanding of the dependencies of the EDF model on individual parameters let us insert the equations for ΔQ_{gas}, V_{wave} and r_0 in to the Equation (2.38). After a few trivial algebraic calculation steps, one obtains for the sound-pressure amplitude generated by a thermo-acoustic point source excited with a continuous sinusoidal electric power of effective value $P_{el\ eff}$ and frequency f_{th}:

$$p(\bar{r}, f_{th}) = \frac{3 \cdot P_{el\,eff} \cdot f_{th}}{2 \cdot \pi \cdot c_{sound}^2 \cdot \left(1 - b \cdot \dfrac{\rho_{gas}}{M_{gas}}\right) \cdot |\bar{r}|} \cdot \frac{3}{F_{DoFs}} \cdot \frac{e_{gas}}{e_{gas} + e_{sub} + d_{film} \cdot \rho_{film} \cdot c_{p\,film} \cdot \sqrt{2 \cdot \pi \cdot f_{th}}}$$
$$\cdot \exp\left(|\bar{r}| \cdot \left[-\frac{(2 \cdot \pi \cdot f_{th})^2}{2 \cdot \rho_{gas} \cdot c_{sound}^3} \cdot \left(\frac{4}{3}\mu_{dyn} + \mu_{bulk} + \left(\frac{\lambda_{gas}}{c_{v\,gas}} - \frac{\lambda_{gas}}{c_{p\,gas}}\right)\right)\right]\right). \tag{2.44}$$

Thus, the main parameters affecting the efficiency of thermophonic sound generation are: the speed of sound in the gas, the input power and the excitation frequency, the ratio of the thermal effusivities of substrate and adjacent gas, the heat capacity of the electrically conductive film, the frequency- and distance-dependent sound attenuation in the gas and the number of degrees of freedom of the adjacent gas molecules.

The thermal-power dependence means that the higher the amplitude of the supplied input power, the higher the temperature increase of the heat-producing film. In turn, this results in an increase of outward heat flux $\dot{Q}(t) = P_{el}(t)$ and an increase of the amount of thermal energy flowing into the gas.

The dependence of the generated sound pressure on the thermal excitation frequency means that the higher the frequency of the oscillating thermal input power, the smaller is the volume of the generated acoustic wave.

A higher thermal energy and a smaller volume both result in an increased pressure amplitude. Thus, the EDF model explains the experimental findings of previous researchers reporting an increase of the generated sound pressure with an increase of the excitation frequency.

However, the initial increase of the generated sound pressure with an increase of the excitation frequency f_{th} will be suppressed by the frequency-dependent thermal inertia of the heat-producing film $I_{th\,film}$ and by the exponential increase of sound attenuation in the gas. Furthermore, the EDF model shows that for large $C_{film} = d_{film} \cdot \rho_{film} \cdot c_{p\,film}$ and for high excitation frequency f_{th}, the square-root term in the energy distribution function $E_{gas}(T,P,f_{th})$ leads to a significant deviation from linearity towards the square-root dependence predicted by Arnold and Crandall [2] for free-standing thermophones.

Thus, the EDF model explains the experimental findings of all previous research indicating that the generated sound pressure $p(f)$ is proportional to $f - f^{0.5}$.

Additionally, the EDF model confirms the statement of Arnold and Crandall [2] that the conductor has to be very thin and its heat capacity C_{film} has to be small. It also confirms the HCPUA theory of Xiao *et al.* [8] that an efficient free-standing thermophone requires a small heat capacity per unit area.

Moreover, the EDF model confirms the findings of Shinoda [5], Boullosa [6], Tian *et al.* [11] and Hu *et al.* [16] on substrate-based thermophones, and in particular their recommendation to use substrates with a small thermal effusivity e_{sub}.

Consequently, it is no surprise that a high-frequency plasma combustion, which does not require solid conductor films and substrates at all, should have the highest thermo-acoustic efficiency. This explains, for example, why the thunder induced by lightning is so powerful.

A detailed discussion about the efficiency of the thermo-acoustic sound generation with thermophones can be found in one of the author's previous publication [23].

3. Experimental validation of the EDF model

For experimental validation of the EDF model, several thermophone samples of different sizes, shapes and materials were tested for sound generation in gases in a frequency range up to 1 MHz. Thus, the experimentally investigated frequency range is around 10 – 20 times wider than in all the experimental studies on thermophones made so far. The sample pool includes free-standing carbon-nano-wire webs (CNW) of different thickness (5 – 150 µm), size and shape and substrate-based thermophones of different size and shape consisting of Titanium and Indium-Tin-Oxide (ITO) coatings of different thickness (20 – 2500 nm) on polycarbonate and quartz-glass substrates. Altogether, more than fifty different thermophone samples were tested for sound generation. Figure 3.1 shows some tested thermophone samples.

The free-standing CNW samples were produced and characterized by Bundesanstalt für Materialforschung und -prüfung (BAM), department 6.2. The substrate-based samples were produced and characterized with respect to their composition and the thickness of their coatings, by BAM, department 6.7. The thickness of the coatings was determined by means of X-ray fluorescence with an accuracy of ± 3 %.

In order to carry out the characterization of thermophones in a wide frequency range, a wide-band and resonance-free ultrasound receiver with known transfer functions is required. One common method to measure the sound pressure is the use of calibrated condenser microphones.

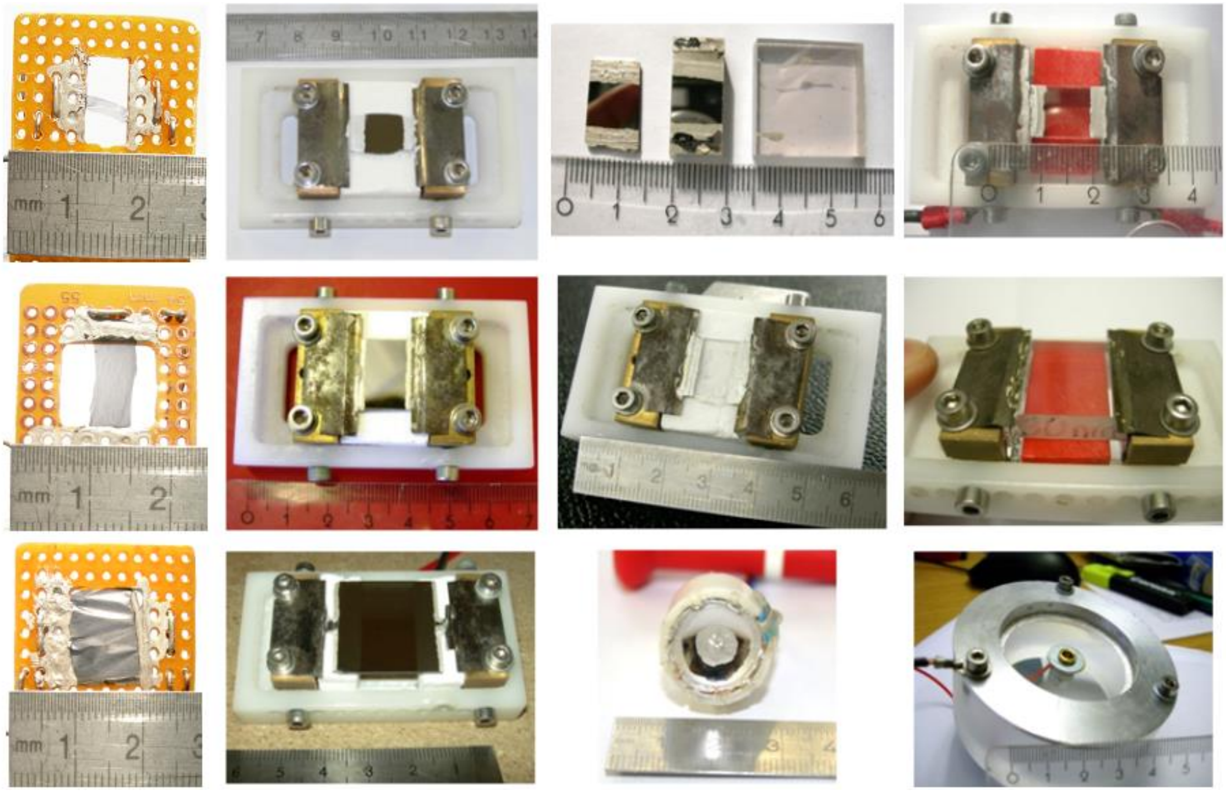

FIG. 3.1 Photographs of several thermophone samples consisting of: free-standing carbon-nano-wire webs (left), and Titanium and Indium-Tin-Oxide coatings on quartz-glass and polycarbonate substrates mounted in the sample holder.

To date, the best commercially available condenser microphones (for example, the 1/8” B&K microphone) are calibrated in the frequency range up to 140 kHz and are not suitable for frequencies higher than 150 kHz. Moreover, these microphones are originally calibrated for air at room temperature and normal atmospheric pressure. As already mentioned in Section 1.3, the use of these microphones at other temperatures and air pressures or in other gases, with different density ρ and speed of sound c, changes the stiffness $S = \rho \cdot c^2 \cdot A/d$ of the gas-filled microphone capsule (where A is the surface of the capsule and d is the capsule height) [19]. As also discussed in [19], the change of the capsule stiffness results in a change of the sensitivity and the resonance frequencies of the microphone, which leads (in extreme cases) to the discrepancies between the measured and the real sound pressures on the order of up to few hundred percent. Hence, for measurements of sound pressures in different gases and in a frequency range e.g. from 1 kHz to 1 MHz and beyond, a special microphone is required in order to obtain reliable results.

Another method to determine the sound pressure of an incident acoustic wave is the measurement of the displacement of an object with known mass placed in the sound field. For the detection of the displacement of the object, an interferometer or a laser vibrometer can be used. The detection bandwidth corresponds to the bandwidth of the measurement system that is employed and can cover a frequency range up to a few tens of MHz. Thus, in most cases, the full range of the ultrasound applications can be covered with one single measurement device. Hence, a Laser-Doppler-vibrometer combined with a 12-µm-thin polyethylene film placed in the sound field are used as a broadband and resonance-free “microphone” for the measurement of the particle velocity and the sound pressure generated by the respective thermophones in several gases.

3.1 Broadband measurement of the particle velocity and the sound pressure by means of a Laser-Doppler-Vibrometer

The use of laser interferometers as “microphones” is known since the middle of the last century when the first manageable IR-laser-interferometers were built and applied to measure the vibrations of objects in a sound field. A review of membrane vibration experiments can be found e.g. in the review by C. Jenkins and U.A. Korde [24].

The application of a Laser-Doppler-vibrometer for measuring the particle velocity in air with an ultra-light membrane was described and tested in the audible-frequency range by Leclère and Laulagnet [25]. Essentially, the measurement is based on the temporal detection of the spatial displacement of a film with known mass per unit area in a sound field.

In general, as has been shown experimentally in one of the author’s recent publications [26], this method allows for a resonance-free measurement of the particle velocity and the sound pressure in all optically transparent fluids with known density and speed of sound. The bandwidth of the detection corresponds to the bandwidth of the respective laser-vibrometer system. Thus, the transfer functions of arbitrary sound and ultrasound transducers in different media and at different temperatures and pressures can be clearly characterized.

The advantages of this measurement in comparison to conventional sound-pressure receivers such as condenser microphones or piezo-electric transducers are:

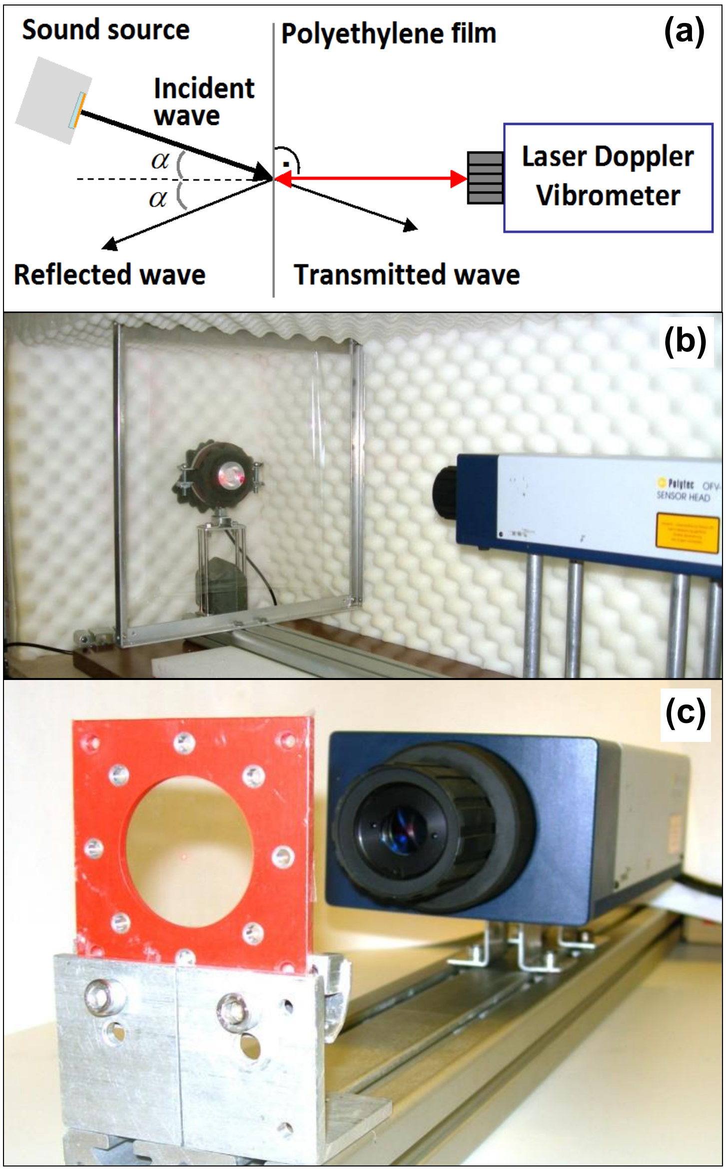

FIG. 3.2 **(a)** Schematic setup for the measurement of the particle velocity by means of a single-point laser Doppler vibrometer and a polyethylene film as detector. Photographs **(b)** and **(c)** show possible implementations of the experimental setup.

- no calibration required;
- a large dynamic measuring range (from µPA to MPa) and a large bandwidth (from few Hz to few MHz);
- suitability for precise measurements in any laser-light-transparent medium;
- a resonance-free frequency response.

Hence, in all further experiments, a Laser-Doppler-vibrometer combined with a 12-µm-thin polyethylene film with a mass of 0.01264 ± $2 \cdot 10^{-5}$ kg/m^2 is used as a broadband particle-velocity detector. Figure 3.2(a) schematically shows the measuring principle in which a single-point Laser-Doppler-vibrometer is combined with a polyethylene film as a particle velocity detector. Figures 3.2(b,c) show possible implementations of the measurement setup. The acoustic wave generated by a sound source moves the polyethylene film and the laser vibrometer detects the displacement and the velocity amplitude of the film. Knowing the angle α of incidence, the mass of the film per unit area $M_{foil} = \rho_{foil} \cdot d_{foil}$, where ρ_{foil} and d_{foil} are the density and the thickness of the film respectively, and the temperature- and pressure-dependent acoustic impedance of the adjacent gas $Z_{gas}(T,P)=\rho_{gas}(T,P)\cdot c_{sound}(T,P)$, the amplitude of the particle velocity of the incident acoustic wave of frequency f can be calculated from the detected velocity amplitude of the film $v_{foil}(f)$ as follows:

$$v_{sound}(T,P,f)=v_{foil}(f)\cdot\sqrt{\frac{1}{\cos^2\alpha}+\left(\frac{\pi\cdot M_{foil}\cdot f}{Z_{gas}(T,P)}\right)^2}\ . \tag{3.1}$$

Multiplying the amplitude of the particle velocity $v_{sound}(T, P, f)$ by the acoustic impedance of the surrounding gas yields the sound-pressure amplitude of the incident acoustic wave at the measurement point

$$p_{sound}(T,P,f)=\rho_{gas}(T,P)\cdot c_{sound}(T,P)\cdot v_{sound}(T,P,f). \tag{3.2}$$

The corresponding sound-pressure level L_{sound} in air is defined as

$$L_{sound}(T,P,f)=20\cdot\log(p_{sound}(T,P,f)/p_0)\ \text{with}\ p_0=20\ \mu\text{Pa}. \tag{3.3}$$

Formula (3.1) is based on the solution of the membrane equation proposed by Leclère and Laulagnet [25] for perpendicularly impinging acoustic waves, and is modified for obliquely incident waves. The reason for this modification are the standing waves between the sound source and the film, and interferences that occur if the angle α of incidence is equal to zero. In order to minimize such interferences, a sound source should be placed in such a way that no standing waves can occur between the source and the film (see Figure 3.2(a)).

Note that the thickness of the sensing film has to be several times smaller (for example ≤ 1/10) than the wavelength of the acoustic wave which is excited in the film by the incident acoustic wave. From this condition, a cutoff frequency of approximately 15 MHz results when a 12-µm-thick polyethylene film in air is used as the sound-pressure detector.

Additionally, a couple of practical points should be considered when using a laser-vibrometer in combination with a sensing film as sound-pressure detector:

- The sensing film should be positioned perpendicular to the laser beam.
- In order to minimize the interferences of standing waves between the sound source and the sensing polyethylene film, the sound source should be placed obliquely to the film (see Figure 3.2).
- For measurements of sound pressures in the µPa and mPa range, it is advisable to use a film with the smallest possible mass per unit area to obtain larger displacement and velocity amplitudes.
- The detected amplitudes have to be averaged, especially for measurements at frequencies in the MHz range.
- For measurements in the µPA and lower mPa range, the experiment should be performed in a closed anechoic room or box (see Figure 3.2(b)) in order to cancel the acoustic noise from the outside. Sound pressures in the upper mPa, Pa and kPa range can be measured in free air.

All these preconditions enhance the signal-to-noise ratio and thus improve the accuracy of the detection.

3.2 Experimental examination of free-standing and substrate-based thermophones in air

For experimental validation of the EDF model several free-standing and substrate-based thermophone samples of different sizes, shapes and materials were tested for sound generation in air at room temperature and pressure in a frequency range up to 900 kHz. All samples were excited using continuous sinusoidal excitation of a constant amplitude and without offset. The examination frequency range was limited to 900 kHz due to increasing noise of the measurement system.

As free-standing thermophones, samples consisting of carbon-nano-wire web (CNW) of different thicknesses and sizes were used. Figure 3.3(a) exemplarily shows a photograph of a $5 \times 12\ \mathrm{mm}^2$ CNW sample mounted on a plastic frame, and figure 3.3(b) shows an electron-microscope image of the CNW. The carbon-nano-wires have a mean diameter of about 200 nm. CNW samples were produced and characterized by BAM, department 6.2. The relative proportion of carbon and air is about 1/100. Hence, for EDF model-predictions the CNW samples are considered as electrically conductive films of 5, 15 and 50 µm thickness with an effective density of $\rho_{\mathrm{CNW+AIR}}$ = (1/100)·2200 [kg/m^3] + (99/100)·1.2 [kg/m^3] = 23.2 [kg/m^3], and an effective heat capacity of $c_{v\ \mathrm{CNW+AIR}}$ = (1/100) · 730[J/kg·K] + (99/100) · 716[J/kg·K] = 716.3 [J/kg·K]. The CNW samples were contacted electrically and fixed on plastic frames with electrically conductive silver paint (BUSCH 5900).

For substrate-based thermophones, quartz-glass and polycarbonate were used as substrates. The main reason to use quartz-glass and polycarbonate as substrates is that the density, heat conductivity and thermal capacity of these materials are well known. Additionally, the substrates have a smooth surface with a roughness smaller than 2 nm. Thus, the Titanium and Indium-Tin-Oxide (ITO) coatings can be assumed to be homogeneous.

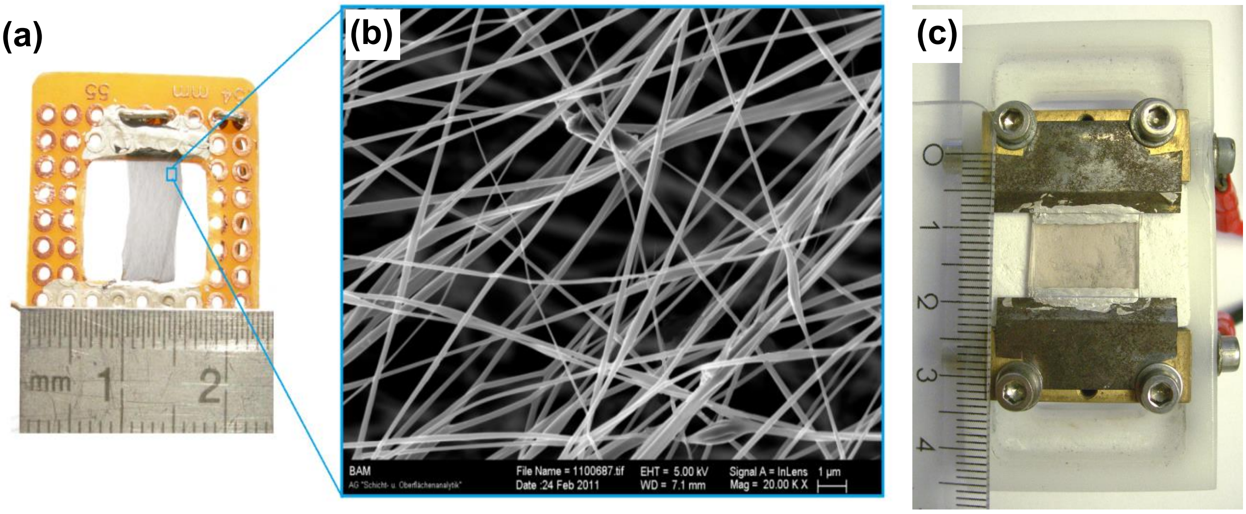

FIG.3.3 (a) Photograph of a 15-µm-thin free-standing CNW sample. **(b)** Electron-microscope image of the carbon-nano-wire web (CNW) made by BAM, department 6.7. **(c)** Photograph of a substrate-based thermophone sample consisting of an ITO coating on quartz-glass mounted in the sample holder.

The substrate-based thermophone samples were placed in a holder and contacted with small spring contacts (see Figure 3.3(c)). Two narrow stripes of electrically conductive silver paint on two rims of the electrically conductive film ensure a uniform electric contact and thus a uniform current density in the electrically conductive film, leading to a homogeneous heating of the film.

Figure 3.4 schematically shows the experimental setup with the essential equipment, and Table 3.1 summarizes the sample properties, and the excitation-power and measurement parameters for seven of the tested thermophone samples.

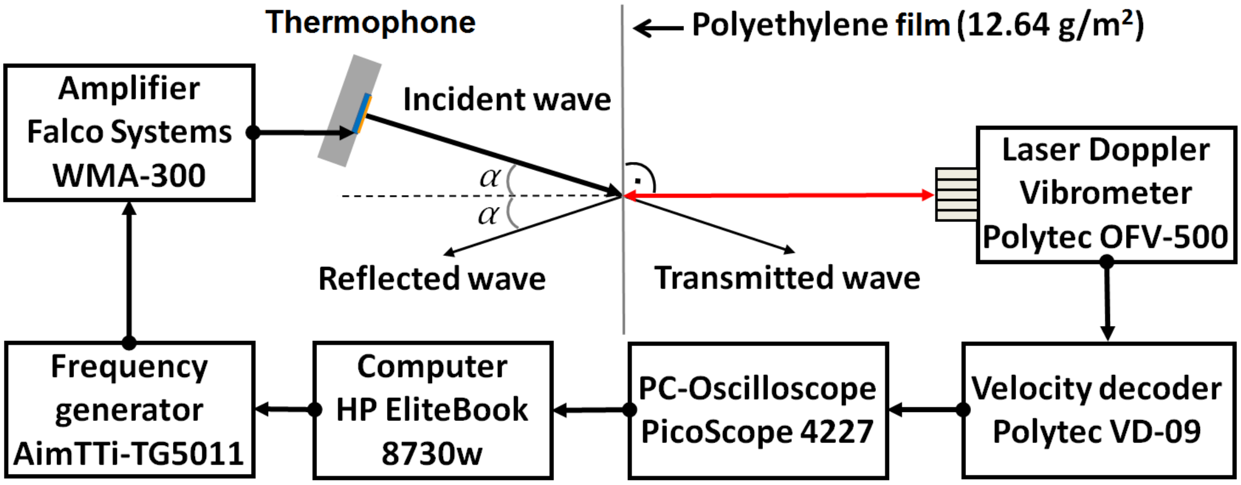

FIG. 3.4 Schematic experimental setup.

TABLE 3.1 Sample properties, and excitation and measurement parameters.

Sample	(a)	(b)	(c)	(d)	(e)	(f)	(g)
Size [mm]	2 × 5.5	5 × 12	10 × 10	4.5 × 5	10 × 15	22 × 24	15 × 20
Substrate material	No substrate, free-standing	No substrate, free-standing	No substrate, free-standing	Quartz-glass	Quartz-glass	Quartz-glass	Polycarbonate
Film material	Carbon-nano-wire – air	Carbon-nano-wire – air	Carbon-nano-wire – air	Titanium	Indium-Tin-Oxide (90/10)	Titanium	Indium-Tin-Oxide (90/10)
Film thickness d_{film} [nm]	5000 ± 500	15000 ± 500	50000 ± 500	30 ± 2	300 ± 10	20 ± 2	30 ± 2
Suplied electric power $P_{el\ eff}$ [W]	0.06 ± 0.005	0.175 ± 0.005	0.175 ± 0.005	2.32 ± 0.05	2 ± 0.05	4.5 ± 0.05	1 ± 0.05
Voltage U [V]	20 ± 0.1	24 ± 0.1	5.7 ± 0.1	25 ± 0.1	13.5 ± 0.1	27 ± 0.1	14.8 ± 0.1
Current I [mA]	6 ± 0.05	14.5 ± 0.05	62 ± 0.5	185 ± 5	300 ± 5	335 ± 5	135 ± 5
Distance sample - measurement point [mm]	30 ± 1	30 ± 1	30 ± 1	20 ± 1	70 ± 1	45 ± 1	45 ± 1
Incident angle α [°]	0	0	0	0	0	30 ± 1	25 ± 1

The electrical resistances of the tested thermophone samples depend on the respective electrically conductive materials, their thickness and temperature. Hence, to determine the supplied electric power $P_{el}(t)$, the amplitudes of the voltage drop $U(t)$ and of the electric current $I(t)$ were measured for each sample separately using a Tektronix TDS2024 oscilloscope. To determine the amplitude of the electric current $I(t)$, the voltage drop on a commercially available 0.1 Ω ± 1 % shunt resistor was observed.

The measurement procedure for the generated sound pressure is automated (see Figure 3.4, schematic experimental setup). The computer controls the frequency generator and sets the excitation frequency in pre-set increments. At each frequency step, the velocity amplitude of the sensing polyethylene film detected by the laser-vibrometer is averaged and stored. In the following step, the respective sound-pressure amplitude is calculated by means of Equation (3.2) and stored. Thereafter, the computer sets the next excitation frequency, and the procedure is repeated.

Figure 3.5 compares the EDF model-predicted and the measured sound-pressure levels with respect to the thermal excitation frequency f_{th} for three different free-standing thermophone samples (Samples (a),(b),(c) as listed in Table 3.1).

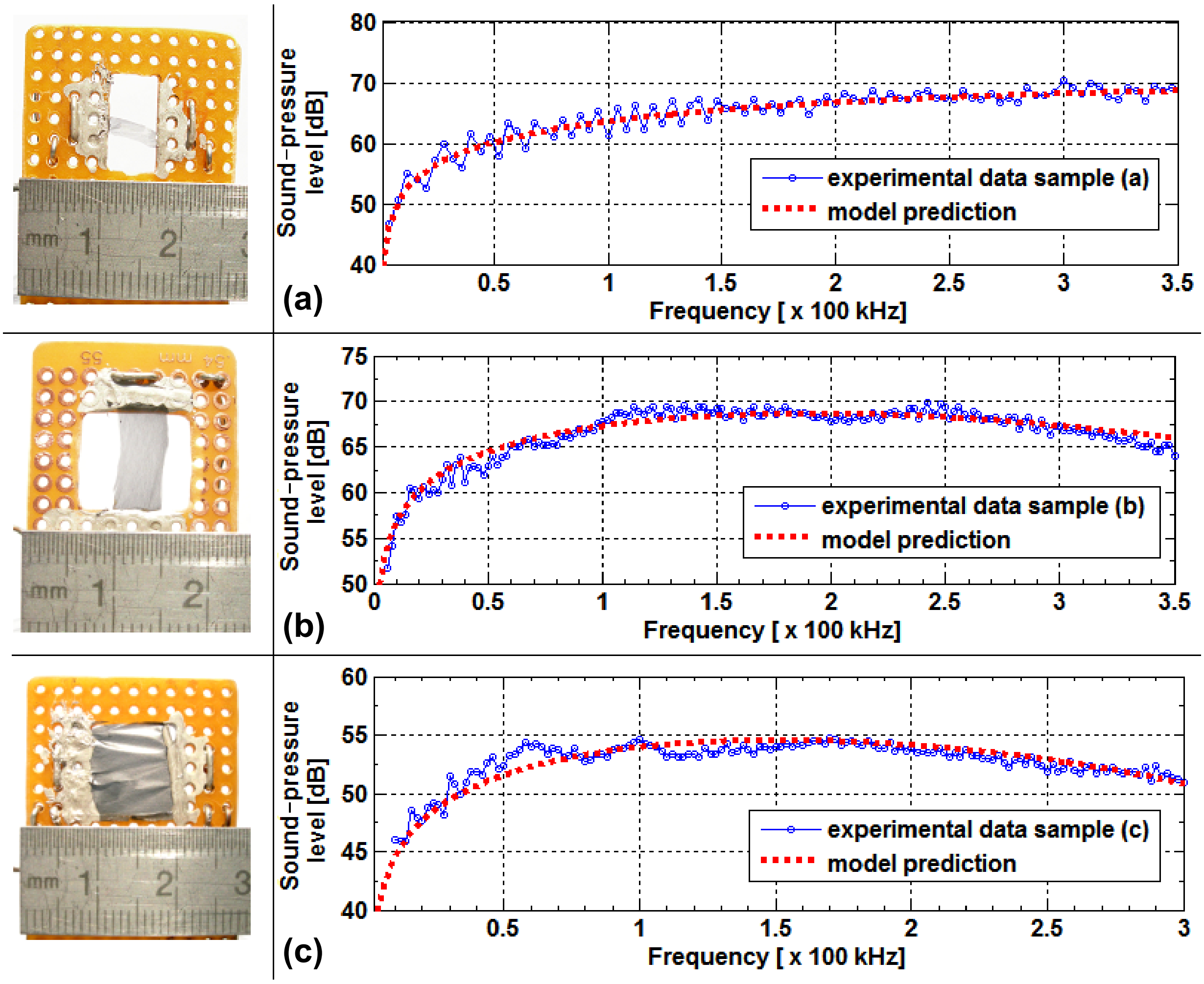

FIG. 3.5 Comparison of measured and EDF model-predicted (dotted line) sound pressure levels with respect to the operating frequency for free-hanging thermophone samples (Samples (a),(b),(c)). Sample properties, and excitation and measurement parameters are listed in Table 3.1.

The frequency range for free-standing samples is limited to 350 kHz due to the increase of the noise level of the measurement system. Excitation of these samples with higher electrical power generates higher sound pressure-levels but overheating of CNW leads to destructions out of the samples.

Comparison of measured and EDF model-predicted sound pressure levels for free-standing samples shows deviations of at most 1.5 to 2 dB. The reasons for these relatively large deviations for free-standing thermophone samples are the inhomogeneities of the CNW samples and rather approximate values for the sample thickness, density and heat capacity. The small periodic oscillations of the sound-pressure levels can be assigned to standing acoustic waves between the samples and the sensing polyethylene film.

The results for free-standing samples demonstrate the influence of the CNW thickness and the corresponding thermal capacity on the generated sound pressure. Consider for example the sound-pressure levels generated by these samples at 150 – 200 kHz: the sample (a), with 5-µm thickness, generates about 67 dB sound-pressure level, consuming 0.06 Watts of electric power; the 15-µm-thick sample (b) reaches similar sound-pressure levels, but consumes 0.175 Watts of electric power; and the 50-µm-thick sample (c) reaches only 55 dB sound-pressure level at the same 0.175-Watt excitation power.

The decrease of generated sound-pressure levels for frequencies above 180 kHz for sample (b) and for frequencies above 150 kHz for sample (c), results from the passing of the acoustic near-field beam relative to the observation point with the increase of the operation frequency (as an example for movement of acoustic near-field with increase of excitation frequency consider Figure 3.7(b - c)).

Additionally, the results for free-standing CNW samples clearly dismiss the assumption of Arnold and Crandall [2] and Xiao et *al.* [8,9] about an expanding and contracting air layer and an imaginary gas piston which generates the acoustic waves. The measured sound pressures show that the air inside the CNW stores the supplied thermal energy and does not contribute to the excited sound pressure. Moreover, the air inside the CNW acts as an additional thermal capacity of the heat-producing carbon-nano-wires leading to a reduction of the generated sound pressure. However, the tested free-standing CNW samples showed a better acoustic efficiency compared to the substrate-based thermophone samples due to the absence of a substrate and hence due to a larger heat flux into the adjacent air. Unfortunately, free-standing CNW samples are mechanically and thermally unstable. The CNW samples burn out in air at excitation powers of a few Watts, when the CNW reaches temperatures of about 450 - 500°C. Additionally, as the experimental experience showed, free-standing CNW samples are very fragile and can tear already at a moderate airflow.

Now let us consider the experimental results of substrate-based thermophone samples. Figure 3.6 shows a comparison of measured and EDF model-predicted sound-pressure levels for four of the tested substrate-based thermophone samples (listed in Table 3.1 as samples (d,e,f,g)) consisting of Titanium and Indium-Tin-Oxide coatings of different size and thickness on polycarbonate und quartz-glass substrates. The frequency-dependent noise level of the measurement system is also plotted as dashed lines in the diagrams.

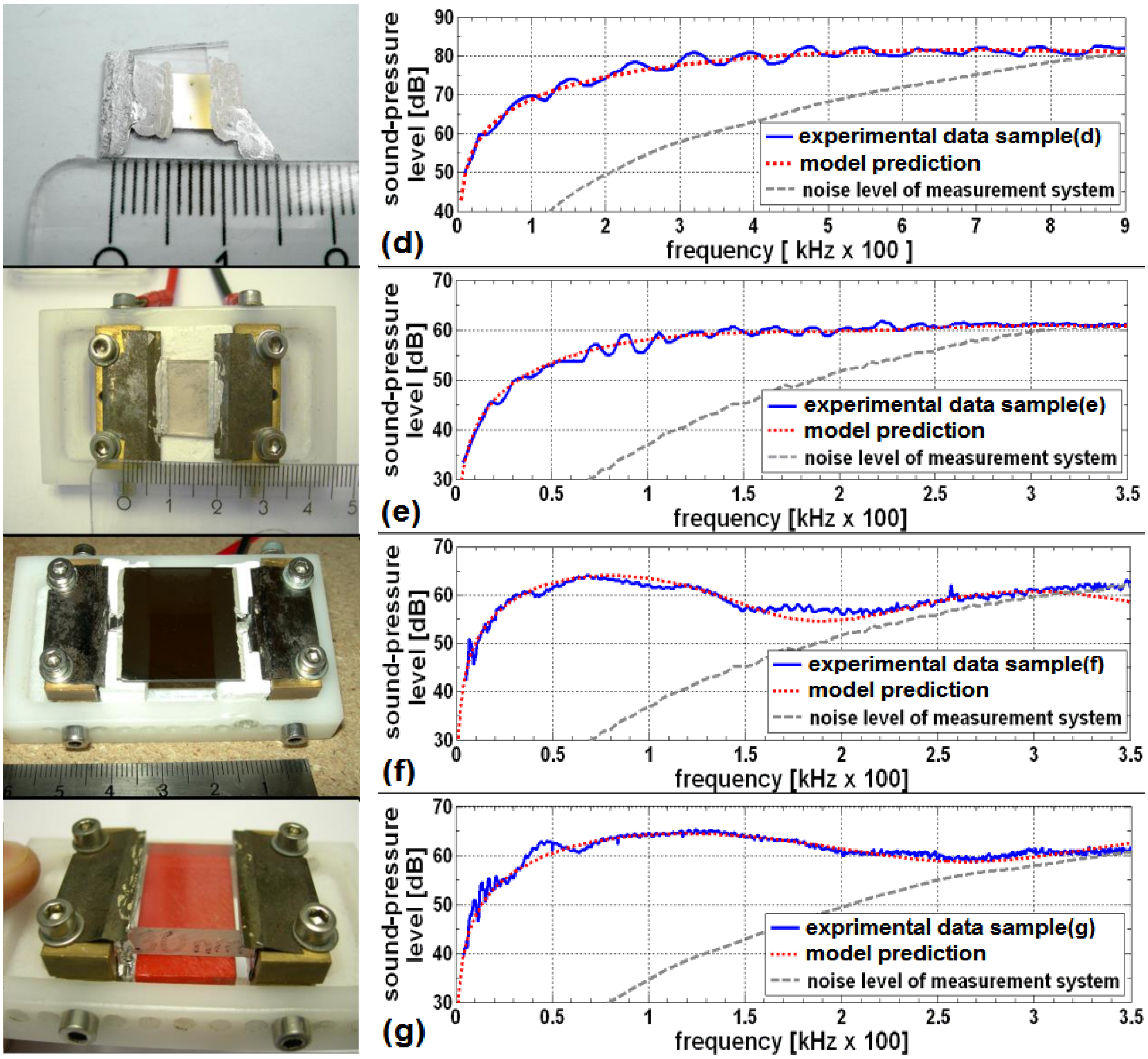

FIG. 3.6 Comparison of measured (solid lines) and EDF-model-predicted (dotted lines) sound pressure levels with respect to operating frequency for Samples (d – g) (samples properties, excitation, and measurement parameters are listed in Table 3.1. Dashed line represents experimentally detected noise level of the measurement system.

Comparison of measured and EDF model-predicted sound-pressure levels shows for all tested substrate-based thermophones a deviation of at most 1 – 1.5 dB. The slight periodic oscillations with a maximum amplitude of about 2 – 3 dB, that are observed in Figure 3.6(d,e) can be assigned to standing waves between the sample and the sensing polyethylene film, caused by the perpendicular alignment of the thermophone direction and the sensing polyethylene film (incident angle $\alpha = 0$). This effect was diminished by increasing the angle α of incidence, as can be seen in Figure 3.6(f,g).

Figure 3.6(d) shows the experimentally detected sound-pressure level in the frequency range from 4 to 900 kHz for a 4.5 × 5 mm^2 thermophone consisting of a 30-nm-thin Titanium coating on quartz-glass substrate. The influence of the thermal inertia of the 30-nm-thin Titanium coating is very small in this frequency range, due to the dominance of the thermal effusivity of the quartz-glass substrate ($e_{quartz\ glass} \approx 1500$ [$(\text{W}^2\cdot\text{s/m}^4\cdot\text{K})^{0.5}$]) on the energy distribution function $E_{gas}(T,P,f_{th})$

(see Equation (2.21)) compared to the effusivity of air ($e_{air} \approx 4.7$ [(W^2·s/m^4·K)$^{0.5}$]) and the frequency-dependent thermal inertia of the heat-generating film (for a 30-nm-thin Titanium film we obtain at 500 kHz thermal excitation frequency $I_{film}(f_{th}) \approx 127$ [(W^2·s/m^4·K)$^{0.5}$] and at 1 MHz $I_{film}(f_{th}) \approx 180$[(W^2·s/m^4·K)$^{0.5}$]) (see Equation (2.22)). Hence, for frequencies up to 600 kHz, the influence of the thermal inertia of the 30-nm-thin Titanium film is smaller than 1 dB. At 900 kHz, its effect amounts to at least 1.5 – 2 dB.

However, at high frequencies, the sound attenuation in air has a major effect. For example, the sound attenuation of dry air at room temperature and normal atmospheric pressure is on the order of about 10 dB/m at 100 kHz and on the order of 480 dB/m at 1 MHz (calculated by means of Equations (2.39 – 2.40)). That is the reason why the examination distance for sample (d) was set at 20 mm.

Additionally, in the high-frequency range, the acoustic near-field effect has to be taken into account. Figure 3.7(a) exemplarily shows the sound field generated by a 4.5 × 5 mm^2 thermophone at 750 kHz operation frequency as calculated by use of the EDF model.

The influence of the thermal effusivity of different substrates can be observed from the results of sample (f) and sample (g) which have a similar size, but different substrate materials. The thermophone on the polycarbonate substrate (sample (g)) generated comparable sound-pressure levels to the thermophone on quartz-glass (sample (f)), but consumed only a quarter of the electric power due to a 3.5 times smaller thermal effusivity of the polycarbonate substrate compared to the quartz-glass substrate.

The slight deviations from the calculated sound-pressure levels for the 22 × 24 mm^2 thermophone sample (f) resulted from the inexact positioning of the sample relative to the measuring point on the polyethylene film. As Figures 3.7(b,c,d) show, the sound fields generated by this thermophone at high frequencies are very complex. Small variations in the positioning (± 1 mm) of this relatively large thermophone (22 × 24 mm^2), especially during measurements in the near-field (see Figures 3.7(c,d)), can lead to significant deviations from the expected sound pressures.

The near-field effect can be observed in Figure 3.6(f) (at 200 kHz) and Figure 3.6(g) (at 260 kHz) as a decrease of the sound-pressure level and as an increase at 300 kHz. The reason for this behavior is the passing of the generated sound beam relative to the observation point on the sensing polyethylene film with increase of the excitation frequency. The movement of the sound-beam maxima across the measuring point, can be seen in Figures 3.7(b,c,d), which show the sound-pressure distribution in air including the near-field as calculated from the EDF model for the 22 × 24 mm^2 thermophone (sample (f)) on a quartz-glass substrate under continuous sinusoidal excitation without offset at 70 kHz, 200 kHz and 300 kHz, respectively. The dashed line and the white point mark the positions of the sensing polyethylene film and of the sensing point of the laser-vibrometer, respectively.

Concluding remarks:

In order to carry out the characterization of thermophones in a frequency range up to 1 MHz and beyond, the samples have to be placed at a distance of a few cm from the measuring point. Additionally, to reduce the near-field effect, the thermophone sample has to be as small as possible. For these reasons, the size of the thermophone samples is reduced to 5 × 5 mm^2 and 3 × 3.5 mm^2 in further experiments and the distance to the observation point is set at 20 mm.

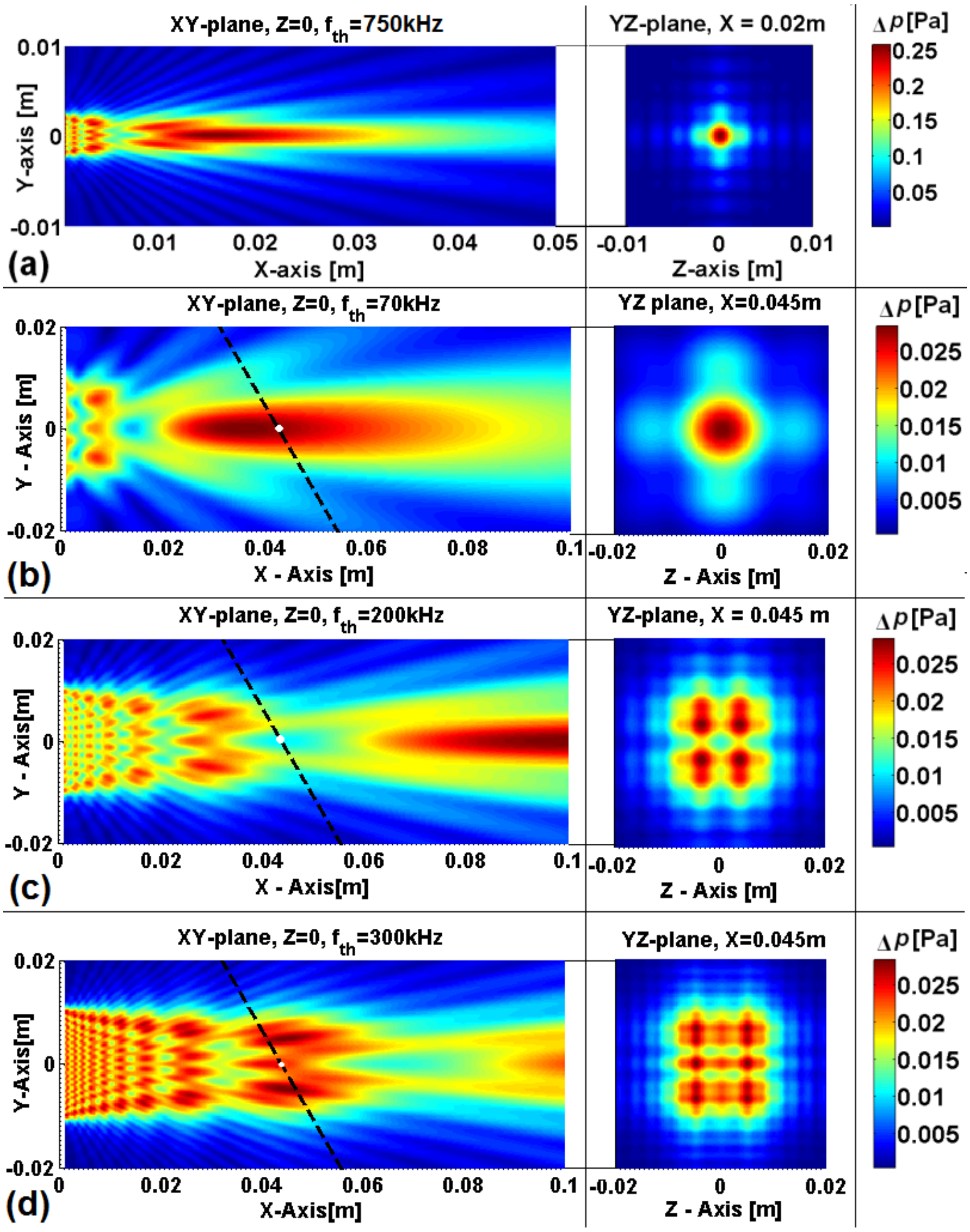

FIG. 3.7 Sound-pressure distributions in the XY- and YZ-planes calculated by means of Equation (2.43) for thermophones placed at zero in the YZ-plane: **(a)** 4.5 × 5 mm^2 sample (d) at 2.3 ± 0.05 W$_{eff}$ sinusoidal excitation without offset, at the operation frequency of 750 kHz; and **(b),(c),(d)** 22 × 24 mm^2 thermophone (sample (f)) on a quartz-glass substrate at 4.5 ± 0.05 W$_{eff}$ sinusoidal excitation without offset and at a frequency of 70, 200 and 300 kHz, respectively. The dashed line and the white point mark positions of the sensing polyethylene film and the sensing point of the laser-vibrometer respectively.

3.3 Experimental examination of the influence of the thermal inertia of the heat-producing film for substrate-based thermophones

Now let us validate one of the theoretical predictions from the EDF model and experimentally investigate the influence of the thermal inertia of an electrically conductive film on the sound pressure generated by substrate-based thermophones. In this context, the variation of only the film thickness, at constant sample size, measuring distance and excitation power, is a suitable method to experimentally verify the impact of the thermal inertia on the generated sound pressure. Therefore, five thermophone samples of equal surface area were prepared consisting of ITO ($In_2O_3/SnO_{2,}$ 90/10) coatings of various thicknesses (as electrically conductive films) on Herasil2-glass (quartz-glass) [27] substrates. The ITO coatings had thicknesses of 65, 206, 370, 1060 and 1440 nm. The samples were produced via a plasma coating process. Thereafter, the samples were annealed for one hour at 200°C in O_2. Finally, the ITO-layer thicknesses were determined by means of X-ray fluorescence with an accuracy of ± 3 %. The thermophone samples were placed successively into a holder and contacted with small spring contacts. Figure 3.8(a) shows one of the tested thermophone samples mounted in the holder. Two narrow stripes of electrically conductive silver paint (BUSCH 5900) on two rims of the ITO film ensure a uniform electric contact and thus a uniform current density in the conductive film, leading to homogeneous heating of the film. The final size of the “active” thermophone surface was set at 5 × 5 mm^2.

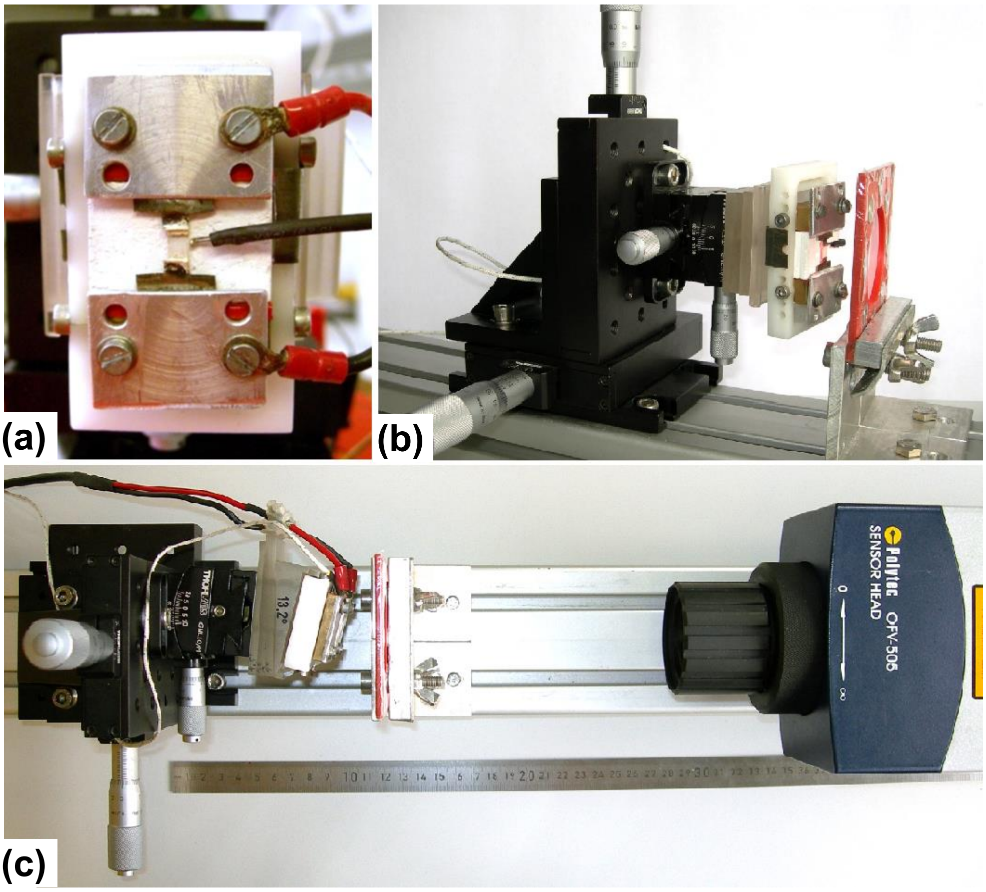

FIG. 3.8 (a) Electrically contacted thermophone sample in the holder. The black wire in the middle, with a small metallic tip, is the thermometer sensor. **(b)** Positioning unit and the sensing polyethylene film mounted on a plastic frame. **(c)** Top view on the measurement setup.

The experimental setup, the relevant equipment and the measurement procedure for the generated sound pressure is the same as in previous experiments (see Figure 3.4) and is described in Section 3.2. To minimize the standing-wave effect between thermophone and sensing polyethylene film, the angle α of incidence was set to 15 degrees (see Figure 3.8(c)).

As already discussed in the previous section, for the measurement of sound pressures in the MHz range, the distance between thermophone and the sensing point on the polyethylene film should be kept below a few centimeters due to the sound attenuation in air. Hence, in this experiment, the distance between the thermophone and the sensing point on the polyethylene film was set for each sample at 20 ± 0.25 mm.

In addition, due to acoustic near-field effects and resulting sound-beam directivity at frequencies > 200 kHz (see Figure 3.9), the thermophone had to be positioned with an accuracy of at least ± 100 µm with respect to the observation point on the sensing polyethylene film. Figure 3.9 depicts the sound field calculated from the EDF model for a 65 nm thin, 5 × 5 mm^2 thermophone under continuous sinusoidal excitation without offset at 2 Watt effective electrical input power and a frequency f_{th} of 800 kHz. Hence, two-way micrometer translation stages with a dual-axis goniometric stage were used for the positioning of the thermophone samples (see Figures 3.8(b) and 3.8(c)).

As was already discussed in section 2.1, for the generation of a single-frequency signal a thermophone should be driven by a sinusoidal voltage without an offset and at half of the desired frequency. Hence, all of the thermophone samples tested in this experiment were excited with a continuous sinusoidal voltage without an offset and with a constant amplitude in a frequency range from 1 kHz to 500 kHz and in 1 kHz steps.

The electrical resistances of the ITO coatings depend on their thickness and temperature. Hence, all samples were electrically preheated before starting the measurements. Finally, the amplitude of the excitation power was set for each sample at 2 ± 0.05 Watt.

The temperatures of the thermophones were measured with a small thermometer fixed on a glass substrate (see Figure 3.8(a)). The measured temperature of the tested thermophones during the experiments was about 186 °C for all samples.

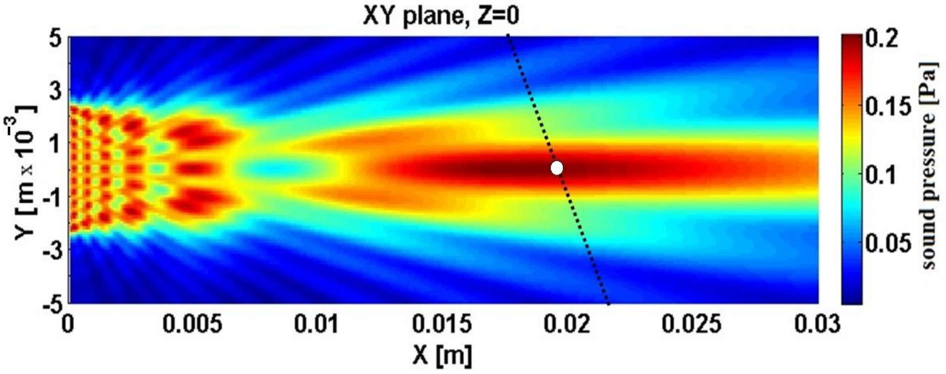

FIG. 3.9 Sound-pressure distribution in the XY-plane calculated from the EDF model for a 65 nm thin, 5 × 5 mm^2 ITO coating on a Herasil2-glass substrate placed at zero in the YZ-plane. The operational frequency f_{th} is 800 kHz. Effective electrical input power is 2 Watts. The dotted line and the white point mark the positions of the sensing polyethylene film and of the sensing point of the laser-vibrometer, respectively.

The ambient atmospheric pressure depended on actual the weather and varied during the experiments in a range of at most ± 0.5 kPa. This variation is marginal compared to the 100 kPa of normal pressure and can be neglected. The room temperature was kept at 24 ± 1 °C during the experiments. The values for the temperatures of the glass substrate, the adjacent air, and the atmospheric pressure were used for determining temperature- and pressure-dependent thermodynamic parameters of the EDF model and finally for calculations of the expected sound-pressure levels for the given thermophones and experimental parameters.

Figure 3.10 presents a comparison of the sound-pressure levels, observed experimentally and of those calculated from the EDF model, as functions of the thickness of the ITO-layers and of the thermal excitation frequency f_{th}. The experimentally detected frequency-dependent noise level of the measurement system is also plotted in the Figure 3.10 as a dashed line. The upper dotted line represents the theoretically expected sound-pressure level if the ITO film had a thermal capacitance and a thermal inertia of zero.

Comparison between sound-pressure levels measured experimentally and those predicted from the EDF model shows an absolute error of less than ± 2 dB for all tested thermophone samples. The theoretical overestimation of the generated sound-pressure levels at high frequencies can be traced back to an optimistic estimate of the ITO density and its heat capacity to be ρ_{ITO} = 7090 kg/m^3 and $c_{p\ ITO}$ = 300 J/kg·m^3. Especially the heat capacity of ITO depends on its oxidation degree and can vary in a range of ± 20 %. For instance, the use of a 5 % larger value for the ITO heat capacity fits also the experimental results for thermophone samples with 1.06 and 1.44 µm thick ITO-layers with an accuracy of better than ± 1 dB.

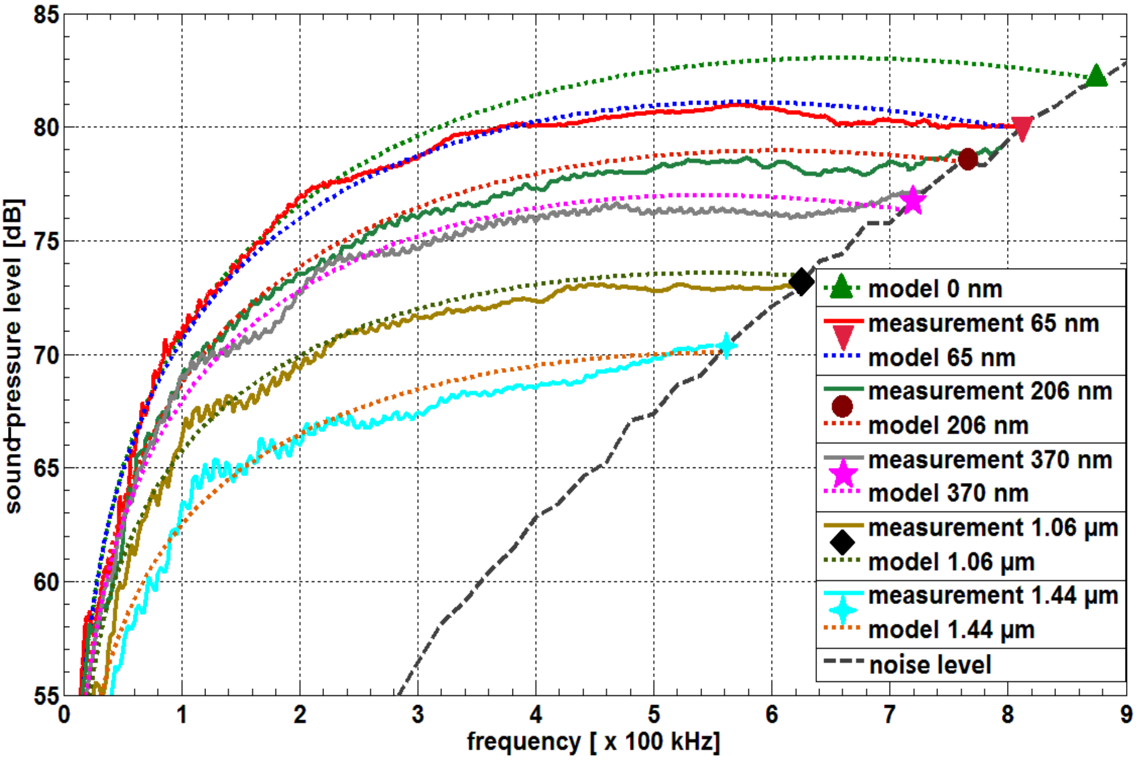

FIG. 3.10 Comparison of sound-pressure levels detected experimentally (solid lines) and calculated from the EDF model (dotted lines) as function of the operating frequency f_{th} for five tested thermophones with different ITO-layer thicknesses. The dashed line indicates the noise level of the measurement system.

The experimental results clearly demonstrate the influence of the increased film thickness on the sound-pressure level generated by substrate-based thermophones. Moreover, the experimental results clearly confirm the prediction from the EDF model that the square-root term in the energy distribution function $E_{gas}(T,P,f_{th})$ (see Equation (2.20)) leads for large C_{film} and for high excitation frequency f_{th} to a significant deviation from linearity towards the square-root dependence predicted by Arnold and Crandall [2] for free-standing thermophones. Furthermore, the experimental results confirm the prediction from the EDF model that the thermal inertia of the electrically conductive film (see Equation (2.19)) acts non-linearly, like a thermal low-pass filter. Its influence grows with the increase of the excitation frequency and reduces the amplitude of the generated sound pressure. For example, the difference of the sound-pressure levels generated with samples of 65 nm and 1.44 µm thickness is on the order of about 6 dB at 50 kHz and of about 12 dB at 500 kHz (see Figure 3.10). Thus, the thermal inertia of the heat-producing film is an important factor for an efficient thermal ultrasound generation in the MHz range and should not be neglected.

In contrast to previous models describing thermophonic sound generation in gases, only the EDF model involves the frequency-dependent thermal inertia of the heat-producing film and thus explains the experimental findings of all previous results indicating that the generated sound pressure $p(f)$ is proportional to $f - f^{0.5}$.

3.4 Experimental examination of thermophones in various gases

For the experimental validation of the EDF model in various gases, a thermophone sample consisting of a 50-nm thin and 3 × 3.5 mm^2 area ITO coating on a Herasil2 (quartz-glass) substrate was tested for sound generation in air, Ar, He, O_2, N_2 and SF_6. The ITO coating was produced in a plasma sputtering process. Thereafter, the sample was annealed for two hours at 300°C in O_2 to ensure complete oxidation of the ITO-layer. To test the thermophone in various gases, the experimental setup is used as shown in Figure 3.11. All cables and hoses are mounted vacuum-tight in the plastic plate. The positioning unit, the thermophone as well as the sensing polyethylene film are located under the glass dome. The laser-vibrometer is placed outside and is focused on the polyethylene film. The glass wall has no influence on the detection of the displacement of the polyethylene film.

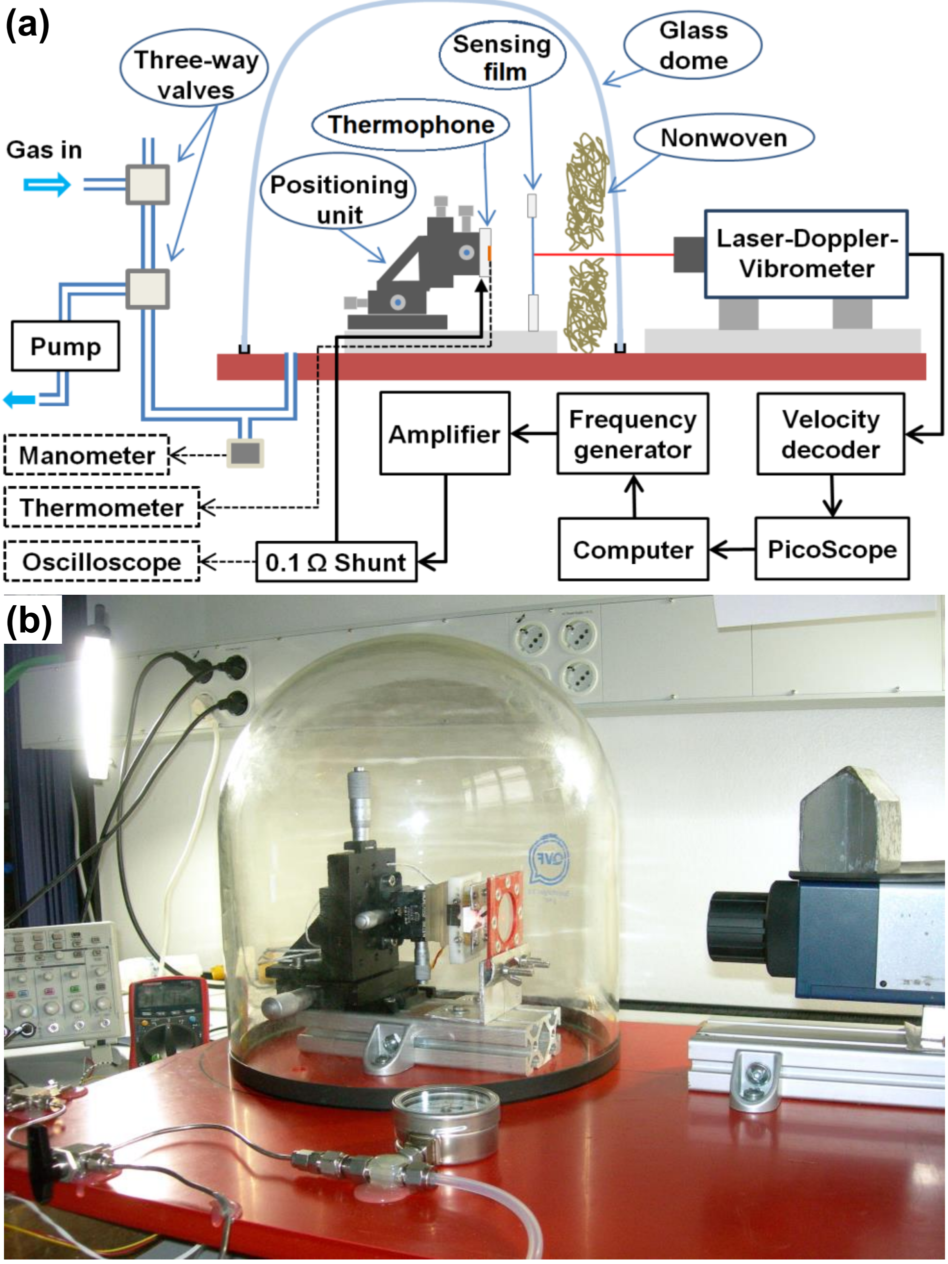

FIG. 3.11 Experimental setup for the measurement of the particle velocity and the sound pressure in several gases. **(a)** Schematic experimental setup. **(b)** Photograph of the laboratory setup.

The 3-cm-thick nonwoven fabric between the sensing polyethylene film and the glass dome acts as scatterer and absorber in the ultrasonic wave field and diminishes reflections at the glass wall and thus possible distortions of the results.

As was already discussed in previous sections, in order to measure the generated sound pressure at frequencies up to 1 MHz, the distance between the thermophone and the sensing polyethylene film has to be kept in the range of a few centimeters due to sound attenuation in the gases. Hence, in this experiment, the distance between the thermophone and the sensing point of the laser vibrometer on the polyethylene film was set at 20 ± 0.1 mm. To reduce possible measurement inaccuracies, the angle α between the thermophone sound beam and the normal of the sensing polyethylene film (see Figure 3.4, schematic experimental setup) was set to 0 degrees.

Whether the experimental setup is vacuum-tight, has been tested by leaving the evacuated dome under vacuum without pumping over a weekend. The subsequent check of the dome pressure showed no changes. To evacuate the dome, a two-stage diaphragm pump was used.

Before starting the measurements, the dome was repeatedly evacuated (down to 500 Pa residual pressure) and flooded (up to 100 kPa) with 99.999 % pure gas to ensure a minimum gas purity of at least 99 %.

Since the electrical resistance of the ITO coating is temperature-dependent, the thermophone sample was electrically pre-heated prior to starting the measurement. After achieving the thermodynamic equilibrium temperature, the electric resistance of the ITO coating reached a constant value. Finally, for measurements in all gases, the effective value of the supplied electric power $P_{el\,eff}$ was set at 1.5 ± 0.01 Watt.

The thermophone sample was excited using a continuous sinusoidal offset-free voltage of constant amplitude in a frequency range from 2.5 to 500 kHz in 2.5 kHz steps.

The temperature of the thermophone was measured during the experiments by means of a temperature sensor fixed on the glass substrate (see previous experiment, Figure 3.8(a)). During the experiments, the measured values of the thermophone temperature ($T_{Thermophone}$) were about 130°C for He, 140°C for Ar, 145 °C for air, N_2 and O_2, and 120°C for SF_6.

The measurement procedure for the generated sound pressure is the same as in previous experiments.

Figure 3.12 shows the measured sound-pressure amplitudes generated by the tested thermophone consisting of a 50-nm thin, 3 × 3.5 mm^2 ITO coating on Hersil2 quartz-glass substrate in air, Ar, O_2, N_2, He or SF_6 at 20 ± 0.2 °C and 100 ± 0.5 kPa pressure.

The periodic oscillations of the sound-pressure amplitudes occur because of constructive / destructive interference of the incident and reflected sound waves between the thermophone and the sensing polyethylene film. The periodic amplitude variation can be suppressed by applying a smoothing algorithm on the raw experimental data.

The Savitzky-Golay ("sgolay") smoothing algorithm implemented in MATLAB was applied to smooth the raw experimental data. The smoothing method uses a generalized moving average with filter coefficients which are automatically determined by an weighted linear least-squares regression and a polynomial model. The results of the smoothing algorithm are plotted in Figure 3.12 as dotted lines.

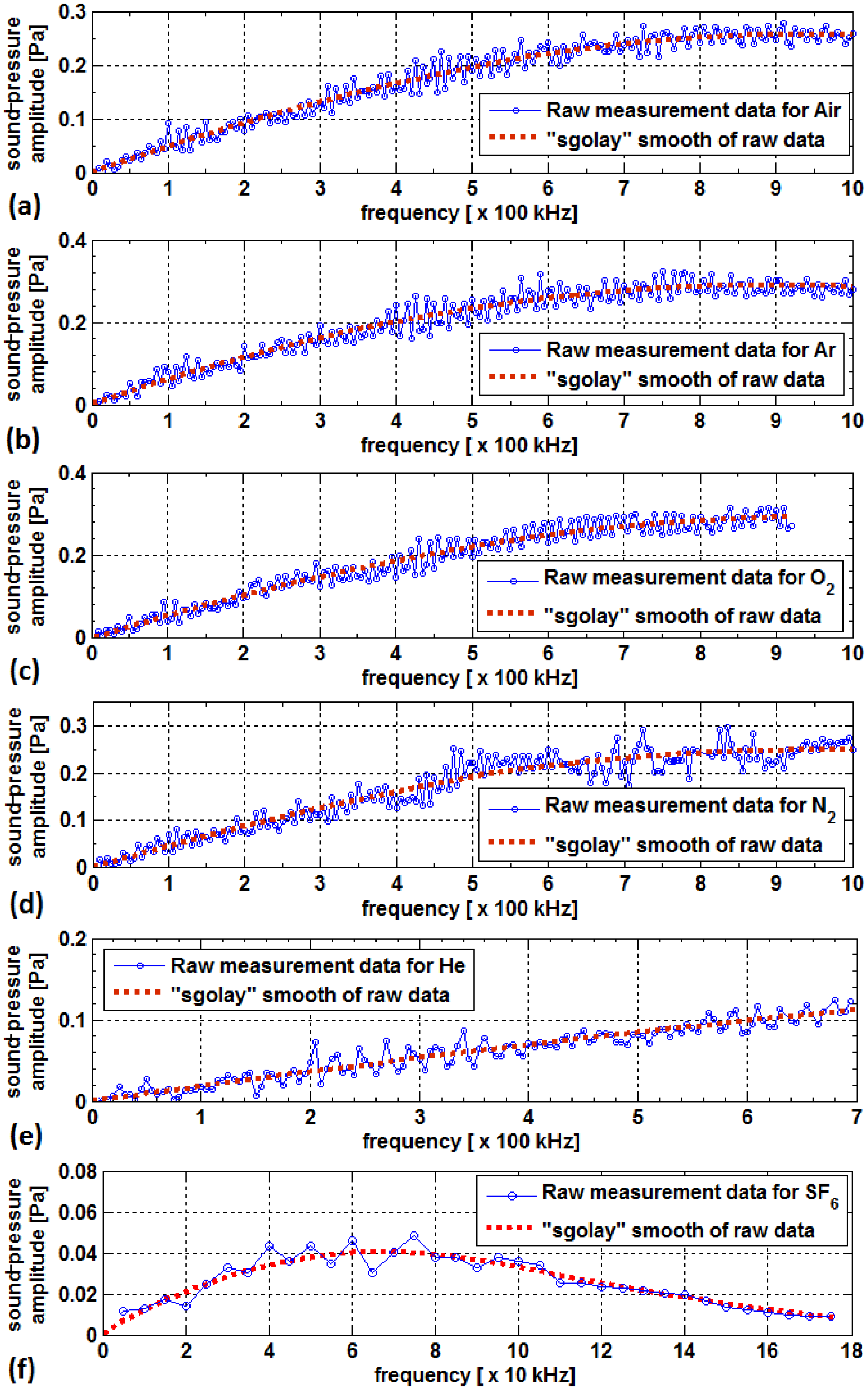

FIG. 3.12 Measured sound-pressure amplitudes generated by a thermophone consisting of a 50-nm thin, 3 × 3.5 mm^2 ITO coating on Hersil2-glass in **(a)** air, **(b)** Ar, **(c)** O_2, **(d)** N_2, **(e)** He and **(f)** SF_6 at 20°C and 100 kPa versus the thermal excitation frequency f_{th}. Dotted lines are “sgolay”-smoothing of raw experimental data.

TABLE 3.2 Gas properties at the thermophone temperature and at 100 kPa dome atmospheric pressure.

	Heat conductivity λ [W/m·K]	Density ρ [kg/m^3]	Heat capacity at constant volume c_v [J/kg·K]	Degrees of freedom F_{DoFs}
He at 130°C	0.226 [28,30,31,33]	0.1157 [28,30,33]	3229.3 [28,30,33]	3.1 Eq.(2.36)
Ar at 140°C	0.0227 [28-32,35-37]	1.167 [29,30,32]	332.8 [29,30,32]	3.2 Eq.(2.36)
N₂ at 145°C	0.0334 [28-32,35]	0.813 [28-32]	750.83 [28-32]	5.1 Eq.(2.36)
O₂ at 145°C	0.0371 [28-32,35]	0.921 [28-32]	685.43 [28-32]	5.25 Eq.(2.36)
Air at 145°C	0.0346 [28,29,31,32,34]	0.8359 [28,29,32,34]	737.84 [28,29,32,34]	5.15 Eq.(2.36)
SF₆ at 120°C	0.021 [31,39,40]	4.25 [39,40]	755 [39,40]	26.52 Eq.(2.36)

After the post-processing of measurement data, we can compare the measured and the EDF model-predicted sound pressures for all tested gases.

In order to calculate precisely the distribution of thermal energy between the substrate, the ITO film and the gas, the heat conductivities, heat capacities and densities of the materials at given thermophone temperature ($T_{Thermophone}$) have to be taken into account. The temperature of the gas layer close to the thermophone can be assumed to be equal to the observed glass-substrate temperature. Table 3.2 summarizes the properties of the tested gases at a given thermophone temperature.

For Herasil2 quartz-glass substrate, the manufacturer specification [27] is used to obtain the following linear approximations for its heat conductivity and specific heat capacity:

$$\lambda_{glass}(T_{Thermophone})\left[\mathrm{W}/_{\mathrm{m}\cdot\mathrm{K}}\right]=1.32+1\cdot10^{-3}\cdot T_{Thermophone}[°\mathrm{C}], \tag{3.16}$$

$$c_{p\,glass}(T_{Thermophone})\left[\mathrm{J}/_{\mathrm{kg}\cdot\mathrm{K}}\right]=700+0.934\cdot T_{Thermophone}[°\mathrm{C}]. \tag{3.17}$$

The temperature-dependent change of the glass density can be calculated from the volumetric thermal-expansion coefficient of the glass ($\gamma_{glass}=1.74\cdot10^{-6}/\mathrm{K}$ [27]):

$$\rho_{glass}(T_{Thermophone})\left[\mathrm{kg}/_{\mathrm{m}^3}\right]=2203\cdot(1-1.74\cdot10^{-6}\cdot T_{Thermophone}[°\mathrm{C}]) . \tag{3.18}$$

The experimental data for thin ITO (90/10) coatings as listed in [41] are employed to obtain linear approximations for the temperature-dependent heat capacity, density and thickness of the 50-nm-thin ITO coating used in this experiment:

$$c_{p\,ITO}(T_{Thermophone})\left[\mathrm{J}/_{\mathrm{kg}\cdot\mathrm{K}}\right]=349+0.174\cdot T_{Thermophone}[°\mathrm{C}], \tag{3.19}$$

$$\rho_{\,\mathrm{ITO}}(T_{Thermophone})\left[\mathrm{kg}/_{\mathrm{m}^3}\right]=7090\cdot(1-21.25\cdot10^{-6}\cdot T_{Thermophone}[°\mathrm{C}]) , \tag{3.20}$$

$$d_{ITO}(T_{Thermophone})[\mathrm{nm}]=50\cdot(1+7.25\cdot10^{-6}\cdot T_{Thermophone}[°\mathrm{C}]) . \tag{3.21}$$

The parameters in Table 3.2 and the Equations (3.16)-(3.21) are used to calculate the thermal effusivities of the Herasil2-glass substrate and gases and finally to determine the amount of thermal energy $\Delta Q_{gas}(T,P,f_{th})$ flowing into the gas (see Equation (2.25)).

TABLE 3.3 Gas properties at 20°C and 100 kPa pressure

	He	**Ar**	**N$_2$**	**O$_2$**	**Air**	**SF$_6$**
$\boldsymbol{M_{gas}}\cdot10^{-3}$ [kg/mol]	4.0026 [42]	39.948 [42]	28.0134 [42]	31.9988 [42]	28.97 [42]	146.055 [42]
$\boldsymbol{\rho}$ [kg/m^3]	0.1642 [28,30,33]	1.6391 [29,30,32]	1.1494 [28-32]	1.3129 [28-32]	1.189 [28,29,32,34]	6.1 [39,40]
$\boldsymbol{c_{sound}}$ [m/s]	1000.7 Eq.(2.42)	318.9 [32], Eq.(2.42)	349.1 [32], Eq.(2.42)	326.05 [32], Eq.(2.42)	343.3 [32], Eq.(2.42)	134 [39,40], Eq.(2.42)
$\boldsymbol{\lambda_{gas}}$ [W/m·K]	0.1567 [28,30,31,33]	0.01782 [28-32,35-37]	0.0259 [28-32,35]	0.0264 [28-32,35]	0.0263 [28,29,31,32,34]	0.0117 [31,39,40]
$\boldsymbol{c_v}$ [J/kg·K]	3160 [28,30,33]	312 [29,30,32]	743 [28-32]	658.94 [28-32]	719 [28,29,32,34]	603 [39,40]
$\boldsymbol{c_p}$ [J/kg·K]	5230 [28,30,33]	523 [29,30,32]	1040 [28-32]	916 [28-32]	1005 [28,29,32,34]	663 [39,40]
$\boldsymbol{\mu_{dyn}}$ [μPa·s]	18.66 [29,30,32,33]	22.31 [30,32,43,45,46]	17.57 [28,29,32,43,45]	19.24 [28,29,32,43]	18.2 [28,29,32,34,43]	15.27 [44,45]
$\boldsymbol{\mu_{bulk}}$ [μPa·s]	unknown	unknown	Experimental value 0.73·μ_{dyn} [47-49]	Experimental value 0.4·μ_{dyn} [48,49]	Theoretical value from this work 0.63·μ_{dyn}	Theoretical value 340·μ_{dyn} [50]
	Experimental result of this work: 0.33·μ_{dyn}	Experimental result of this work: 0.32· μ_{dyn}	Experimental result of this work: 0.73·μ_{dyn}	Experimental result of this work: 0.45·μ_{dyn}	Experimental result of this work: 0.63·μ_{dyn}	Experimental result of this work: 300·μ_{dyn}
	Gas specific van-der-Waals constant *b* [42]					
$\boldsymbol{b}\cdot10^{-3}$ [m^3/mol]	0.0238	0.03201	0.0387	0.03186	0.0364	0.08786

To calculate the volume of the generated sound wave $V_{wave}(T,P,f_{th})$ (see Equation (2.28)), the sound attenuation function $A(T,P,r,f_{th})$ (see Equation (2.39)) and finally the generated sound pressures at the measurement point, the gas properties at dome temperature and pressure as listed in the Table 3.3 are used.

Most gas parameters listed in Table 3.3 are well known and can be found, for instance, in handbooks on chemistry and physics. The values for bulk viscosities of gases are still mostly unknown. As discussed in [48,50], the bulk viscosities of monatomic gases have to be very small and possibly equal to zero. To the best of the author's knowledge, the bulk viscosities of Helium and Argon at given temperature and pressure are unknown. The experimentally measured values for the bulk viscosities of O$_2$ and N$_2$ can be found in [47-49]. These values can be used to estimate the bulk viscosity of air. Assuming air is composed of 78 % N$_2$ and 22 % O$_2$, the bulk viscosity of air can be calculated as follows, $\mu_{bulk\,air} \approx \mu_{bulk\,\mathrm{N2}}\cdot 0.78 + \mu_{bulk\,\mathrm{O2}}\cdot 0.22 = 11.7$ μPa·s and thus, $\mu_{bulk\ air} \approx 0.63\cdot\mu_{dyn\ air}$. A theoretical value for the bulk viscosity of SF$_6$ gas, $\mu_{bulk\ SF6} \approx 340\cdot\mu_{dyn}$, can be found in [50].

Since all remaining gas parameters are well known, let us first compare the measured and from the EDF model predicted sound pressures, ignoring the bulk viscosities of the respective gases. For clarity, the "sgolay"-smoothed experimental data for all tested gases are plotted in Figures 3.13 and 3.14.

In Figure 3.13, the sound pressures generated by the respective thermophone and the values predicted from the EDF model, ignoring the bulk viscosities of the gases, are compared.

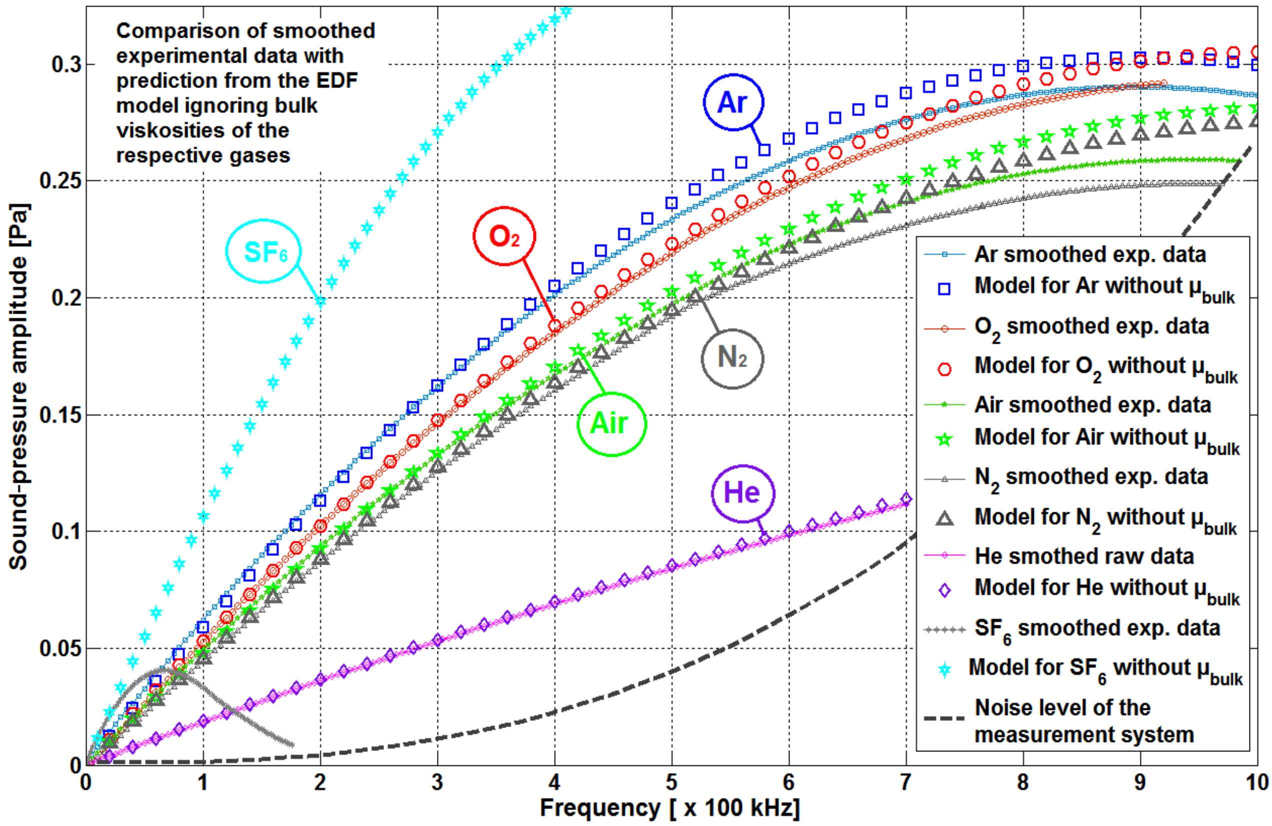

FIG. 3.13 Comparison of "sgolay"-smoothed experimental data (dotted lines) and the sound pressures (marked) predicted from the EDF model (bulk viscosities are ignored) versus the thermal excitation frequency f_{th}. The dashed line represents the noise level of the measurement system.

As one can see in Figure (3.13), the influence of the bulk viscosity is small for mon- und diatomic gases and is noticeable only at high frequencies (> 300 kHz). This confirms the assumption of Pen *et al*. [48] and of M. S. Cramer [50] that bulk viscosities of monatomic gases are small ($< 0.5{\cdot}\mu_{dyn}$). For SF_6, a large deviation is observed already at frequencies above 30 kHz. This deviation can be traced back to a strong sound attenuation in the SF_6 gas due to a large ($\approx 340{\cdot}\mu_{dyn\ \mathrm{SF6}}$) bulk viscosity of this gas (see Table 3.3).

Since all gas parameters (except the bulk viscosities) are well known, the values for bulk viscosities of the respective gases can be determined by minimizing the deviation between the measured and the EDF model-predicted sound-pressure amplitudes at high frequencies. In doing so, the bulk viscosity values listed in Table 3.3 as "experimental results of this work" are obtained. The results confirm the values for the bulk viscosity of O_2, $\mu_{bulk\ \mathrm{O2}} = 0.4{\cdot}\mu_{dyn\ \mathrm{O2}}$, and N_2, $\mu_{bulk\ \mathrm{N2}} = 0.73{\cdot}\mu_{dyn\ \mathrm{N2}}$, as given in [47-49], as well as the value for the bulk viscosity of air, $\mu_{bulk\ air} \approx 0.63{\cdot}\mu_{dyn\ air}$, calculated theoretically in this work. For the bulk viscosities of Helium and Argon, the following values were obtained: $\mu_{bulk\ \mathrm{He}} \approx 0.33{\cdot}\mu_{dyn\ \mathrm{He}}$ and $\mu_{bulk\ \mathrm{Ar}} \approx 0.32{\cdot}\mu_{dyn\ \mathrm{Ar}}$. For SF_6, a value of about $\mu_{bulk\ \mathrm{SF6}} \approx 300{\cdot}\mu_{dyn\ \mathrm{SF6}}$ was obtained. This value is about 12 percent smaller than the value of $340{\cdot}\mu_{dyn\ \mathrm{SF6}}$ theoretically predicted by the Enskog-model and calculated by M. S. Cramer [50].

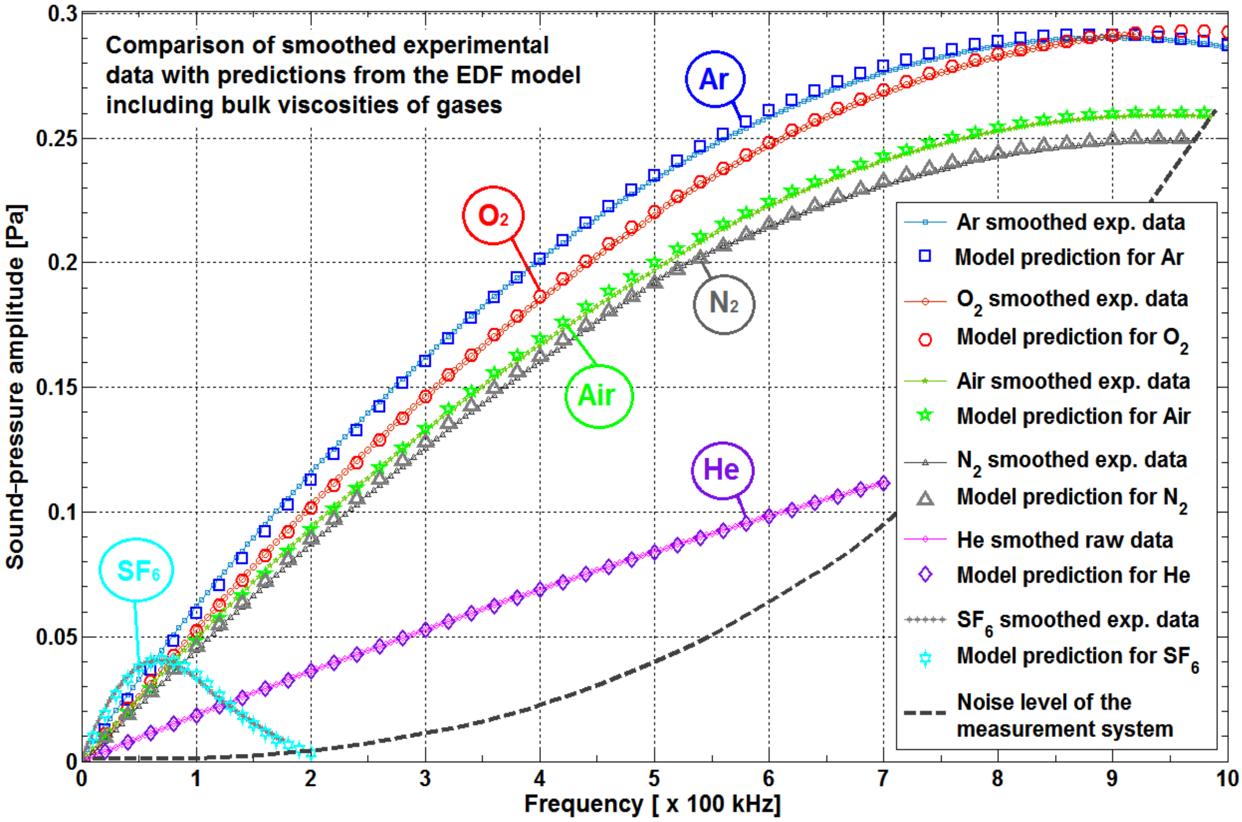

FIG. 3.14 Comparison of “sgolay”-smoothed experimental data (dotted lines) and sound pressures (marked) predicted from the EDF model versus the thermal excitation frequency f_{th} and including bulk viscosities of the respective gases. The dashed line represents the noise level of the measurement system.

In Figure 3.14, the measured and the model-predicted sound pressures including the bulk viscosities of gases are compared. As one can see in Figure 3.14, the predicted sound pressures are in good agreement with the experimental results even for frequencies up to 1 MHz. The maximum deviation between the measured and the EDF model-predicted sound pressures is in the range of ± 4 % for all gases. This discrepancy is a result of small deviations of all the parameters which were used for the model prediction.

Thus, the experimental results clearly confirm the prediction made from the EDF model. Additionally, measurements of thermally generated sound pressures in monatomic gases such as Helium and Argon confirmed that the thermal energy supplied to a monatomic gas is entirely carried away by the generated acoustic wave. This means that the gas layer does not store any thermal energy and consequently does not expand. This fact contradicts the idea of an expanding gas layer working as imaginary piston and is an additional indicator for the validity of the EDF model.

3.5 Summary and discussion

For the experimental validation of the EDF model, different thermophone samples of various sizes, shapes and materials were tested for sound generation in several gases with in a frequency range from 1 kHz to 1 MHz. The frequency range is 10 – 20 times wider than in all the experimental studies on thermophones published so far. It can be assumed that thermophones are also capable to produce ultrasound at frequencies higher than 1 MHz. However, the frequency range in this study was limited to 1 MHz due to increasing noise levels of the measuring equipment.

To measure thermally generated sound pressures a Laser-Doppler-Vibrometer combined with a 12-µm-thin polyethylene film placed in the sound field was used as a broadband, non-resonant sound-pressure detector. The method allows for measurements of particle velocity and sound pressure in all optically transparent gases with known density and speed of sound. The advantages of the present method compared to conventional sound-pressure detectors such as condenser microphones or piezo-electric transducers are:

- no calibration required;
- a large dynamic measuring range (from µPA to MPa) and a high bandwidth (from few Hz to few MHz);
- suitability for measurements in optically transparent gases; and
- resonance-free frequency response.

The tested thermophone samples included free-standing carbon-nano-wire webs (CNW) of different thickness (5 – 150 µm), size and shape, and also different substrate-based thermophones consisting of Titanium and Indium-Tin-Oxide (ITO) coatings of different thickness (20 – 2500 nm), size and shape on polycarbonate and quartz-glass substrates. Altogether, more than fifty different thermophone samples were tested for sound generation.

As expected, all thermophone samples showed a resonance-free frequency response across entire tested frequency range. Thus, thermophones can be used as broadband, non-resonant ultrasound sources.

As predicted from the EDF model, the thermally generated sound-pressure amplitude is linearly related to the input power and to the thermal excitation frequency. An initially linear increase of the sound-pressure amplitude with increasing excitation frequency is impeded by the frequency-dependent thermal inertia of the heat-producing film and by sound attenuation in the gas.

Being more precise, with the increase of the excitation frequency, the frequency-dependent thermal inertia of the electrically conductive film (for both free-standing and substrate-based thermophones) leads to a significant deviation from linearity towards the square-root dependence predicted by Arnold and Crandall [2] and Xiao et al. [8,9] for free-standing thermophones. Thus, the EDF model explains the experimental findings of all previous studies that the generated sound pressure $p(f)$ is proportional either to f, or to $f^{0.7-0.8}$ or to $f^{0.5}$.

The influence of the thermal capacity of the electrically conductive film on the sound pressure for substrate-based thermophones was investigated experimentally in a frequency range from 10 to 800 kHz with thermophones consisting of ITO coatings of different thickness (65 – 1400 nm) on quartz-glass substrates.

Unlike the prediction made by the models of Shinoda *et al.* [5], Boullosa *et al.* [6], Tian *et al.* [11], Vesterinen *et al.* [15] and Hu *et al.* [16] (which do not include a heat-producing film), experimental results for substrate-based thermophones confirmed the prediction made from the EDF model and showed that the thermal inertia of an electrically conductive film also has a negative influence on the acoustic efficiency of substrate-based thermophones and should not be ignored.

The best possible acoustic performance of a thermophone on a substrate can be achieved by using:

a) an electrically conductive film with the smallest possible thickness d_{film}, density ρ_{film} and specific heat capacity $c_{p\,film}$;

b) a substrate with the smallest possible thermal effusivity e_{sub}.

Condition (a) confirms the findings of Arnold and Crandall [2] and Xiao et al. [8,9] for free-standing thermophones, and condition (b) confirms the findings of Shinoda [5], Boullosa [6], Tian et al. [11] and Hu et al. [16] for substrate-based thermophones.

The main reason to use quartz-glass and polycarbonate as substrates in this experimental study is that the density, heat conductivity and thermal capacity of these materials are well known. Additionally, these substrates have a smooth surface with a roughness smaller than 2 nm. Thus, the Titanium and ITO coatings used as electrically conductive films can be assumed to be homogeneous layers of constant thickness.

In order to experimentally validate the EDF model in various gases, the sound pressure generated by a thermophone consisting of a 50-nm-thin ITO coating on a quartz-glass substrate was measured in 99.99 % pure gases such as He, Ar, O_2, N_2, Air and SF_6 in a frequency range up to 1 MHz. The maximum deviation between the measured and the model-predicted sound pressures is in the range of ± 4 % for all gases.

For all substrate-based thermophones tested in “open” air, deviations of less than ± 10 % have been observed between the detected and model-predicted sound-pressure levels. The reasons for these deviations are: differences in the film thickness, weather-dependant variations of air humidity, room temperature and pressure, and about ± 2 % variations of the supplied electrical-power amplitude.

For all free-standing thermophone samples tested in “open” air, maximum differences of ± 15 % were observed between the measured and the model-predicted sound pressure levels. The reasons for such relatively large differences are the inhomogeneities of the CNW samples and an approximate estimation of the sample thickness, density and heat capacity.

The prediction accuracy of the EDF model strongly depends on the precision of the relevant thermodynamic and physical parameters of gases, substrate and electrically conductive film materials. The main parameters affecting the prediction accuracy are: the speed of sound of the gas, the ratio of the thermal effusivities of substrate and surrounding gas, the input power, the number of degrees of freedom of the gas molecule, the heat capacity of the electrically conductive film and the sound attenuation in the gas.

In contrast to all models that existed up to now and that describe thermophonic sound generation in gases, only the EDF model is generalized and can be applied to predict the sound pressure generated by free-standing as well as by substrate-based thermophones with an acceptable accuracy of ± 4 – 15 %. Thus, the experimental results for all tested thermophone samples clearly confirm the predictions of the EDF model.

Concerning a better understanding of the underlying physical principles, it could be shown that thermophonic sound generation in gases occurs without thermal expansion of a gas layer. If the gas layer close to the thermophone expanded, it would have to store some of the supplied thermal energy, which would reduce the generated sound-pressure amplitude. But this does not happen. Measurements of thermally generated sound pressures in monatomic gases such as Helium and Argon show that the thermal energy supplied to the gas is entirely carried away by the acoustic wave. This means that the gas layer does not store thermal energy and consequently does not expand. Also, the experimental results for free-standing CNW samples contradict the assumption of an imaginary gas piston and an expanding and contracting air layer that generates the acoustic waves. If the air inside a porous heater such as for example a carbon-nano-wire web would expand these thermophones should generate considerably higher sound pressures, and all the more so the thicker the sample. However, the experimental results show that the air inside the CNW-web stores the supplied thermal energy and does not contribute to the excited sound pressure. Moreover, the air inside the CNW-web acts as an additional thermal capacity of the heat-producing carbon-nano-wire web and leads to a reduction of the generated sound pressure.

4. Applications of thermophones

4.1 Investigating physical properties of gases

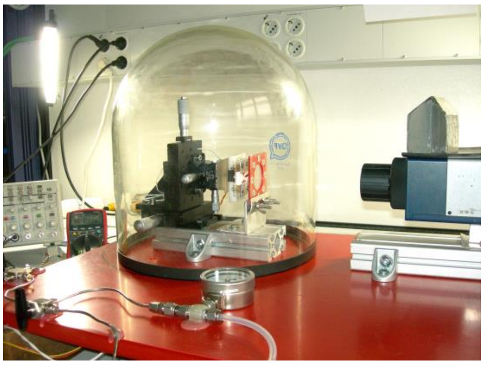

As discussed in Chapter 2 and demonstrated in the experimental results of Section 3.4 (Model validation in various gases), the sound pressure generated by a thermophone in any given gas strongly depends on the physical properties of the gas at a given temperature and pressure. Thus, in general, from the sound pressure generated by a thermophone in any gas, conclusions can be drawn about its physical properties.

For example, the number of degrees of freedom of the gas molecule, the speed of sound, the heat conductivity and the heat capacity of the gas or the sound attenuation in the gas can be investigated experimentally. Additionally, by variation of gas temperature and pressure and considering the generated sound pressure, activation or deactivation of degrees of freedom of the gas molecules may be observed. Furthermore, changes of the dynamic and bulk viscosities of a gas at different temperatures and pressures can be investigated. Thus, a thermophone could be a new scientific tool for the investigation of physical properties of gases.

4.2 Thermo-acoustic gas spectroscopy

The use of the photo-acoustic effect and is applied e.g. in gas spectroscopy [51,52] has long been known. Up to now, for the periodic heating of a gas inside a photo-acoustic cell, either expensive infrared lasers or infrared emitters with complex optical wavelength filters are employed. By avoiding the use of IR-Lasers and optical filters, compact and inexpensive thermo-acoustic gas spectrometers and analyzers can be fabricated.

The experiment shown in Figure 4.1 demonstrates the applicability of thermophones as heating elements for thermo-acoustic gas spectroscopy in a simple manner.

As demonstrator, a commercially available 60 Watt bulb is used as a closed cell filled with a gas. The filament is used as heating source. The bulb is connected to a linear amplifier driven by a frequency generator and is electrically excited with a monofrequent continuous sinusoidal voltage of 60 V and 0.5 A. The excitation frequency is increased in 100 Hz steps, and the sound pressure generated by the bulb is measured using ¼-inch Microtech Gefell condenser microphone, averaged over 4096 periods and saved on a computer.

Figure 4.1(b) shows sound-pressure levels generated in the bulb during continuous sinusoidal excitation with a constant amplitude in the frequency range from 20 kHz to 100 kHz and detected by means of a condenser microphone. Similar to a photo-acoustic cell, a resonant behavior is observed at certain frequencies. From this spectral “finger print”, conclusions can be drawn about the gas mixture in the cell. Thus, a thermophone could also be a new useful tool in the analytical chemistry of gases.

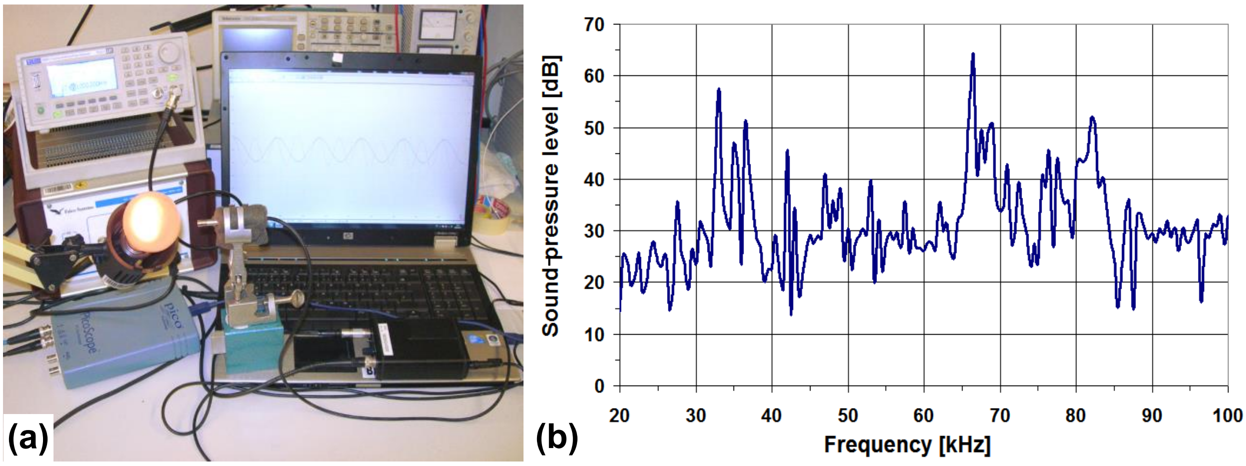

FIG. 4.1 Demonstration experiment for the applicability of thermophones as heating elements in thermo-acoustic gas spectroscopy. **(a)** Experimental setup. **(b)** Sound pressure levels measured with ¼ inch Microtech Gefell condenser microphone placed in distance of 3 cm from the bulb.

4.3 Broadband characterization of the transfer functions of airborne-ultrasound measurement systems

In general, the measurement of sound pressures requires a sensor system with a well-known transfer function. The most commonly used sensor systems are condenser microphones. These microphones must be tested and recalibrated regularly, typically once per year, or after any potentially damaging event such as being dropped or being exposed to sound pressures beyond the operational range of the device.

Up to now, the methods for the calibration of condenser microphones can be divided into two categories: primary and secondary methods. Reciprocity calibration is a primary method and is based on the reciprocity of condenser microphones. The method enables calibration with a high accuracy. However, it is a time-consuming and expensive procedure and is carried out only at the National Physical Laboratory in the United Kingdom, at the Physikalisch-Technische Bundesanstallt (PTB) in Germany and at the National Institute of Standards and Technology (NIST) in the USA. The secondary calibration methods include pistonphones and sound calibrators, the electrostatic actuator method, and the comparison method. Pistonphones and sound calibrators are strongly dependent on ambient temperature and pressure and are generally only used to reproduce low frequencies, typically between 250 Hz and 1 kHz. The comparison method requires a calibrated reference microphone which is used to calibrate other microphones by comparing the output signal of the “test” microphone to that of the reference microphone.

Each calibration method has its advantages and disadvantages, depending on its frequency range, its sound-pressure amplitude and its measurement uncertainty. A detailed discussion of calibration methods can be found for example in the work of Bouaoua [53].

The use of thermophones could be a new method for broadband calibration of sound-pressure and particle-velocity sensor systems.

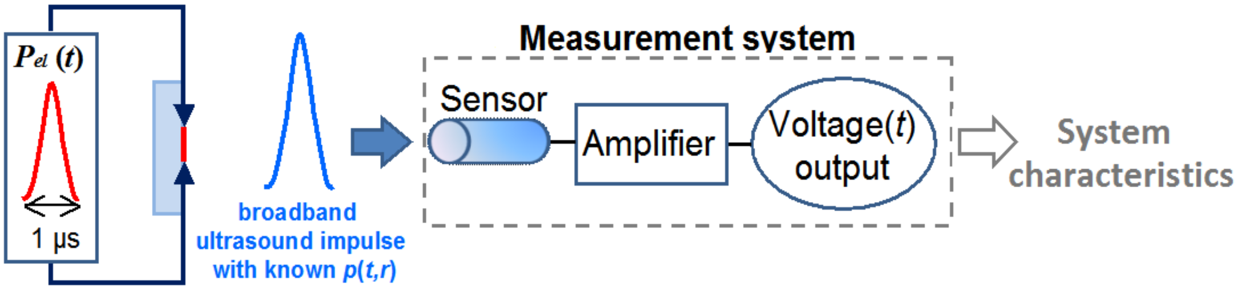

FIG. 4.2 Schematic representation of the characterization principle of the transfer functions of airborne-ultrasound measurement systems.

Because thermophones are broadband devices and have a well-known transfer function without resonances, they can be used for broadband characterization of the transfer function of any airborne-ultrasound measurement system such as microphones, and electromagnetic, piezoelectric or electrostatic transducers. Moreover, because the sound pressure generated by the thermophone can be accurately determined from the EDF model, the tested sensor system can be calibrated.

In general, a single broadband ultrasound impulse generated by a thermophone is sufficient to obtain the full information about the transfer characteristics of the tested measurement system.

These characteristics can be for example:

- the frequency band and the dynamic range of the sensor system,
- its frequency-, temperature- and pressure-dependent sensitivity spectrum in V/Pa (f, T, P),
- its linear or nonlinear behavior and its resonance frequencies.

Figure 4.2 schematically illustrates the characterization principle of using a thermophone for characterization of the transfer functions of an ultrasound measurement system.

In order to demonstrate the applicability of a thermophone for the characterization of the transfer function of an airborne ultrasound measurement system, let us test and compare

- a six-year-old condenser-microphone system from Microtech Gefell consisting of an MK301 microphone capsule combined with an MV302 preamplifier and an MN920 amplifier. The amplifier was set at its maximum amplification of x128. According to the manufacturer's specifications, the microphone has a linear frequency response up to 100 kHz and has a frequency-independent transmission factor of 640 mV/Pa.
- the Laser-Doppler-Vibrometer (LDV) with two velocity decoders, a VD06-decoder (with a transmission factor of 2 mm/s/V and cutoff frequency at 350 kHz) and a VD09-dekoder (with a transmission factor of 20 mm/s/V and cutoff frequency at 1 MHz) combined with a 12-µm-thin polyethylene film.

As a broadband ultrasound source, a thermophone consisting of 5 × 5 mm^2 large and 50-nm-thin titanium coating on a polycarbonate substrate is used.

Figure 4.3 shows photographs of the tested measurement systems and of the thermophone used as a broadband airborne-ultrasound source.

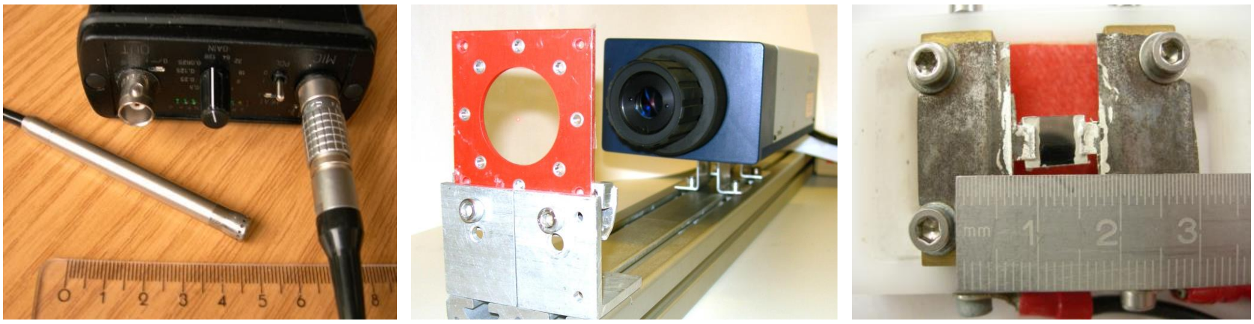

FIG. 4.3 Tested airborne-ultrasound measurement systems. Photograph on the left: MK301 condenser microphone with amplifier. Photograph in the center: Laser-Doppler-Vibrometer combined with a 12-μm-thin polyethylene film. Photograph on the right: Thermophone used as a broadband airborne-ultrasound source.

The sensors (the microphone or the polyethylene film) are positioned at a distance of 6 cm in front of the thermophone. The thermophone is excited with a 1 μs (1 MHz) pulse of 175 W effective power. For a 5 × 5 mm^2 thermophone in air, which is driven with 1 MHz pulses, the distance of 6 cm already corresponds to the acoustic far field. Thus, at the sensor position, the incident acoustic pulse can be considered as a quasi-planar wave.

Figures 4.4 and 4.5 show the experimental setup and the diagrams on the right show the time-dependent signals detected by the two measurement systems. The detected time signals are not filtered or averaged.

The condenser-microphone measurement system receives an acoustic signal of approximately 55 μs duration. The LDV in combination with the VD06-decoder records a single sound impulse of 3.5 μs duration, and the VD09-decoder receives a sound pulse of 1 μs duration and the small (at most 10 % of the maximum magnitude) internal noise of the measurement system.

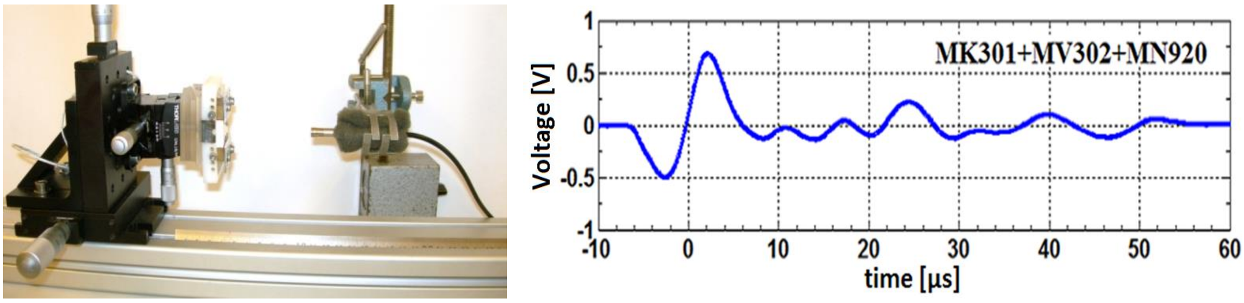

FIG. 4.4 Experimental setup for characterizing the transfer function of a condenser-microphone measurement system and the detected signal versus time.

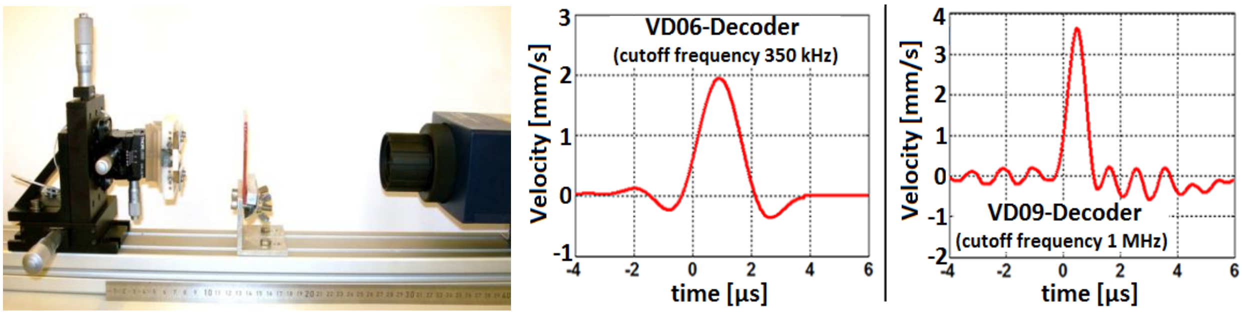

FIG. 4.5 Experimental setup for characterizing the transfer function of an LDV measurement system combined with two velocity decoders and the detected signals versus time.

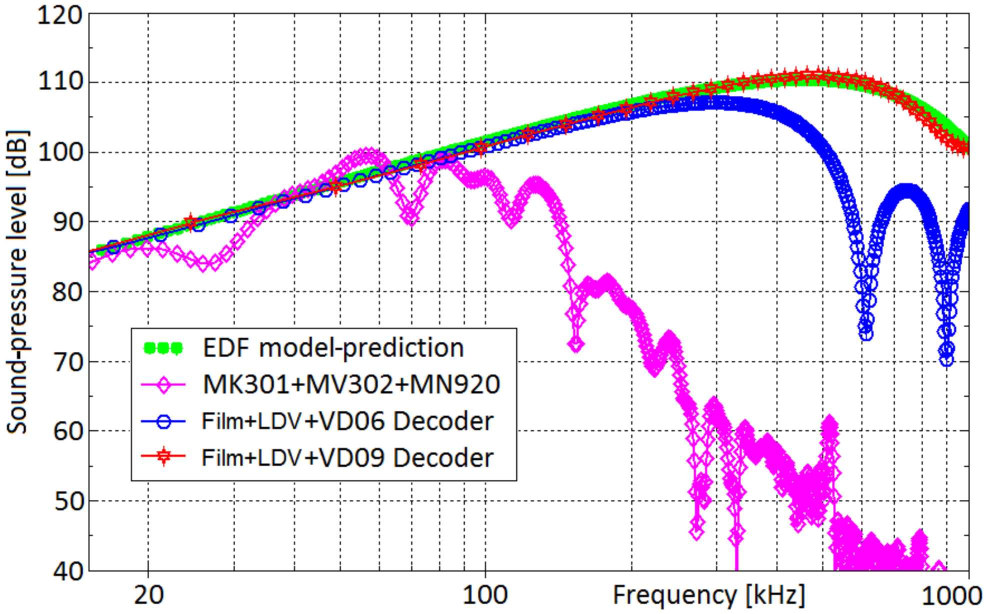

FIG. 4.6 Comparison of predicted and detected sound-pressure levels versus frequency.

After Fourier transformation of the detected time-depended signals and multiplication with the known transfer functions of the respective measurement systems, sound-pressure-level spectra of the detected acoustic signals are obtained. A detailed description of the calculation of the acoustic spectra from the detected time-dependent signals can be found in one of the author's recent publications [26]. Note that for characterizing the transfer function of a measurement system with an unknown transfer function, the detected frequency-dependent voltage and the EDF model predicted frequency dependence of the sound pressure have to be compared in order to obtain the sensitivity spectrum of the tested system in V/ Pa as a function of frequency, temperature and pressure.

Figure 4.6 shows the comparison of the model-predicted sound-pressure level for a thermally generated sound pulse at the sensor position (green curve) and the detected sound-pressure levels versus frequency.

As one can see in Figure 4.6, the LDV+VD09 decoder shows a deviation of less than 1.5 dB compared with the theoretically predicted sound-pressure levels for frequencies over 800 kHz. These deviations can be traced back to the internal noise of the measurement system and can be reduced by averaging the detected time signals. The measurement system shows no resonances and can be used for measurements in the full decoder range up to 1 MHz.

The measurement system consisting of the LDV combined with the VD06 decoder (the blue curve) shows also a resonance-free response and can be used for measurements up to 300 kHz.

More interesting is the result of the condenser-microphone measurement (shown in Figure 4.6 in magenta). The cutoff frequency of the microphone system is approximately at 120 kHz. Thus, the measuring system is not suitable or only of limited suitability for frequencies higher than 120 kHz. Additionally, as can be seen in Figure 4.6, the measurement system shows some deviations from the expected linear frequency response. For example, it shows a deviation of about 6 dB at 27 kHz and a deviation of about 8 dB at 68 kHz. Even during several repeated measurements, the deviations remained unchanged. The deviations may result from a cable defect, or some capacitors of the microphone amplifier have changed their capacity with time.

An important point is that these deviations cannot be detected if a low-frequency pistonphone or a sound calibrator is used for calibration of the measurement system.

The experimental results clearly demonstrate the applicability of thermophones for broadband testing and characterizing transfer functions of airborne-ultrasound measurement systems.

Undoubtedly, the same characterization can be conducted in any gases at any temperature and pressure. This is a big advantage of the thermophonic calibration method compared to existing calibration methods. Using only one thermophone combined with the EDF model proposed in this work, any measurement system may be tested over a large frequency range and calibrated for application in various gases. Figure 4.7 shows a possible experimental setup. Additionally, using this laboratory setup, the transmission properties characterization of transmit properties of ultrasonic transducers can be characterized in various gases or gas mixtures at different pressures and temperatures.

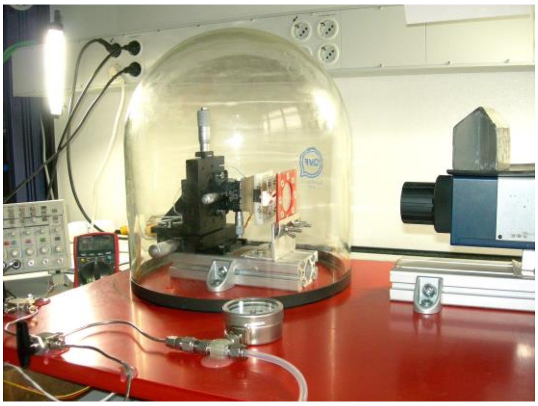

FIG. 4.7 A possible experimental setup for characterizing transfer functions of ultrasound transducers in different gases.

4.4 Applications of thermophones in non-destructive materials testing

Ultrasound-based methods for non-destructive testing (NDT) [54-56] are long known. In particular, airborne ultrasound has been gaining importance as a contact- and coupling agent-free inspection method and is increasingly applied in many technical fields, including for example non-contact quality control and health monitoring of lightweight materials and safety-relevant components for automobile and aerospace applications [57-59].

Currently, the most commonly used ultrasound transducers are piezo-electric or electro-static transducers that are basically damped mass-spring systems. The influence of the moving mass of a transducer is particularly strong in airborne-ultrasound transducers and manifests itself in the post-ringing of the transducer and in a “long” decay time (up to 200 μs) of the generated acoustic signal even after a 500 ns short-pulse excitation (see Figure 4.8). Further disadvantages of the moving mass of conventional airborne-ultrasound transducers include their resonances and the resulting narrow bandwidth (± 10 – 20 % of the main frequency).

Thermophones work without any moving parts and hence are resonance-free sound sources. Additionally, using pulse excitation, thermophones reach acoustical efficiencies comparable to those of conventional piezoelectric airborne-ultrasound transducers generating sound-pressure levels of about 140 dB and more at 6 cm distance from the source. Figure 4.8 exemplarily compares ultrasound pulses generated by two high-end piezoelectric ultrasound transducers and a thermophone consisting of a 30-nm-thin Titanium coating on a quartz-glass substrate after a single pulse excitation of 500 ns duration with 1.5 kV. The sound pulses were measured at a distance of 6 cm in front of the transducers.

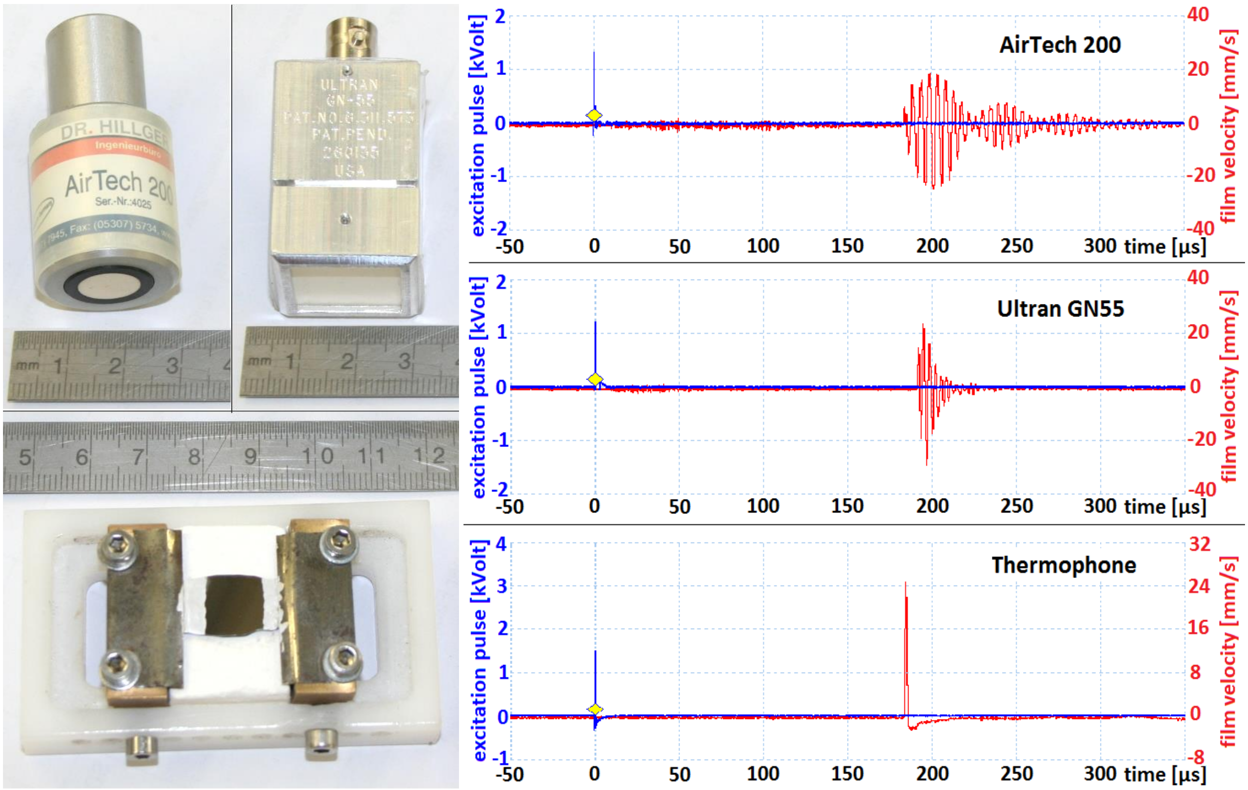

FIG. 4.8 Comparison of measured velocities of the sensing polyethylene film after excitation with (from top to bottom) AirTech 200, Ultran GN-55, and a 10 x 10 mm^2 thermophone that consists of a 30-nm-thin Titanium coating on quartz-glass substrate, placed at 60 ± 3 mm from the sensing film. All transducers were excited with 1.5 kV pulses of 500 ns duration.

As expected, the conventional piezo-electric transducers show typical resonant behavior with “long” post-oscillations after the short-pulse excitation (see Figure 4.8), while the thermophone generates a single sound pulse free from any post-oscillations.

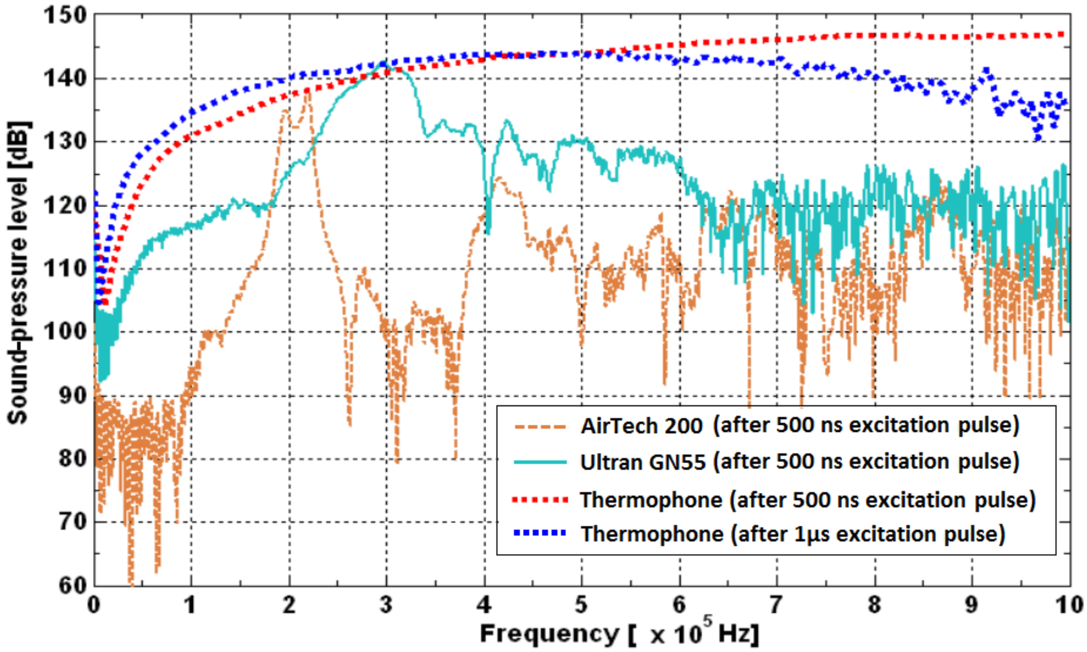

FIG. 4.9 Comparison of the generated sound-pressure levels versus frequency measured at a distance of 60 mm from the transducers after a single 1.5 kV excitation of 500 ns or 1 µs duration.

In Figure 4.9, the acoustic spectra and the sound-pressure levels at frequencies up to 1 MHz are compared for the same three transducers after a 500 ns and a 1 µs pulse excitation. The conventional piezoelectric transducers reach maximum sound pressures of about 140 dB at their center frequency after a 500 ns pulse excitation. Their acoustic spectra are relatively narrow frequency bands. After a 1 µs pulse excitation, the piezoelectric transducers generate a few dB higher sound-pressure levels, but their acoustic spectra remain unchanged and their post-ringing is longer by a factor approximately of 2. Contrary to conventional airborne-ultrasound transducers, the thermophone is a broadband device and generates sound-pressure levels of more than 140 dB for frequencies above 300 kHz after a 500 ns pulse excitation (Figure 4.9, dotted red curve). Excitation of the thermophone with longer excitation pulses, for example 1 µs pulses, halves the bandwidth of the generated acoustic signal and shifts the maximum of the generated sound-pressure levels to a lower frequency range (see Figure 4.9, dotted curve in blue). Use of e.g. 10 – 20 µs excitation pulses allows generation of low-frequency (50 – 100 kHz) airborne ultrasound.

The comparison of piezo-electric airborne-ultrasound transducers with a thermophone as shown in Figures 4.8 and 4.9 clearly demonstrates that thermophones can reach acoustical efficiencies comparable to those of conventional piezoelectric transducers and that they can be used, unlike conventional airborne-ultrasound transducers, as broadband and non-resonant ultrasound sources with a freely selectable bandwidth over the full frequency range of airborne-ultrasound applications.

The acoustic efficiency of thermophones can be further increased. Possible improvements include focusing designs, optimizing the thermophone film materials and using substrates with lower thermal effusivities. Such substrates could be porous, such as the porous-silicon substrates already proposed by Shinoda *et al.* [5] or they could be aerogels and xerogels.

Table 4.1 provides an overview of densities, specific heat capacities and hardnesses of some materials that can be used as electrically conductive nano-layers. The product of the density and the specific heat capacity yields a relative, thickness-independent value of the thermal capacitance.

As one can see in Table 4.1, carbon has a thermal capacitance smaller than metallic materials. Thus, theoretically, carbon-based materials such as graphene or carbon nanotubes are well suited to be used as thermophones. However, in practice, these materials are insufficiently robust to consistently generate sound-pressure levels of more than 140 dB due to their relatively low thermal, chemical and mechanical stabilities.

TABLE 4.1 Comparison of density, specific heat capacity, thermal capacitance and hardness at 20°C for some materials that can be used as electrically conductive films.

	Density ρ [kg/m^3]	Specific heat capacity c_p [J/kg·K]	Thermal capacitance $\rho \cdot c_p$ [MJ/m^3·K]	Hardness [Mohs]
Carbon	2200	720	1.584	1.5 – 2
ITO 90/10	7120	330	2.34	6 – 7
Titanium	4500	523	2.354	4 – 5
Aluminum	2700	897	2.422	2 – 2.8
Gold	19320	128	2.473	2.5
Tungsten	19300	138	2.66	7.5
Platinum	21450	130	2.79	3.5

For example, thermo-acoustic generation of a 1 kPa sound pressure (≈ 154 dB) at 100 kHz and at a distance of 3 cm from a 1 × 1 cm^2 thermophone requires periodic heating of the electrically conductive film up to 1000 °C (calculated from the EDF model). Carbon-based materials such as carbon nanotubes or graphene oxidize in air at temperatures above 350 °C [60] and already burn up at 560 °C. Aluminum, titanium and tungsten have better thermal stability compared to carbon materials, however, they are also prone to oxidizing in air. Therefore, thermophones consisting of these materials are not suitable for durable high sound-pressure airborne-ultrasound generation as required in NDT. Gold and platinum provide much better chemical stability in air compared to carbon-based materials, and aluminum, titanium and tungsten, but unfortunately these materials have a relatively low hardness (2.5 – 3.5 Mohs, see Table 4.1) and thus a relatively low robustness against mechanical impacts. As one can see from Table 4.1, ITO has a lower thermal capacitance than aluminum, titanium and gold. Moreover, annealed ITO has a relatively high hardness (6 – 7 Mohs), is thermally and chemically stable in air at temperatures up to 1800°C, and is already an oxide. Hence, to the best of the author’s knowledge, ITO as an electrically conductive film best meets the requirements of a thermo-acoustic airborne-ultrasound source for NDT applications in terms of its mechanical, thermal and chemical stability combined with a relatively low thermal capacitance.

The use of substrates with a small thermal effusivity will additionally increase the acoustic efficiency of a thermophone. However, one must not forget that both the hardness and the mechanical stability of a coating depend on the hardness and the stiffness of the underlying substrate. The use of porous substrates such as xerogel or aerogel necessarily results in a loss of mechanical stability and robustness of a thermophone.

In order to increase the sound pressure generated by a thermophone and, at the same time, to avoid the overheating, the surface of a thermophone has to be increased. Additionally, a focusing shape of the transducer contributes to an increase in the sound pressure.

Figure 4.10 shows photographs of a spherically shaped thermophone of 55 mm diameter, consisting of a 200-nm-thin ITO coating on a quartz-glass substrate. The copper rings provide the electrical contacts to the ITO layer. Due to its spherical shape, this thermophone has a constant acoustic focus position for all frequencies. Figure 4.10(c) exemplarily shows the calculated sound field generated by this thermophone in air at 500 kHz. Using pulse and burst excitation of 40 kWatt power, sound-pressure levels in the range of 170 dB can be achieved in the focus.

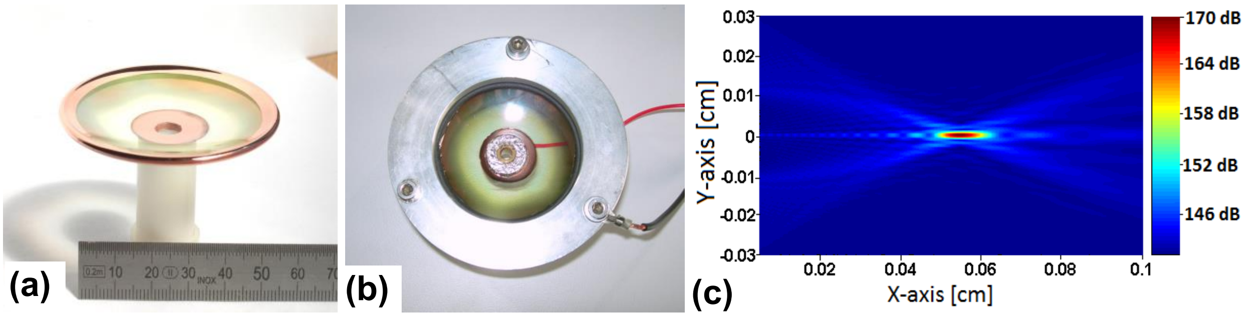

FIG. 4.10 **(a)** Focusing thermophone consisting of an annealed ITO coating on a spherically shaped quartz-glass substrate. **(b)** The same thermophone mounted in a holder. **(c)** The calculated sound field generated by the thermophone in air at 500 kHz burst excitation with 40 kW excitation power.

Additionally, as one can see in Figure 4.10(c), the “acoustic focus” generated by the focusing thermophone is relatively “sharp” compared to that generated by conventional airborne-ultrasound transducers. The reason for this behavior is that conventional airborne-ultrasound transducers generate an ultrasound wave bundle containing a frequency band of ± 20 % of the center frequency. The interference of this poly-frequent wave bundle leads to the formation of a “fuzzy” acoustic focus, which reduces the spatial resolution capability in airborne-ultrasound inspection.

Figure 4.11(a) demonstrates one of the possible applications of focusing thermophones for an airborne-ultrasound inspection of test objects. The thermophone is connected to a USPC AirTech4000 ultrasonic-inspection system and is used as a transmitter. A test carbon-fiber-reinforced plastic plate (CFRP) with several artificial defect structures is mounted on a x-y stage controlled by the inspection system.

Figure 4.11(b) shows the result of a transmission scan of the test-plate. The color scale represents the amplitude of the ultrasound signal transmitted through the plate. The orange-red colors show places of attenuated acoustic signal and thus a defect in the plate. All defects in the test plate were successfully detected.

The advantage of using a thermophone as an ultrasound source is that the frequency spectrum of the sound pulse can be optimally adapted to the main frequency of the sensing ultrasound receiver, leading to a better signal-to-noise ratio of the detected signals and thus to a higher probability of defect detection.

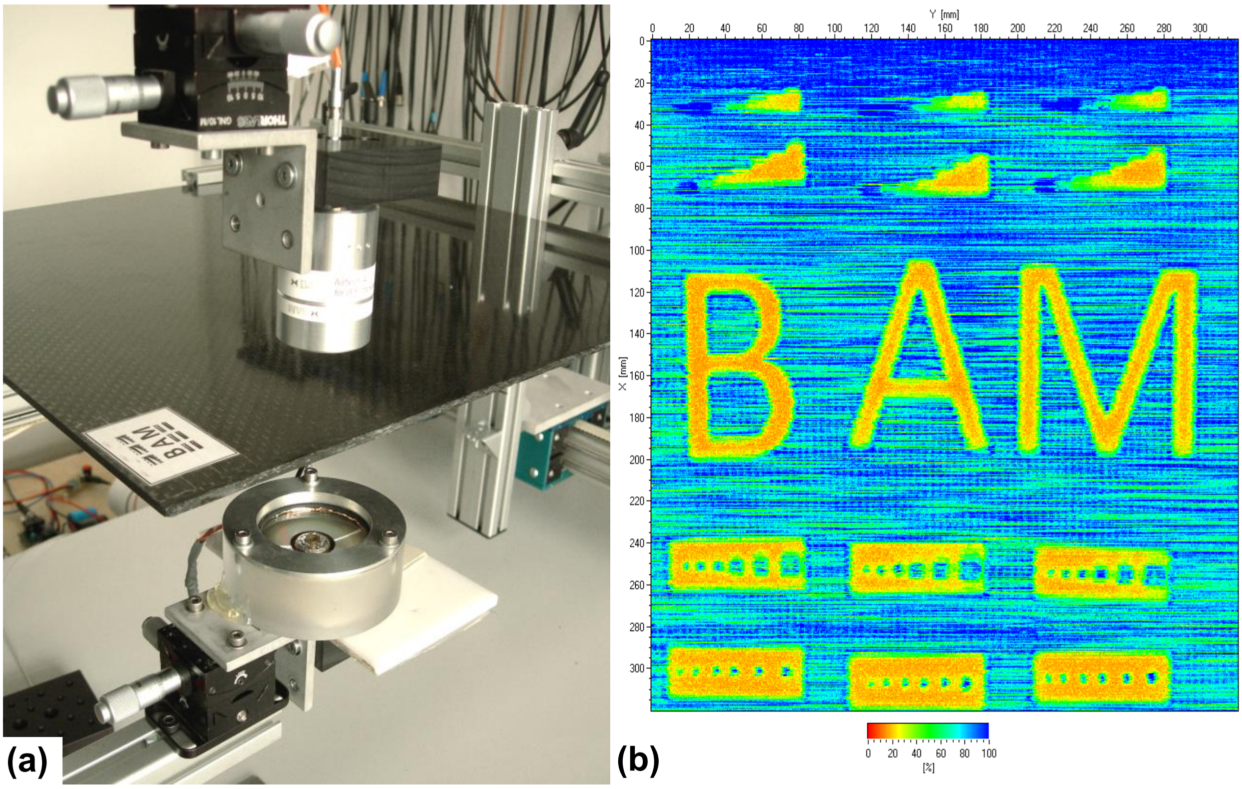

FIG. 4.11 (a) Photograph of the experimental setup. **(b)** Result of the transmission ultrasound scan of the CFRP test-plate. The color scale represents the amplitude of the ultrasound signal transmitted through the plate. The orange-red colors show positions of the attenuated acoustic signal and thus a defect in the plate.

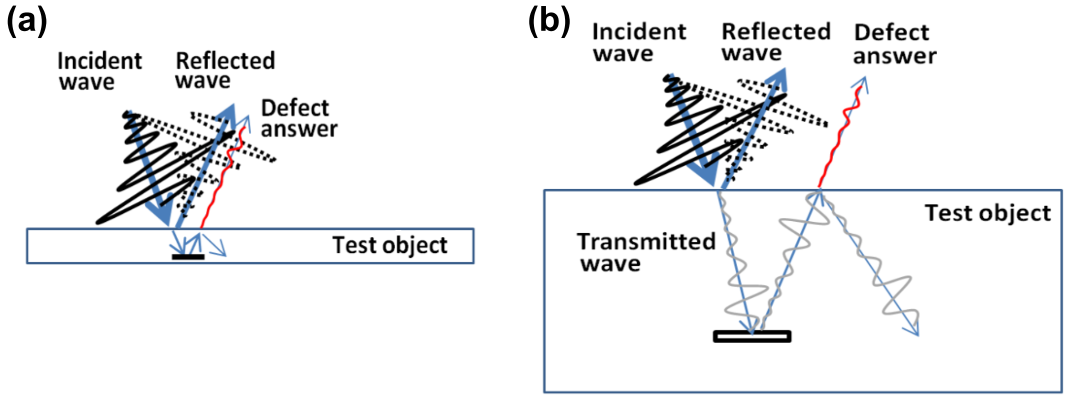

FIG. 4.12 Schematic representations of unilateral pulse-echo defect detection with conventional, post-ringing airborne-ultrasound transducers. **(a)** For a “thin” plate. **(b)** For a “thick” test body.

A further application of the thermophone could be for example in the one-sided, contact-free pulse-echo inspection and health monitoring of objects with a few centimeters of thickness. This inspection method is challenging for most of the existing airborne-ultrasound measurement systems.

Figure 4.12 illustrates the difficulties of classical unilateral airborne-ultrasound pulse-echo inspection technique. Due to a reflection of more than 99 % of the incident ultrasonic waves on the surface of the objects to be tested, the “defect response” is overlapped by the reflected waves and is generally too small for clear detection. Additionally, the reception of the “defect response” signal is disturbed during the decay time of the post-ringing of the transducer. Hence, up to now, only deep defects (far from the surface in a depth of at least 10 – 20 cm) can be detected if conventional airborne ultrasound transducers without electronically controlled active damping are used for pulse-echo inspection.

Figure 4.13 schematically shows a possible implementation of a unilateral pulse-echo inspection of thin objects with the help of a focusing thermophone as a tunable and post-oscillation-free ultrasound source and a laser-vibrometer as a ringing-free detector. The advantage of using a thermophone for pulse-echo inspection is that the test objects can be excited with single sound pulses of desired duration. Thus, using short (e.g. 500 ns – 2 μs) excitation pulses the “defect answer” from the interior of a test object can clearly be separated from the incident acoustic impulse.

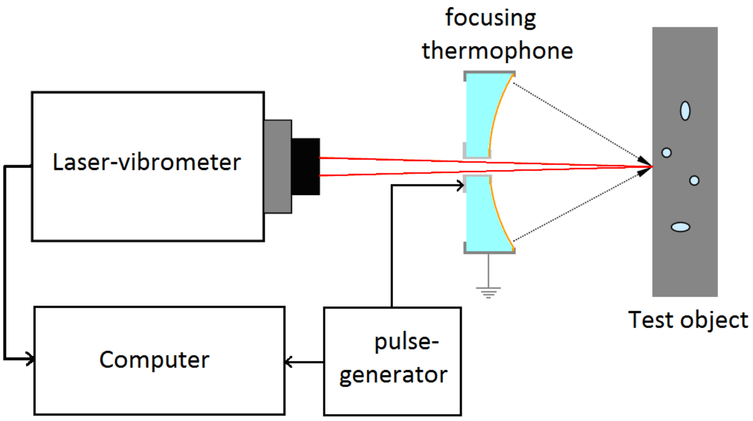

FIG. 4.13 Schematic experimental setup for unilateral pulse-echo defect detection with a focusing thermophone as a tunable airborne-ultrasound source and a Laser-Doppler-vibrometer as detector.

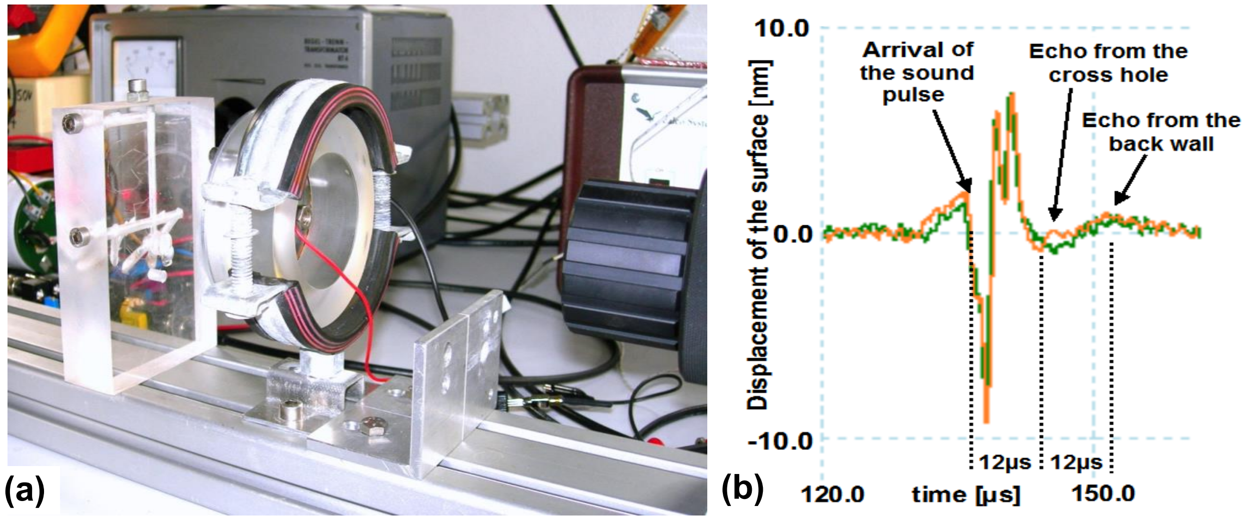

FIG. 4.14 (a) Photograph of the experimental setup for a unilateral pulse-echo inspection with a focusing thermophone as ultrasound source and a laser-vibrometer as detector. **(b)** Comparison of detected surface displacements of the Plexiglas block over time. The orange curve shows the displacement detected over a cross hole of 3 mm diameter located in 1.5 cm depth, the green curve is the displacement detected at an intact region 2 cm beside the cross hole.

The photograph shown in Figure 4.14(a) shows a unilateral airborne-ultrasound pulse-echo inspection of a Plexiglas block with a thickness of 3 cm and with a few cross holes inside as artificial defects. The focusing thermophone is positioned at a distance of 50 mm from the test object and is used as a ringing-free ultrasound source. The laser-vibrometer is focused on to the surface of the Plexiglas block and is used as a ringing-free detector. The thermophone is excited with single excitation pulses of 1.5 µs duration and 20 kW peak power. The sound-pressure level of the incident sound pulse on the surface of the Plexiglas block is between 160 and 163 dB.

Figure 4.14(b) shows the displacements of the surface of the Plexiglas block over time measured by means of the laser-vibrometer. The signals were taken above a cross hole of 3 mm diameter located in a depth of approximately 1.5 cm (orange curve) as well as at a position 2 cm beside the cross hole within an intact region (green curve). Both time signals are averaged over 256 measurements; the residual noise is in the range of ± 0.5 nm.

As one can see in Figure 4.14(b), the detected surface displacements shows a noticeable difference approximately 12 µs after the arrival of the sound pulse (compare the orange and the green curves). This difference corresponds to a reflection at a depth of approximately 13 – 14 mm inside the Plexiglas block (the speed of sound in Plexiglas is about 2360 m/s). 24 µs after the arrival of the sound pulse, both time signals show a small displacement of the surface in the range of about 2 nm. The displacements can be attributed to the return of the sound pulse reflected at the rear surface of the Plexiglas block in a depth of 3 cm.

If conventional airborne-ultrasound transducers are used, the expected displacements of the surface caused by a reflection from a 3 mm wide cross hole in a depth of 1 – 2 cm are in the range of a few nanometers. For test objects with a bigger density and a higher speed of sound, the displacement of the surface will be even smaller. Hence, the non-contact pulse-echo inspection method with airborne-ultrasound is non-trivial and requires an averaging as well as a complex post-processing of the detected time signals of the surface displacement. However, if a thermophone is used, the absence of ringing simplifies the detection of the “defect response” compared to excitations with conventional ringing airborne-ultrasound transducers.

A further highly interesting application of the thermophonic sound-generation principle in NDT is that conventional airborne-ultrasound transducers can be modified and used as a thermophone. Figure 4.15 shows, to the best of the author’s knowledge, the world’s first prototype of a hybrid airborne-ultrasound transducer. This transducer combines the advantages of thermophones and at the same time the acoustic sensitivity of a polarized cellular-polypropylene ferroelectret film (cPP-film) [61-63]. Basically, as one can see in Figure 4.15, the combined transducer is a classical airborne-ultrasound transducer; the only difference is the third contact, and the upper electrode is used for thermophonic ultrasound generation. As Figures 4.16 (a) – (d) demonstrate, the combined transducer is capable of generating arbitrarily shaped acoustic signals (sinusoidal bursts, triangular and ramp waveforms) in the full frequency range of airborne-ultrasound applications and without the typical ringing of conventional transmitting devices.

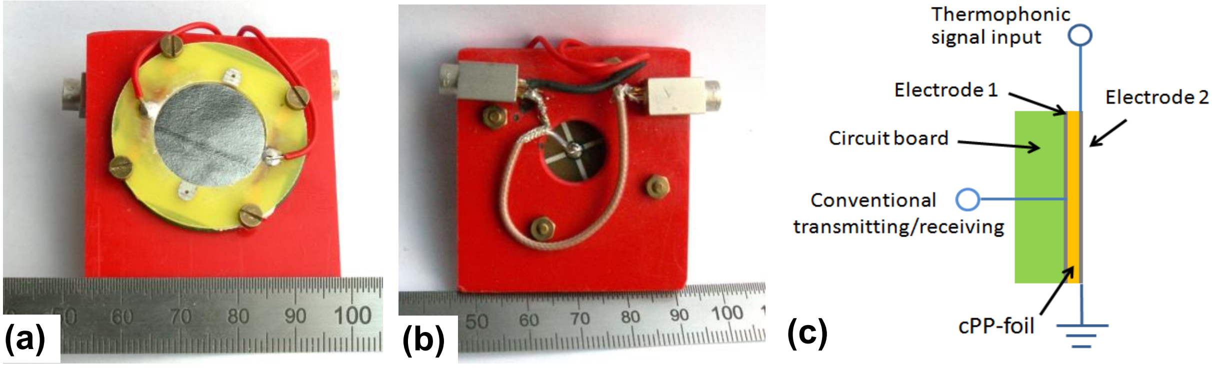

FIG. 4.15 (a) - **(b)** Photographs of the first prototype of a combined airborne-ultrasound transducer. **(c)** Schematic circuit diagram of the transducer.

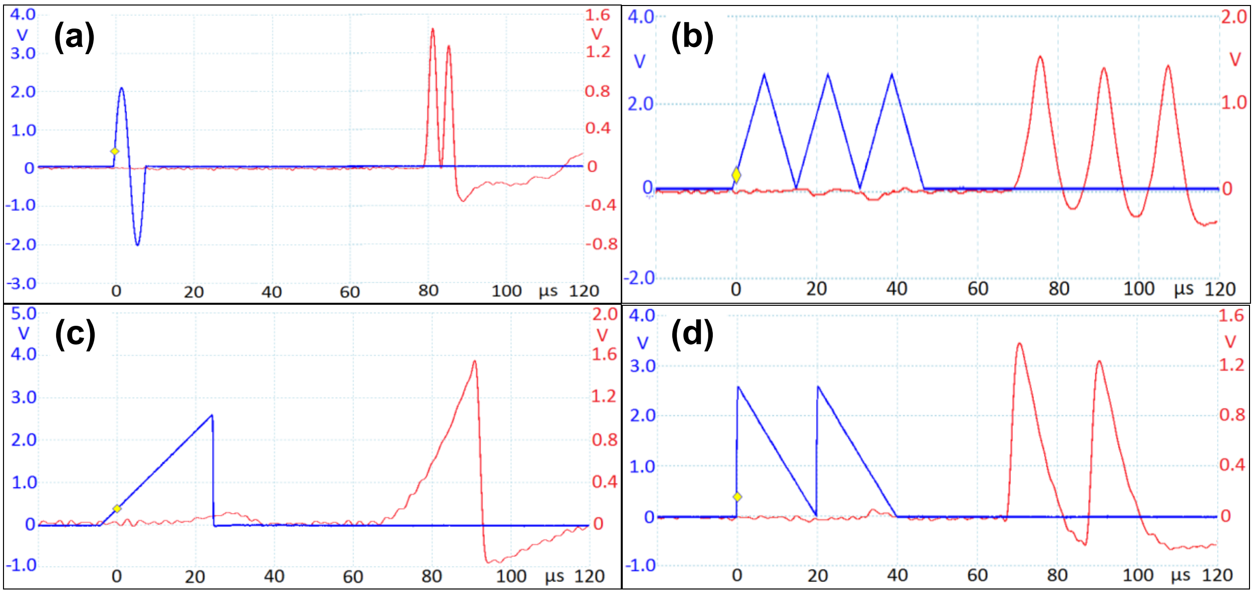

FIG. 4.16 Acoustic pulses generated in thermophonic transmission mode. **(a)** 100 kHz sinusoidal burst. **(b)** Triangles. **(c)** and **(d)** Ramps. The blue curves show the excitation voltage (1/100) and the red curves show sound pulses and waves detected with a laser-vibrometer and the polyethylene film in a distance of 2.5 - 3 cm from the transducer.

Additionally, due to the small thermal effusivity of the polypropylene film, the combined transducer shows a better electro-acoustic efficiency in thermophonic transmission mode than in classical transmission mode. For example, in classical transmission mode, excitation voltages around 2 kV are required to generate sound-pressure levels of about 145 dB at a distance of 6 cm from the transducer. In thermophonic transmission mode, excitation voltages of about 200 V generate the same sound-pressure levels at the same distance.

One of the possible applications of the novel combined airborne-ultrasound transducer is non-contact scanning of surface profiles of sensitive or porous materials that cannot be sampled with existing mechanical or optical methods. Figure 4.16 exemplarily shows a possible implementation of a unilateral airborne pulse-echo ultrasound scan of surface profiles. The transducer is connected to a USPC AirTech4000 airborne-ultrasound measurement system. Adjustments to the measurement system were not necessary. The transducer is excited with a rectangular pulse of 1 µs duration (the excitation pulse can be seen on the screen of the oscilloscope) generating single acoustic pulses in thermophonic transmission mode. Reception of the acoustic pulses after reflection off the plate surface is possible in a conventional manner with cPP-film. The time-signal received by the transducer and its Fourier transform can be vaguely seen on the monitor in the background. From the time delay of the returned acoustic pulse, the surface profile can be reconstructed with high accuracy. For example, if short (100 – 200 ns) acoustic pulses are used, changes of the surface profile on the order of a few tens of µm can be detected. Note that, due to high sound attenuation in air (especially for ultrasound pulses of 100 – 200 ns duration), the distance between the transducer and the test object should no more than 10 – 20 mm. The use of focusing transducers will additionally increase the spatial resolution of detection.

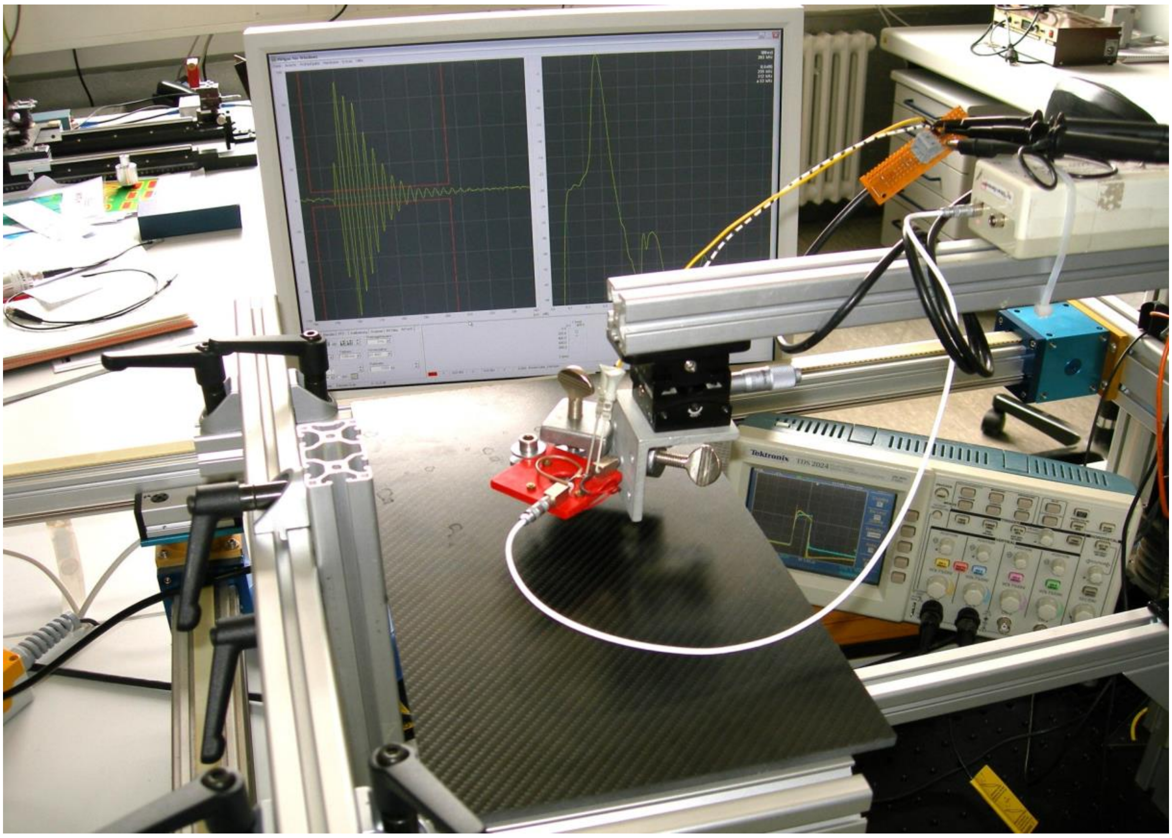

FIG. 4.16 Experimental setup for unilateral airborne pulse-echo ultrasound scans of surface profiles.

In summary, the use of thermophones in NDT is a new scientific field. The applications proposed and the experiments demonstrated here are not yet optimized and only provide experimental examples for some possible applications of thermophones in NDT.

Further possible applications of thermophones in NDT could be for example the modal analysis of test objects after broadband pulse excitation. Additionally, using for example monofrequent burst excitation, Lamb waves of desired frequency and wave-length can be excited in plates and thin-walled pipes.

Advantages of thermophones over conventional airborne-ultrasound transducers are broadband and resonance-free behavior, simple construction, and low production costs. Due to their simple construction, thermophones of nearly arbitrary size and shape can be fabricated. Moreover, arbitrarily shaped acoustic signals without disruptive resonances or ringing can be generated with thermophones in the full frequency range of airborne-ultrasound applications. Furthermore, with tungsten, nickel-chromium or platinum coatings, highly robust thermophones can be designed for applications in chemically aggressive media (like acids and bases) and at high temperatures and even inside plasmas.

5. Summary

A thermophone is an electrical device for sound generation. The advantages of thermophones over conventional sound transducers such as electro-magnetic, electrostatic or piezo-electric transducers are that they are free of moving parts, have no resonances, and offer simple construction and low production costs. Furthermore, arbitrarily shaped acoustic signals can be generated with a thermophone. Thus, thermophones have the potential for a wide use in applied acoustics as powerful and resonance-free sound sources with a bandwidth in the MHz range and beyond.

The evaluation of the existing theoretical concepts and approaches for thermophonic sound generation in gases has shown that there is currently no model available which would be able to predict the sound pressure generated with thermophones at a sufficient accuracy.

Hence, the present PhD thesis focuses on a detailed theoretical analysis, mathematic modeling and experimental investigation of thermophonic sound generation in real gases.

Based on the consideration of an acoustic wave as a thermally induced kinetic Energy-Density-Function (EDF model) and on its propagation in the adjacent gas, a generalized mathematical description of thermophonic sound generation in real gases was derived. With the energy-based consideration, the difficulties that are usually encountered in the analytical solution of a set of coupled partial differential equations for temperature and pressure are avoided, and a fully analytical solution for the thermally generated sound pressure at each point of the surrounding real gas is obtained. From a theoretical point of view, the proposed EDF model is generalized and can be applied to arbitrary thermal-power sources including thermophones, plasma discharges, laser beams, chemical or nuclear reactions. The non-linear effects such as shock waves and hypersonic wave propagations caused e.g. by explosions are not included and have to be treated differently.

Unlike the existing theoretical approaches [2,5,6,8-11,15-17] (see Section 1.2) for modeling thermophonic sound generation in gases, the EDF model describes free-standing as well as substrate-based thermophones and comprises:

- the thermodynamic properties of thermophone materials, including the thermal inertia of the heat-producing film and the thermal effusivities of the substrate and the adjacent gas,
- the physical properties of adjacent real gas atoms and molecules such as molecular degrees of freedom and the volume occupied by the gas atoms,
- the distance- and frequency-dependent sound-attenuation effects due to viscosity, inelastic collisions and excitation of vibronic states of real gas molecules,
- the shape and size of the thermophone surface, and also
- the reduction of the acoustic power due to photon emission.

Thus, the EDF model is applicable to a wide range of thermophonic applications in real gases. For more complex cases, such as thermal sound generation in gases near their condensation points or near their critical points, the EDF model may require further modifications.

For experimental validation of the EDF model, several free-standing and substrate-based thermophone samples of different sizes, shapes and materials were tested for sound generation in gases in a frequency range from 2 kHz to 1 MHz. The experimentally investigated frequency range is 10 – 20 times wider than in all the experimental studies on thermophones published so far. It can be assumed that thermophones are also capable to produce ultrasound at frequencies higher than 1 MHz. However, the frequency range in this study was limited to 1 MHz due to increasing noise levels of the measuring equipment.

To measure thermally generated sound pressures in different gases, a Laser-Doppler-Vibrometer combined with a 12-µm-thin polyethylene foil placed in the sound field was used as a broadband and non-resonant microphone. The method allows for measurements of particle velocity and sound pressure in all optically transparent gases with known density and speed of sound. Advantages of the measurement method in comparison to conventional sound-pressure receivers such as condenser microphones or piezo-electric transducers are:

- no calibration is required;
- a large dynamic measuring range (from µPA to MPa) and a large bandwidth (from a few Hz to a few MHz);
- suitability for precise measurements in any light-transparent gases; and
- resonance-free frequency response.

The tested thermophones samples pool included free-standing carbon-nano-wire webs (CNWs) of different thickness (5 – 150 µm), size and shape and different substrate-based thermophones consisting of titanium and Indium-Tin-Oxide (ITO) coatings of different thickness (20 – 2500 nm), size and shape on polycarbonate and quartz-glass substrates. Altogether, more than fifty different thermophone samples were tested for sound generation. The main reason to use quartz-glass and polycarbonate as substrates in the experimental study is because the density, heat conductivity and thermal capacity of these materials are well known. Additionally, the substrates have a smooth surface with a roughness smaller than 2 nm. Thus, the Titanium and ITO coatings used as electrically conductive films can be assumed to be homogeneous layers of a constant thickness.

Unlike all existing models (see Section 1.2) describing thermophonic sound generation in gases, only the EDF model is general and can be applied to predict the sound pressure generated by free-standing as well as by substrate-based thermophones with an accuracy of ± 4 – 15 %. This is by a factor of 25 to 100 better than the prediction accuracy of the earlier models.

The prediction accuracy of the EDF model mainly depends on the precision of the thermodynamical and physical parameters of gases, substrates and electrically conductive films. The main parameters affecting the prediction accuracy are: the speed of sound in the gas, the ratio of the thermal effusivities of the substrate and the surrounding gas, the input power, the number of the degrees of freedom of the gas molecules, the heat capacity of the electrically conductive films and the sound attenuation in gas.

In order to experimentally validate the EDF model in various gases, the sound pressure generated by a substrate-based thermophone consisting of a 50-nm-thin ITO coating on a quartz-glass substrate was measured in gases such as He, Ar, O_2, N_2, air and SF_6 in a frequency range from 5 kHz to 1 MHz. The maximum deviation between the measured and the model-predicted sound pressures was in the range of ± 4 % for all gases.

For all free-standing thermophone samples tested in “open” air, maximum deviations of ± 15 % were observed between the measured and the model-predicted sound-pressure levels. The reasons for the relatively large deviations are inhomogeneities of the CNW samples and rather imprecise estimates for the sample thickness, density and heat capacity.

For all substrate-based thermophones tested in “open” air, deviations of less than ± 10 % have been observed between measured and the model-predicted sound-pressure levels. The reasons for the deviations are: deviations of the film thickness, weather-dependent variations of air humidity, room temperature and pressure, and an uncertainty of about 1.5 – 2 % for the supplied electrical-power amplitude.

All tested thermophone samples showed a resonance-free frequency response in the entire tested frequency range. Thus, thermophones can be used as broadband and non-resonant ultrasound sources.

As predicted from the EDF model, the thermally generated sound pressure is linearly related to the input power and the excitation frequency. An initially linear increase of the sound pressure with increasing excitation frequency is suppressed by the frequency-dependent thermal inertia of the heat-producing film and by an exponential increase of the sound attenuation in the gas. Thus, the EDF model may be used to explain the experimental findings of all previous publications in which it was reported that the generated sound pressure $p(f)$ is proportional either to f, or to $f^{0.7-0.8}$ or to $f^{0.5}$.

Unlike the prediction made in the models of Shinoda *et al.* [5], Boullosa *et al.* [6], Tian *et al.* [11], Vesterinen *et al.* [15] and Hu *et al.* [16] (which do not comprise the thermodynamic properties of the heat-producing film), the experimental results for substrate-based thermophones confirmed the prediction made from the EDF model and showed that the thermal inertia of an electrically conductive film has a negative influence on the acoustic efficiency of substrate-based thermophones and should not be neglected.

The best possible acoustic performance of a thermophone on a substrate can be achieved by using:

a) an electrically conductive film with the smallest possible thickness d_{film}, density ρ_{film} and specific heat capacity $c_{p\,film}$;

b) a substrate with the smallest possible thermal effusivity e_{sub}.

The condition (a) confirms the findings of Arnold and Crandall [2] and of Xiao et al. [8,9] made for free-standing thermophones, and condition (b) confirms the findings of Shinoda [5], Boullosa [6], Tian et al. [11] and Hu et al. [16] made for substrate-based thermophones.

In addition to the development and the experimental evaluation of the generalized EDF model for thermophonic sound generation in real gases, new applications of thermophones such as:

- investigation of physical properties of gases,
- thermo-acoustic gas spectroscopy,
- broadband characterization of transfer functions of sound and ultrasound detection systems, and
- non-destructive materials testing

have been discussed and experimentally demonstrated. Furthermore, thermophones could also be used as sensing devices such as temperature sensors, pressure sensors, and gas-flow sensors similar to hot-wire and hot-film anemometry. Thus, thermophones could be a new versatile scientific tool with the potential for wider use in various areas of applied science.

APPENDIX A: Determination of thermodynamic equilibrium temperature $T_{Therm\ eq}$

Let us consider a thermophone consisting of an electrically conductive film on a solid substrate being heated with a continuous sinusoidal power $P_{el\ eff}$. The part of the thermal power flowing into the adjacent gas $P_{gas}\cdot(3/F_{DoFs})$ generates sound waves and is carried away with the speed of sound. The thermal power flowing into substrate P_{sub}, in addition to the power P_{film} remaining in the film itself, quasi-constantly heat the substrate and its immediate surroundings. This DC heat will be removed by photon emission $P_{photons}$ and convection $P_{convection}$ (the heat conductivity of a gas is mostly small (e.g. λ_{air} = 0.024) and can be neglected).

Therefore, to determine the equilibrium temperature of a thermophone, the effective value of the thermal power that flows into the substrate P_{sub}, the thermal power remaining in the film P_{film} and the thermal power remaining in the adjacent gas layer as rotations and vibrations of the molecule $P_{gas}\cdot((F_{DoFs} - 3)/F_{DoFs})$ have to be taken into account:

$$P_{sub} + P_{film} + P_{gas} \cdot \frac{F_{DoFs} - 3}{F_{DoFs}} = P_{convection} + P_{photons} \tag{A1}$$

$$P_{gas}(T,P) = P_{el\ eff} \cdot E_{gas}(T,P,f_{th}) \tag{A2}$$

$$P_{sub}(T,P) + P_{film}(T,P) = P_{el\ eff} \cdot \left(1 - E_{gas}(T,P,f_{th})\right) \tag{A3}$$

where F_{DoFs} is the amount of degrees of freedom of adjacent gas molecules (see Equation (2.36)), $E_{gas}(T,P,f_{th})$ is the energy distribution function (see Equation (2.21)) at given gas temperature T and pressure P.

To calculate the power transported by convection and photons following, well known equations can be used:

$$P_{convection}(T,P) = h_{conv}(T,P) \cdot S_{Therm} \cdot \left(T_{Therm} - T_{0\,gas}\right), \tag{A4}$$

$$P_{photons} = \varepsilon \cdot \sigma \cdot S_{Therm} \cdot \left(T_{Therm}^4 - T_{0\,gas}^4\right), \tag{A5}$$

where $h_{conv}(T,P)$ is the convection coefficient of a gas at given temperature T and pressure P, S_{Therm} is the total area of the thermophone, ε is the emissivity of the thermophone material, $\sigma = 5.670373(21)\cdot 10^{-8}\ \mathrm{W\cdot m^{-2}\cdot K^{-4}}$ is the Stefan–Boltzmann constant and $T_{0\,gas}$ is the temperature of surrounding gas).

Inserting the Equations (A2) – (A5) in Equation (A1) for power balance results in

$$P_{el\ eff} \cdot \left(1 - E_{gas}(T,P,f_{th}) \cdot \left(1 - \frac{F_{DoFs} - 3}{F_{DoFs}}\right)\right) = h_{conv} \cdot S_{Therm} \cdot \left(T_{Therm} - T_{gas}\right) + \varepsilon \cdot \sigma \cdot S_{Therm} \cdot \left(T_{Therm}^4 - T_{gas}^4\right). \tag{A6}$$

Solving of Equation (A6) for T_{Therm} yields the thermodynamic equilibrium temperature of the thermophone.

For example, consider a flat glass-substrate body with a total area of 2 cm^2 and emissivity ε = 0.95 in static air at room temperature (293.15 K, 20 °C) being heated with a continuous sinusoidal power of 1 W. Assuming the convection constant of static air $h_{conv\ air}$ = 20 (EN ISO 6946 norm Appendix A), in a few minutes the thermophone will reach its equilibrium temperature T_{Therm} of about 457.5 K (184.4 °C).

APPENDIX B: Determination of the energy $Q_{photons}$ transported by photons

Consider for example a 50-nm-thin titanium film covering 1 cm^2 on a quartz-glass being excited for t_{th} = 100 µs (10 kHz) with 100 W effective power, $Q_{th\ in} = P_{el\ in} \cdot t_{th} = 1 \cdot 10^{-2}$ J. Using thermal diffusion $a = \lambda/(\rho \cdot c_p)$, the heat penetration depth $d_{th} = (a \cdot t_{th}/2 \cdot \pi)^{1/2}$ and the density ρ one can determine the mass of the heated gas and the substrate layers during one heating period t_{th}: $m_{sub} = d_{th\ sub} \cdot \rho_{sub} \cdot S_{film}$, $m_{gas} = d_{th\ gas} \cdot \rho_{gas} \cdot S_{film}$.

The maximum temperature rise of the electrically conductive film above the initial room temperature (e.g. $T_0 = 293.15$ K) will be $\Delta T_{th\ film} = Q_{th\ in}/(c_{p\ film} \cdot m_{film} + c_{p\ sub} \cdot m_{sub} + c_{v\ gas} \cdot m_{gas}) = 6.9$ K.

The maximum of both sides, from the periodically heated film, transported energy by photons during 100 µs, will be

$Q_{photons\ th}\ (t_{th} = 100 \mu s) = P_{photons} \cdot t_{th} = \varepsilon \cdot \sigma \cdot S_{film} \cdot ((\Delta T_{th\ film} + T_0)^4 - T_0^4) \cdot t_{th} = 4.2 \cdot 10^{-7}$ J,

where $\varepsilon = 0.5$ is the emissivity of the transducer material, $\sigma = 5.670373(21) \cdot 10^{-8}$ W·m^{-2}·K^{-4} is the Stefan–Boltzmann constant, and $S_{film} = 2 \times 1$ cm^2 is the total film surface. This represents 0.0042% of the total input energy $Q_{th\ in}$. For 10 µs (100 kHz) excitation with 100 W effective power, the maximum energy transported by photons $Q_{photons\ th}$ is only 0.0013%, and for 1 µs (1 MHz) excitation $Q_{photons\ th}$ is only 0.001% of the input energy $Q_{th\ in}$. Therefore, the photonic part $Q_{photons\ th}$ can be mostly neglected.

Note, that for free-hanging films and low-frequency excitations (< 10 kHz) the part of the thermal energy converted into photonic radiation can reach up to few percent of the supplied thermal energy $Q_{th\ in}$ and hence has to be taken into account.

For example, consider a free-hanging 50-nm-thin titanium film of 2 cm^2 surface area in air being excited for t_{th} = 100 µs (10 kHz) with 100 W effective power, $Q_{th\ in} = P_{el\ in} \cdot t_{th} = 1 \cdot 10^{-2}$ J. The maximum temperature rise of the electrically conductive film above the initial room temperature ($T_0 = 293.15$ K) will be $\Delta T_{th\ film} = Q_{th\ in} / (c_{p\ film} \cdot m_{film} + 2 \cdot c_{v\ gas} \cdot m_{gas}) = 509$ K. The maximum of both sides, from the periodically heated film, transported energy by photons during 100 µs, will be $2.28 \cdot 10^{-4}$ J. This represents 2.28% of the total input energy $Q_{th\ in}$. For 10 µs (100 kHz) excitation with 100 W effective power, the maximum energy transported by photons $Q_{photons\ th}$ is only 0.058%, and for 1 µs (1 MHz) excitation $Q_{photons\ th}$ is only 0.0048% of the input energy $Q_{th\ in}$.

Bibliography

[1] P. de Lange, "On Thermophones", Proceedings of the Royal Society of London Vol. 91, No. 628 (Apr. 1, 1915), p. 239 – 241.

[2] H. D. Arnold and I. B. Crandall, "The thermophone as a precision source of sound", Phys. Rev., Vol. X, No.1, 1917, p. 22 – 38, http://dx.doi.org/10.1103/PhysRev.10.22.

[3] E. C. Wente, "The thermophone", Phys. Rev., Vol. XIX, No.4, 1922, p. 333 – 345.

[4] W. Geffcken and L. Keibs, "Untersuchungen über akustische Schwellenwerte. II. Das Thermophon und seine Verwendung als akustisches Meßinstrument", Annalen der Physik, Band 16,1933, p. 404 – 430.

[5] H. Shinoda, T. Nakajima, K. Ueno and N. Koshida, "Thermally induced ultrasonic emission from porous silicon", Letters to Nature, Vol. 400, 1999, p. 853 – 855.

[6] R. R. Boullosa, A. O. Santillan, "Ultrasound radiation from simple thermoacoustic transducer", Acta Acustica united with Acustica, Vol. 90, 2004, p. 277 – 284.

[7] I. Hwang, Y. Kim, "Measurement of thermoacoustic waves induced by rapid heating of nickel sheet in open and confined spaces", International Journal of Heat and Mass Transfer 49 (2006), p. 575 – 581.

[8] L. Xiao, Z. Chen, C. Feng, L. Liu, Z. Bai, Y. Wang, L. Qian, Y. Zhang, Q. Li, K. Jiang and S. Fan, "Flexible, Stretchable, Transparent Carbon Nanotube Thin Film Loudspeakers", Nano Letters, Vol. 8, No. 12, 2008, p. 4539 – 4545, http://dx.doi.org/10.1021/nl802750z.

[9] L. Xiao, P. Liu, L. Liu, Q. Li, Z. Feng, S. Fan and K. Jiang, "High frequency response of carbon nanotube thin film speaker in gases", Journal of Applied Physics 110, 084311 (2011), http://dx.doi.org/10.1063/1.3651374.

[10] A. O. Niskanen, J. Hassel, M. Tikander, P. Maijala, L. Grönberg and P. Helisto, "Suspended metal wire array as a thermoacoustic sound source", Appl. Phys. Lett. 95, 2009, http://dx.doi.org/10.1063/1.3249770.

[11] H. Tian, T. Ren, D. Xie, Y. Wang, C. Zhou, T. Feng, D. Fu, Y. Yang, P. Peng, L. Wang, and L. Liu, "Graphene-on-paper sound source devices", ACS Nano, Vol. 5, No. 6, 2011, p. 4878 – 4885.

[12] H. Tian, D. Xie, Y. Yang, T. Ren, Y. Wang, C. Zhou, P. Peng, L. Wang and L. Liu, "Transparent, flexible, ultrathin sound source devices using Indium Tin oxide films", Appl. Phys. Lett. 99, 043503 (2011), http://dx.doi.org/10.1063/1.3617462.

[13] Y. Wei, X. Lin, K. Jiang, P. Liu, Q. Li, and S. Fan, "Thermoacoustic chips with carbon nanotube thin yarn arrays", Nano Lett. 13 (2013), p. 4795 – 4801, http://dx.doi.org/10.1021/nl402408j.

[14] F. A. McDonald and G. C. Wetsel, "Generalized theory of the photoacoustic effect", J. Appl. Phys., Vol. 49, No. 4, 1978, p. 2313 – 2322.

[15] V. Vesterinen, A. O Niskanen, J. Hassel and P. Helistö, "Fundamental Efficiency of Nanothermophones: Modeling and Experiments", Nano Lett. 2010, 10, p. 5020 – 5024, http://dx.doi.org/10.1021/nl1031869.

[16] H. Hu, T. Zhu and J. Xu, “Model for thermoacoustic emission from solids”, Appl. Phys. Lett. 96 (2010), http://dx.doi.org/10.1063/1.3435429.

[17] A. E. Aliev, Y. N. Gartstein and R. H. Baughman, “Increasing the efficiency of thermoacoustic carbon nanotubes sound projectors”, IOP Publishing, Nanotechnology 24 (2013), http://dx.doi.org/10.1088/0957-4484/24/23/235501.

[18] R. Dutta, B. Albee, W. E. van der Veer, T. Harville, K. C. Donovan, D. Papamoschou, and R. M. Penner, “Gold Nanowire Thermophones”, J. Phys. Chem. C 2014, 118, p. 29101 – 29107, http://dx.doi.org/10.1021/jp504195v.

[19] L. Cremer and M. Möser, “Technische Akustik” (5th Edn.), Springer-Verlag, ISBN 3-540-44249-9, p.262 – 269.

[20] H.D. Young and R. Geller, “Young and Geller College Physics” (8th ed.), published 2006 by Pearson, ISBN 0-8053-9218-1.

[21] P. M. Morse and K. U. Ingard, “Theoretical Acoustics”, Published by Princeton University Press (1992), ISBN: 9780691024011, p.271 – 300.

[22] A. D. Pierce, “Acoustics: An Introduction to Its Physical Principles and Applications”, Publisher: Acoustical Society of America (1989), ISBN-13: 978-0883186121.

[23] M. Daschewski, R. Boehm, J. Prager, M. Kreutzbruck and A. Harrer, “Physics of thermo-acoustic sound generation”, J. Appl. Phys. 114, 114903 (2013), http://dx.doi.org/10.1063/1.482112.

[24] C. H. M. Jenkins, U. A. Korde, “Membrane vibration experiments: An historical review and recent results”, Journal of Sound and Vibration 295 (2006), p. 602-613, http://dx.doi.org/10.1016/j.jsv.2006.01.036.

[25] Q. Leclère and B. Laulagnet, “Particle velocity field measurement using an ultra-light Membrane”, Applied Acoustics 69, 2008, p. 302 – 310, http://dx.doi.org/10.1016/j.apacoust.2006.11.009.

[26] M. Daschewski, M. Kreutzbruck, J. Prager, E. Dohse, M. Gaal, and A. Harrer, “Resonance-free measuring and excitation of ultrasound”, TM - Technisches Messen 2015, 82(3), p. 156 – 166, http://dx.doi.org/10.1515/teme-2014-0020.

[27] http://optics.heraeus-quarzglas.com/media/webmedia_local/downloads/ FusedsilicaandQuartzGlassforOpticsDataandProperties.pdf

[28] A. Faghri, Y. Zhang and J. R. Howell, Advanced Heat and Mass Transfer, Global Digital Press, 2010, ISBN: 9780984276004.

[29] https://www.thermalfluidscentral.org/encyclopedia/index.php/Thermophysical_Properties:_ Gas_and_Liquids_at_Atmospheric_Pressure

[30] http://www.pipeflowcalculations.com/tables/gas.php

[31] http://www.engineersedge.com/heat_transfer/thermal-conductivity-gases.htm

[32] “VDI-Wärmeatlas”, 11.ed., Springer-Verlag, ISBN: 978-3-642-19980-6, p. 196 – 287.

[33] H. Petersen, “The Properties of Helium: Density, Specific Heats, Viscosity, and Thermal Conductivity at Pressures from 1 to 100 bar and from Room Temperature to about 1800 K”, Danish Atomic Energy Commission, Risö Report No.224 (1970).

[34] http://www.engineeringtoolbox.com/dry-air-properties-d_973.html

[35] E. A. Mason and J. Kestin, "Thermal Conductivity of Nine Polyatomic Gases at low Density", J. Phys. Ref. Data, Vol. 19, No. 5 (1990), p. 1123 – 1136.

[36] S. H. P. Chen and S. C. Saxena, "Thermal conductivity of argon in the temperature range 350 to 2500 K", Molecular Physics, Vol. 29, No. 2 (1975), p. 455 – 466.

[37] M. C. Aggarwal and G. S. Springer, "High temperature – high pressure thermal conductivity of argon", J. Chem. Phys. 70, No. 8 (1979), p. 3939 – 3947.

[38] M. J. Assael I. A. Koini, K. D. Antoniadis, M. L. Huber, I. M. Abdulagatov, and R. A. Perkins, "Reference Correlation of the Thermal Conductivity of Sulfur Hexafluoride from the Triple Point to 1000 K and up to 150 MPa", J. Phys. Ref. Data 41, 023104 (2012), http://dx.doi.org/10.1063/1.4708620.

[39] J. J. Hurly, D. R. Defibaugh, M. R. Moldover, "Thermodynamic Properties of Sulfur Hexafluoride", International Journal of Thermophysics, 2000, Vol. 21, Issue 3, p. 739 – 765.

[40] C. Guder and W. Wagner, "A Reference Equation of State for the Thermodynamic Properties of Sulfur Hexafluoride (SF6) for Temperatures from Melting Line to 625 K and Pressures up to 150 MPa", J. Phys. Ref. Data, Vol. 38, No. 1 (2009), http://dx.doi.org/10.1063/1.3037344.

[41] E. Medvedovski, N. Alvarez, O. Yankov, M. K. Olsson, "Advanced indium-tin oxide ceramics for sputtering targets", Ceramics International 34 (2008), p. 1173 – 1182, http://dx.doi.org/10.1016/j.ceramint.2007.02.015.

[42] R. C. Weast, "Handbook of Chemistry and Physics" (53rd Edn.), Cleveland: Chemical Rubber Co., 1972.

[43] E. W. Lemmon, R.T. Jacobsen, "Viscosity and Thermal Conductivity Equations for Nitrogen, Oxygen, Argon, and Air", International Journal of Thermophysics, Vol. 25, No.1(2004), p. 21 – 69.

[44] S. E. Quinones-Cisneros, M. L. Huber, U. K. Deiters, "Correlation for the Viscosity of Sulfur Hexafluoride (SF6) from the Triple Point to 1000 K and Pressures to 50 MPa", Journal of Physical and Chemical Reference Data 41, 023102 (2012), http://dx.doi.org/10.1063/1.3702441.

[45] J. J. Hurly, K. A. Gillis, J. B. Mehl, and M. R. Moldover, "The Viscosity of Seven Gases Measured with a Greenspan Viscometer", International Journal of Thermophysics, Vol. 24, No. 6 (2003), p. 1441 – 1474.

[46] B. A. Younglove and H. J. M. Hanley, "The Viscosity and Thermal Conductivity Coefficients of Gaseous and Liquid Argon", J. Phys. Chem. Ref. Data, Vol. 15, No. 4(1986), p. 1323 – 1337.

[47] G. Emanuel, "Bulk viscosity of dilute polyatomic gas", Physic of Fluids A 2(12), 1990, p. 2252 – 2254.

[48] X. Pan, M. N. Shneider Z. Zhang, and R. B. Miles, "Bulk Viscosity Measurements Using Coherent Rayleigh-Brillouin Scattering", The 42nd Aerospace Sciences Meeting and Exhibit Conference 2004.

[49] Z. Gu, W. Ubachs, "A systematic study of Rayleigh-Brillouin scattering in air, N_2, and O_2 gases", J. Chem. Phys. 141, 104320 (2014), http://dx.doi.org/10.1063/1.4895130.

[50] M. S. Cramer, “Numerical estimates for the bulk viscosity of ideal gas”, Physic of Fluids 24, 066102 (2012), http://dx.doi.org/10.1063/1.4729611.

[51] C.S. Sunandana, “Physical Applications of Photoacoustic Spectroscopy”, Physica Status Solidi (a), Volume 105, 1988, p. 11 – 43, http://dx.doi.org/10.1002/pssa.2211050102

[52] F. J.M. Harren, G. Cotti, J. Oomens and S. L. Hekkert, “Photoacoustic Spectroscopy in Trace Gas Monitoring”, Encyclopedia of Analytical Chemistry, R.A. Meyers (Ed.) 2000, p. 2203 – 2226.

[53] N. Bouaoua, “Free-field reciprocity calibration of condenser microphones in the low ultrasonic frequency range”, PhD thesis (2008), University of Oldenburg, http://oops.uni-oldenburg.de/id/eprint/725.

[54] J. Blitz, G. Simpson, “Ultrasonic Methods of Non-destructive Testing”, Springer Netherlands 1995, ISBN: 978-0-412-60470-6.

[55] D. A. Benwell, “A Review of Ultrasound Application”, Journal of the Canadian Acoustical Association, Volume 8, No 2 (1980).

[56] L. C. Lynnworth, “Ultrasonic Measurements for Process Control: Theory, Techniques, Applications”, Academic Press (2013), ISBN*:* 978-0-323-13803-1.

[57] C. J. Lissenden and J. L. Rose, “Structural Health Monitoring of Composite Laminates Through Ultrasonic Guided Wave Beam Forming”, NATO Applied Vehilce Technology Symposium on Military Platform Ensured Availability Proceedings. 2008.

[58] M. Kreutzbruck, M. Pelkner, M. Gaal, M. Daschewski, and D. Brackrock, “Evolution of Modern NDT-Methods for the Inspection of Lightweight Components”, The 12th International Conference of the Slovenian Society for Non-Destructive Testing (2013), Conf. Proceeding, p. 304 – 314.

[59] D. E. Chimenti, “Review of air-coupled ultrasonic materials characterization”, Ultrasonics 54(7), (2014), p.1804 – 1816, http://dx.doi.org/10.1016/j.ultras.2014.02.006.

[60] Y. Yamada, K. Murota, R. Fujita, J. Kim, A. Watanabe, M. Nakamura, S. Sato, K. Hata, P. Ercius, J. Ciston, C. Yu Song, K. Kim, W. Regan, W. Gannett, and A. Zettl, “Subnanometer vacancy defects introduced on graphene by oxygen gas”, Journal of American Chemical Society 136 (6) (2014), p. 2232 – 2235. http://dx.doi.org/10.1021/ja4117268.

[61] S. Bauer, R. Gerhard-Multhaupt, and G. M. Sessler, “Ferroelectrets: Soft Electroactive Foams for Transducers”, Physics Today 57(2) (2004), p. 37 – 43.

[62] M. Wegener and S. Bauer, “Microstorms in Cellular Polymers: A Route to Soft Piezoelectric Transducer Materials with Engineered Macroscopic Dipoles”, ChemPhysChem 2005, Volume 6, Issue 6, p. 1014 – 1025, http://dx.doi.org/10.1002/cphc.200400517.

[63] V. Bovtun, J. Döring 1, J. Bartusch, U. Beck, A. Erhard, Y. Yakymenko, “Ferroelectret non-contact ultrasonic transducers”, Appl. Phys. A 88 (2007), p. 737 – 743, http://dx.doi.org/10.1007/s00339-007-4060-3.

Acknowledgement

First, I would like to express my deepest gratitude to my scientific advisors Prof. Dr. Marc Kreutzbruck, Dr. Jens Prager and Prof. Dr. Reimund Gerhard, for their thoughtful guidance during my graduate study. They provided me with all kinds of opportunities for an independent and unrestricted research.

I am very grateful to Mr. Rainer Boehm, Dr. Jens Prager, Dr. Mate Gaal, Dr. Andrea Harrer and Dr. Hauke Gravenkamp for the fruitful and enlightening scientific discussions, and for reviewing of my publications and PhD thesis draft.

A special thanks to Dr. Uwe Beck and his working group, in particular to Mr. Matthias Weise, Ms. Thorid Lange and Mr. Mario Sahre, for their support and collaboration in production and characterization of the high-quality thermophone-samples.

Last but not least, I would like to thank Mr. Elmar Dohse for his continuous support and his helpfulness in development of electronic compounds and elements.